



## **Terms and Conditions of Use of Digitised Theses from Trinity College Library Dublin**

### **Copyright statement**

All material supplied by Trinity College Library is protected by copyright (under the Copyright and Related Rights Act, 2000 as amended) and other relevant Intellectual Property Rights. By accessing and using a Digitised Thesis from Trinity College Library you acknowledge that all Intellectual Property Rights in any Works supplied are the sole and exclusive property of the copyright and/or other IPR holder. Specific copyright holders may not be explicitly identified. Use of materials from other sources within a thesis should not be construed as a claim over them.

A non-exclusive, non-transferable licence is hereby granted to those using or reproducing, in whole or in part, the material for valid purposes, providing the copyright owners are acknowledged using the normal conventions. Where specific permission to use material is required, this is identified and such permission must be sought from the copyright holder or agency cited.

### **Liability statement**

By using a Digitised Thesis, I accept that Trinity College Dublin bears no legal responsibility for the accuracy, legality or comprehensiveness of materials contained within the thesis, and that Trinity College Dublin accepts no liability for indirect, consequential, or incidental, damages or losses arising from use of the thesis for whatever reason. Information located in a thesis may be subject to specific use constraints, details of which may not be explicitly described. It is the responsibility of potential and actual users to be aware of such constraints and to abide by them. By making use of material from a digitised thesis, you accept these copyright and disclaimer provisions. Where it is brought to the attention of Trinity College Library that there may be a breach of copyright or other restraint, it is the policy to withdraw or take down access to a thesis while the issue is being resolved.

### **Access Agreement**

By using a Digitised Thesis from Trinity College Library you are bound by the following Terms & Conditions. Please read them carefully.

I have read and I understand the following statement: All material supplied via a Digitised Thesis from Trinity College Library is protected by copyright and other intellectual property rights, and duplication or sale of all or part of any of a thesis is not permitted, except that material may be duplicated by you for your research use or for educational purposes in electronic or print form providing the copyright owners are acknowledged using the normal conventions. You must obtain permission for any other use. Electronic or print copies may not be offered, whether for sale or otherwise to anyone. This copy has been supplied on the understanding that it is copyright material and that no quotation from the thesis may be published without proper acknowledgement.



**Optical Characterisation of Blue-  
Green-Emitting Polymer Gain  
Media: Light Amplification, Laser  
Emission, and Two-Photon  
Absorption**

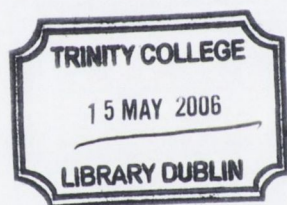
By

Grace Jordan

A thesis submitted for the degree of  
Doctor of Philosophy  
in the  
University of Dublin

School of Physics  
Trinity College Dublin

September 2005



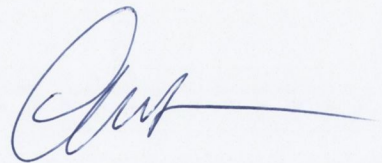
THOS  
7904

# Declaration

I declare that the work in this thesis has not been previously submitted as an exercise for a degree to this or any other university.

The work described herein is entirely my own, except for the assistance mentioned in the acknowledgements and the collaborative work mentioned in the list of publications.

I agree that Trinity College Library may lend or copy this thesis on request.

A handwritten signature in blue ink, appearing to read 'Grace Jordan', with a long horizontal flourish extending to the right.

Grace Jordan

September 2005

For my mother Pauline, and in memory of my father Frank

The wallpaper with which the men of science have covered the world of reality is falling to tatters.

Henry Miller, *Tropic of Cancer* 1934

# Acknowledgements

For the help and support I received during the period of my studies I am indebted to many. Firstly, I would like to thank Prof Werner Blau for the opportunities and guidance he provided throughout. Secondly, I would like to thank Dr. Takeyuki Kobayashi for all the help, support, advice and guidance that he has provided over the years.

To all the members of group BU past and present I am forever grateful for making my time in Trinity a fantastic one. I owe very special thanks to the original crew: Adam, Anna, Bernd, Brendan, Catriona, Colin, Jean-Edouard, Johnny, Keith, Manuel, Marie-Laurence, Martin, Margaret, Michael, Patrick, Rob, Rory, Sandy, Sean, Slipper, Steffi, Stefanie, Valerie. And to the ones who've come and gone since: Andy, Cahill, Chris, Christian, David B, David R, Donal, Eimhin, Eleni, Emer, Estelle, Eveann, Fiona, Gordon, Helen, James, Les, Marjo, Martin, Michael, Rebekah, Ronan, Shane, Sharon, Schweta, Sylvia, Trevor, Umar, Valeria. Thank you all for providing enlightenment and entertainment in one way or another!

A very special thank you to the members of the downstairs office in Westland Row, past and present for always being available for coffee, questions, chocolate and gin: Yenny, Nacho, Kev and Denis.

For all their support, technical and otherwise I would like to thank John Kelly, Michelle Duffy, Susan Priest, Suzanne Richmond, Dave Grouse, Mick Reilly, Pat

Flanagan, Joe McCauley, Ken Colcannon and last but not least, Jeannette Cummins without whom the whole thing would fall apart.

I would like to thank Marek Samoc in the Australian National University for all of his help during my time there, and I would like to thank Alan Lyons of Bell Laboratories for his help and advice. In addition, I am very grateful to our collaborators in the Optical Fiber Technology Centre in the University of Sydney for their work on the polymer fiber laser project.

I cannot thank enough, the people from outside of college who have supported me for *years* in almost everything I've done: My family who are too numerous to mention especially my Mum, all my friends but especially Claire and Michelle and of course, Steffen, who has kept me sane by just being around.

Thank you all, and send in the clowns.



# Abstract

Blue-green emitting stilbene dyes have been incorporated into different inert polymer hosts. Steady-state absorption and emission spectroscopy revealed a considerable host dependence of the spectroscopic properties of these dyes.

Gain spectroscopy was used to investigate the use of a stilbene dye-doped polymer for solid state amplifying or lasing devices. Initial investigations showed that the photostability of the dye was dependent on the host with polystyrene providing the most stable performance of the hosts investigated. The variable stripe length method was employed to measure the net modal gain of asymmetric slab waveguides under nanosecond UV pumping conditions. The modal gain measured was one of the highest reported to date for an organic material. Optically pumped low threshold lasing was also demonstrated in a rudimentary asymmetric slab waveguide laser.

The two-photon absorption cross-section of the dyes was measured in the femtosecond regime on both solution and solid-state samples using the z-scan technique and the two-photon induced fluorescence method. Large two-photon absorption cross-sections were measured in solution and in polystyrene hosts. However, the upconverted emission intensity was much weaker in other polymers. This has again been related to the increased rates of motion of the molecular backbone of the dyes due to heating from the infrared beam used in the experiments.

Having identified polystyrene as a suitable host polymer for stilbene dyes, it has been used as the host material for the fabrication of microring cavity lasers. Optical microscopy has been used to characterize the size, shape and surface morphology of the rings. Mode assignment has been carried out on the output spectrum and from this the mode diameter can be predicted. This is in good agreement with the ring diameter measured using optical microscopy. In addition, the agreement between the position of the spectral peaks and that predicted for a waveguide mode supported in the polymer microring indicates that the mode is well confined within the polymer layer. Furthermore, a method has been proposed based on surface chemistry, to provide a more controlled method of producing the microrings. Very low threshold lasing has been shown in 80  $\mu\text{m}$  diameter microrings under transverse UV excitation in the nanosecond regime which compares very well with other measurements on similar devices in the literature.

This study shows that from a spectroscopic point of view, stilbene dyes have excellent properties for gain and two-photon absorption. Their weakness lies in the flexible double bonds in their backbone, which allow torsional motion. However, suitable choice of host in the solid state inhibits this motion making them extremely stable. In addition, low-threshold lasing has been demonstrated in microrings under optical excitation.

# Table of Contents

<b>DECLARATION</b> .....	<b>2</b>
<b>ACKNOWLEDGEMENTS</b> .....	<b>5</b>
<b>ABSTRACT</b> .....	<b>7</b>
<b>CHAPTER 1 : INTRODUCTION</b> .....	<b>16</b>
1.1    MOTIVATION .....	16
1.2    SCIENTIFIC BACKGROUND .....	18
1.2.1 <i>Advantages of organic materials</i> .....	19
1.2.2 <i>Organic materials for photonics</i> .....	21
1.3    THESIS OUTLINE.....	24
REFERENCES .....	26
<b>CHAPTER 2 : LIGHT-MATTER INTERACTION AND ORGANIC MATERIALS</b> .....	<b>29</b>
2.1    THE INTERACTION OF LIGHT WITH MATTER.....	29
2.1.1 <i>Introduction</i> .....	29
2.1.2 <i>The Lorentz model</i> .....	30
2.1.3 <i>Quantum description: electronic transitions</i> .....	35
2.2    ORGANIC MATERIALS .....	36
2.2.1 <i>Introduction</i> .....	36
2.2.2 <i>Basic concepts in organic materials</i> .....	37
2.2.3 <i>Light absorption and conjugation</i> .....	38
2.2.4 <i>Absorption of light by organic dyes</i> .....	40
2.2.5 <i>Relaxation and deactivation pathways for excited molecules</i> .....	43
2.2.6 <i>Induced transitions and stimulated emission</i> .....	46
REFERENCES .....	48
<b>CHAPTER 3 : MATERIALS</b> .....	<b>49</b>
3.1    INTRODUCTION .....	49
3.1.1 <i>Stilbene dyes</i> .....	49
3.1.2 <i>Host polymer matrix materials</i> .....	51
3.2    UV-VISIBLE ABSORPTION AND EMISSION MEASUREMENTS.....	51
3.2.1 <i>Polymer Hosts</i> .....	52
3.2.2 <i>Absorption spectra: Dye solutions</i> .....	53
3.2.3 <i>Steady-state photoluminescence: Dye solutions</i> .....	54
3.2.4 <i>Solid state spectra</i> .....	55
3.3    PHOTOLUMINESCENCE QUANTUM YIELD (PLQY).....	61
3.3.1 <i>Introduction</i> .....	61
3.4    CONCLUSION .....	64
REFERENCES .....	65
<b>CHAPTER 4 : GAIN SPECTROSCOPY</b> .....	<b>66</b>
4.1    INTRODUCTION .....	66
4.2    THE ORGANIC DYE: A FOUR-LEVEL LASER SYSTEM .....	66
4.3    AMPLIFIED SPONTANEOUS EMISSION (ASE).....	68
4.3.1 <i>Variable stripe length method (VSM)</i> .....	69

4.4	THE ASYMMETRIC SLAB WAVEGUIDE.....	71
4.4.1	<i>Transverse Electric (TE) modes</i> .....	74
4.5	SAMPLE PREPARATION .....	76
4.6	MODAL GAIN MEASUREMENTS.....	80
4.6.1	<i>Experimental procedure</i> .....	80
4.6.2	<i>Initial tests</i> .....	81
4.6.3	<i>Modal gain in doped polystyrene</i> .....	83
4.6.4	<i>Loss measurements</i> .....	87
4.7	SLAB WAVEGUIDE LASER .....	89
4.8	DISCUSSION .....	92
4.9	SUMMARY.....	93
	REFERENCES .....	95
<b>CHAPTER 5 : TWO-PHOTON ABSORPTION SPECTROSCOPY .....</b>		<b>97</b>
5.1	INTRODUCTION .....	97
5.2	NONLINEAR POLARIZATION .....	98
5.3	TWO-PHOTON ABSORPTION.....	104
5.3.1	<i>Introduction</i> .....	104
5.3.2	<i>Upconversion</i> .....	104
5.3.3	<i>Optical Limiting</i> .....	105
5.3.4	<i>Two-photon spectroscopy and photochemistry</i> .....	105
5.4	DESIGN STRATEGIES FOR TWO-PHOTON ABSORBING MATERIALS .....	105
5.4.1	<i>Introduction</i> .....	105
5.4.2	<i>Quadrupolar molecules</i> .....	106
5.4.3	<i>Dipolar "push-pull" molecules</i> .....	108
5.4.4	<i>Recent advances in the design of octupolar and branching molecules for multiphoton absorption</i> .....	108
5.5	EXPERIMENTAL TECHNIQUES-A REVIEW .....	109
5.5.1	<i>Introduction</i> .....	109
5.5.2	<i>Nonlinear Transmission Methods</i> .....	109
5.5.3	<i>Two-photon induced fluorescence methods</i> .....	111
5.6	Z-SCAN TECHNIQUE.....	111
5.6.1	<i>Introduction</i> .....	111
5.6.2	<i>Z-scan theory</i> .....	113
5.6.3	<i>Experimental Procedure</i> .....	117
5.6.4	<i>Experimental Results</i> .....	118
5.7	TPIF-SOLID STATE MEASUREMENTS.....	123
5.7.1	<i>Introduction</i> .....	123
5.7.2	<i>Experimental details</i> .....	123
5.7.3	<i>Analysis</i> .....	125
5.7.4	<i>Experimental Results: Commerical Dyes: Rhodamine 6G and Coumarin120</i> .....	128
5.8	STILBENE DYES: SP35 AND SP48 .....	131
5.9	DISCUSSION .....	133
5.9.1	<i>Local field factor:</i> .....	133
5.9.2	<i>S<sub>0</sub>-S<sub>1</sub> transition dipole</i> .....	134
5.9.3	<i>Quantum Yield Ratio</i> .....	135
5.10	SUMMARY.....	136
	REFERENCES .....	138
<b>CHAPTER 6 : MICRORING LASER CAVITIES .....</b>		<b>141</b>

6.1	INTRODUCTION .....	141
6.1.1	<i>The microring cavity</i> .....	142
6.2	THE FORMATION OF FILMS ON FIBER SUBSTRATES .....	143
6.2.1	<i>Introduction</i> .....	143
6.2.2	<i>Ring formation: Experimental results</i> .....	145
6.3	CHARACTERIZATION OF LASER DEVICES: EXPERIMENTAL SET-UP .....	149
6.4	THE WAVE EQUATION IN CYLINDRICAL COORDINATES.....	150
6.5	QUALITY FACTOR .....	156
6.6	DEVICE CHARACTERIZATION: RESULTS AND ANALYSIS.....	158
6.6.1	<i>Capillary Device</i> .....	158
6.6.2	<i>80 micron diameter microrings</i> .....	163
6.7	COMPARISON WITH LITERATURE.....	174
6.8	FUTURE WORK .....	175
6.8.1	<i>Microrings</i> .....	175
6.8.2	<i>Polymer optical fiber production</i> .....	178
6.9	SUMMARY.....	180
	REFERENCES .....	182
<b>CHAPTER 7 CONCLUSIONS AND FUTURE WORK .....</b>		<b>184</b>
7.1	INTRODUCTION .....	184
7.2	SUMMARY.....	185
7.3	CONCLUSIONS.....	187
	REFERENCES .....	188
<b>APPENDIX I - CALCULATION OF PUMP FLUENCES .....</b>		<b>189</b>
<b>APPENDIX II - ESTIMATION OF EXCITED STATE POPULATION DENSITY.....</b>		<b>191</b>
<b>APPENDIX III- PUBLICATION LIST .....</b>		<b>193</b>

# List of Figures

Figure 1-1 Upconverted emission under two-photon excitation at 800 nm in a stilbene-dye doped PMMA step-index fiber.....	18
Figure 2-1 Schematic view of $sp^3$ hybridization.....	37
Figure 2-2 Schematic view of $sp^2$ hybridized bonding showing also the remaining unhybridized $p_z$ orbital <sup>7</sup> .....	38
Figure 2-3 Schematic of bonding structure of ethane $C_2H_4$ <sup>7</sup> .....	39
Figure 2-4 Conjugated bonds in butadiene.....	39
Figure 2-5 $P_z$ orbitals in benzene resulting in highly delocalised electronic system above and below the plane of the benzene ring. <sup>7</sup> .....	40
Figure 2-6 Franck-Condon diagram showing the vertical transition of an electron in a diatomic molecule from the lowest vibronic level of the electronic ground state to some high-lying vibronic level in the first excited electronic state.....	41
Figure 2-7 Jablonski diagram depicting some of the different photophysical processes seen in molecules. IC: internal conversion, ISC: intersystem crossing, ESA: excited state absorption.....	44
Figure 3-1 Molecular structure of trans-stilbene.....	50
Figure 3-2 Absorption spectra of host polymers; polystyrene, PVP and PMMA on glass substrates.....	52
Figure 3-3 Absorption spectra of SP35, SP48 and B2080 in toluene at a concentration of $\sim 10^{-5}$ M. ....	54
Figure 3-4 Emission spectra of SP35, SP48 and B2080 in toluene at a concentration of $\sim 10^{-5}$ M. ....	55
Figure 3-5 Absorption cross-section of B2080 in polystyrene, PMMA, and PVP. ....	57
Figure 3-6 Emission spectrum of B2080 in polystyrene, PMMA and PVP.....	58
Figure 3-7 Absorption spectrum of SP35 in polystyrene, PMMA and PVP. ....	58
Figure 3-8 Emission spectrum of SP35 in polystyrene, PMMA and PVP. ....	59
Figure 3-9 Absorption spectrum of SP48 in polystyrene, PMMA and PVP. ....	60
Figure 3-10 Photograph of SP48 and polymer solutions in chloroform approximately 1 hour after sonication. Also shown is SP48 and polystyrene in toluene which is a stable solution. ....	61
Figure 3-11 Absorption spectra of B2080 in toluene and coumarin120 in methanol measured in a 1 cm quartz cuvette.....	63
Figure 3-12 Fluorescence spectra of coumarin120 and B2080 when pumped at 355 nm.....	63
Figure 4-1 Schematic diagram of organic four-level laser system. ....	67
Figure 4-2 Schematic representation of variable stripe length experiment. ....	71
Figure 4-3 The asymmetric slab waveguide. The upper cladding layer is assumed to be air.....	72
Figure 4-4 Zig-zag ray path in an asymmetric slab waveguide.....	72
Figure 4-5 (a) Surface profile of polystyrene film and (b) cross-section of film. Spikes on surface are dust particles that have settled on the surface. ....	77
Figure 4-6 (a) Surface profile of PVP film and (b) cross-section of film. Spikes on surface are dust particles that have settled on the surface. ....	77
Figure 4-7 (a) Surface profile of PMMA film and (b) cross-section of film. Spikes on surface are dust particles that have settled on the surface. ....	78

Figure 4-8 Graphical solution to the eigenvalue equation for a typical polystyrene sample. Circles mark the intersection of the two functions which represents a solution to the equation. ....	79
Figure 4-9 Typical TE mode profile of polystyrene asymmetric slab waveguide. ....	79
Figure 4-10 Experimental setup used for modal gain measurements.....	80
Figure 4-11 Two isomers of stilbene. (a) trans-stilbene, (b) cis-stilbene.....	82
Figure 4-12 Possible route of irreversible photodegradation of symmetrically substituted stilbene molecule (adapted from reference 11). ....	82
Figure 4-13 ASE intensity as a function of excitation length at pump fluences of $97 \mu\text{J}/\text{cm}^2$ , $130 \mu\text{J}/\text{cm}^2$ , and $280 \mu\text{J}/\text{cm}^2$ , giving modal gain of $11 \text{ cm}^{-1}$ and $20 \text{ cm}^{-1}$ and $33 \text{ cm}^{-1}$ , respectively. ....	84
Figure 4-14 Modal gain as a function of pump fluence at 501 nm. Inset: Measured optical loss at 501 nm of $0.33 \text{ cm}^{-1}$ .....	85
Figure 4-15 Modal gain plotted versus excited state population density. Line is a linear fit to the data yielding a value of the effective induced emission cross-section of $(2.7 \pm 0.3) \times 10^{-16} \text{ cm}^2$ . ....	86
Figure 4-16 Gain spectrum of B2080 doped polystyrene waveguide at a pump fluence of $1.1 \text{ mJ}/\text{cm}^2$ . Inset: Fitting parameter $AP_0$ compared to spontaneous emission spectrum.....	87
Figure 4-17 Loss spectrum of B2080 doped polystyrene waveguide. The solid line is there to guide the eye. ....	88
Figure 4-18 Fabry-Perot cavity of length $L$ where $E_i$ is the incident wave complex amplitude and $t_n$ and $r_n$ are the transmission and reflection coefficients respectively. ....	89
Figure 4-19 Input-output characteristics of B2080 doped polystyrene slab waveguide laser. Kink in the data at approximately $23 \mu\text{J}/\text{cm}^2$ indicates the onset of lasing. ....	91
Figure 4-20 Evolution of spectral FWHM as a function of pump fluence for B2080 doped polystyrene slab waveguide laser. Inset: Emission spectrum above and below threshold.....	92
Figure 5-1 Potential energy curve for harmonic and anharmonic oscillator in a centrosymmetric material. ....	99
Figure 5-2 Parametric processes (a) third harmonic generation and (b) the optical kerr effect. Dashed lines denote virtual levels. ....	102
Figure 5-3 Two photon absorption via virtual level. ....	103
Figure 5-4 Schematic diagram of dipolar, quadrupolar and octupolar molecules. A: Acceptor, D: Donor.....	106
Figure 5-5 Schematic open and closed aperture z-scan experiment. The beam is split after the sample allowing simultaneous recording of open and closed aperture trace. Det: photodetector, BS: beamsplitter .....	111
Figure 5-6 Theoretical closed-aperture z-scans for a gaussian beam profile calculated with the use of Eq. 5.33. $\Delta\phi$ is the nonlinear phase shift which gives the strength of the nonlinearity and will be defined below.....	112
Figure 5-7 Theoretical open-aperture z-scans for a gaussian beam profile calculated from Eq. 5.36.....	113
Figure 5-8 Closed aperture scans for SP35 in chloroform solutions up to 0.755 % wt. Peak-to-valley difference decreases with increasing concentration indicating that the nonlinearity of SP35 has the opposite sign to that of	

chloroform at this wavelength. Solid lines are theoretically calculated according to Eq. 5.32:	$T(z, \Delta\Phi_0) \approx 1 - \frac{4\Delta\phi_0 z/z_0}{(z^2/z_0^2 + 9)(z^2/z_0^2 + 1)}$	119
Figure 5-9	Extracted value of $\Delta\phi_{\text{real}}$ of SP35 solution as a function of mass fraction.	120
Figure 5-10	Open aperture z-scans of SP35 in chloroform for concentrations of up to 0.755 %. Solid lines are curves calculated according to Eq. 5-3:	
	$T(z) = \exp(-\alpha_0 L) \frac{\ln[1 + q_0(z)]}{q_0(z)}$	121
Figure 5-11	Two-photon absorption coefficient versus number density of active molecules for SP35 in chloroform. Straight line is linear fit to data.	122
Figure 5-12	Maximum change in transmission as a function of number density of active molecules of SP35 in chloroform.	122
Figure 5-13	Schematic representation of TPIF experimental procedure.(a) Two-photon pumped upconversion, (b) one-photon pumped photoluminescence.	124
Figure 5-14	Experimental setup used for TPIF measurement. HR: High reflector, CCD: Charge coupled device.	125
Figure 5-15	Absorption cross-section of Rhodamine 6G in three different polymer hosts. Inset: normalized absorption spectra.	128
Figure 5-16	Upconversion efficiency parameter of Rhodamine 6G in PMMA and PVP. Also shown is TPA cross-section in ethanol as reported in reference 33. Solid lines are provided to guide the eye.	129
Figure 5-17	Linear absorption cross-section of Coumarin120 in different polymer hosts. Inset: Normalized absorption spectra.	130
Figure 5-18	Upconversion efficiency parameter of Coumarin120 in PVP and PMMA. Also shown is TPA cross-section of coumarin120 in ethanol taken from ref. 33.	130
Figure 5-19	Upconversion efficiency of SP35 in different polymer hosts. Also shown is the result of z-scan experiment in chloroform. In addition, data on a similar molecule has also been included from ref. 41.	132
Figure 5-20	Upconversion efficiency parameter of SP48 in different polymer hosts.	132
Figure 6-1	Diagram showing the contact angle between a liquid droplet and a flat horizontal substrate.	143
Figure 6-2	Equilibrium droplet shapes on fiber substrates (adapted from reference 15). (a) Barrel droplet shape, (b) Clam-shell droplet shape.	144
Figure 6-3	Screen shot of contact angle analysis software used to calculate contact angle on flat silica substrates.	146
Figure 6-4	Dye doped polystyrene microrings formed from toluene solutions on 200 $\mu\text{m}$ diameter fiber.	147
Figure 6-5	Image of microring on 200 $\mu\text{m}$ diameter fiber at a magnification of 10 X. Bubbles and inhomogeneities are evident on surface.	147
Figure 6-6	Emission spectrum from thickly coated 200 mm diameter microring laser	148
Figure 6-7	Schematic of microring cavity formed on the inside of a glass capillary.	149
Figure 6-8	Schematic of transverse pumping of microring using s stripe pump beam geometry.	149



Figure 6-9 Cylindrical coordinate system.....	150
Figure 6-10 Two types of modes in cylindrical cavity. Whispering gallery modes propagate by successive reflections at the outer boundary, while waveguide modes propagate by alternating reflections from inner and outer boundaries. ....	153
Figure 6-11 Schematic representation of microring cavity formed on inner surface of silica capillary.....	158
Figure 6-12 Typical emission spectrum from microring at a pump fluence of $1.9 \text{ mJ/cm}^2$ . Strong modulation of the emission spectrum is evident. Some of the peaks have been labelled with the order of the Bessel function.....	159
Figure 6-13 Measured position of spectral peak from capillary microring versus predicted peak using method outlined above. Slope of very close to 1 indicates good agreement between theory and experiment. ....	160
Figure 6-14 Integrated emission intensity as a function of pump fluence. Kink in the data at about $1.1 \text{ mJ/cm}^2$ indicates the onset of lasing.....	163
Figure 6-15 Microscope image of coated $80\mu\text{m}$ silica fiber. Regions A and B denote regions of different coverage. ....	164
Figure 6-16 Typical emission spectrum from Region B of Figure 6-15. ....	165
Figure 6-17 Typical emission spectrum from Region A of Figure 6-15.....	165
Figure 6-18 $80 \mu\text{m}$ diameter fiber after cleaning in KOH solution prior to coating. Fiber core is visible in centre of fiber . Magnification: 50 X....	166
Figure 6-19 Surface of $80 \mu\text{m}$ diameter fiber after cleaning in KOH solution prior to coating. Magnification: 50 X.....	166
Figure 6-20 Microrings formed on $80 \mu\text{m}$ diameter fiber. (a) image taken under normal lamp illumination. (b) Fluorescence image taken with long exposure under excitation with a UV light emitting diode. Ring marked with ellipse is selected as an area of interest for higher magnification measurements.....	167
Figure 6-21 Image of microring on $80 \mu\text{m}$ diameter fiber at magnification of 50. (a) Image taken under normal illumination. (b) image taken under excitation with UV light emitting diode at long exposure. ....	168
Figure 6-22 High magnification (100 X) image of microring surface showing microstructure on coating surface.....	169
Figure 6-23 Typical emission spectrum from $80 \mu\text{m}$ microrings shown in Figure 6-20.....	170
Figure 6-24 Emission spectrum plotted on a semi-logarithmic scale. Triangles represent predicted position of peaks. ....	172
Figure 6-25 Measured wavelength peaks versus predicted peak position. Gaps have been left where it is evident that some of the peaks are missing from the spectrum. ....	172
Figure 6-26 Integrated emission intensity as a function of pump fluence. Straight line method has been used to give a lasing threshold of $12.5 \mu\text{J/cm}^2$ .....	173
Figure 6-27 Emission spectrum from $80 \mu\text{m}$ microrings under longitudinal pumping. ....	175
Figure 6-28 Microscope image of $80 \mu\text{m}$ ring formed on surfacesilane- treated fiber. ....	177
Figure 6-6-29 Image of fiber preform after stretching stage. Black spots are bubbles in the core of the fiber. ....	179

# Chapter 1: Introduction

## 1.1 Motivation

The motivation for this work came from two distinct observations on the optical properties of stilbene dyes doped into polymer host materials. Polymer thin film waveguides doped with a substituted stilbene dye were observed to exhibit evidence of optical gain, showing drastic gain narrowing and a superlinear increase in emission with excitation length when pumped in the UV spectral region with a nanosecond (ns) pump laser. In addition, very intense fluorescence from a stilbene dye-doped polymer optical fiber (POF) was observed under two-photon excitation.<sup>1</sup> Figure 1-1 shows a photograph of the fiber when it was longitudinally pumped at 800 nm by 175 femtosecond (fs) optical pulses from a mode-locked titanium sapphire laser. The stilbene dyes used in this work emit in the blue-green spectral region which is a region of interest in many areas such as next generation optical storage media, and data transmission systems using acrylate POFs.<sup>2</sup> In addition, materials with large two-photon absorption and exhibiting strong upconverted emission are interesting in the area of two-photon fluorescence microscopy. Following the pioneering work by Denk et al.<sup>3</sup> this technique has become a very popular technique for the characterization of biological samples and has become an indispensable tool in many areas of biological study. In this method, a fluorescent

label is used to stain a sample which is then excited using a red or near IR laser, often titanium sapphire which generates upconverted emission. This technique is especially useful since the  $I^2$  dependence of the emission allows for site selective excitation and three dimensional imaging. Blue green emitting dyes are particularly suitable for this application since they are readily excited by TPA in the near IR, and many detectors are most sensitive in the blue-green spectral region. Furthermore, in recent years fluorescent green proteins have been used to stain cells since the protein is expressed differently in different parts of the cell, an effect called cell transfection.<sup>4</sup> A further application of materials with good two photon absorption and upconversion properties is in the development of upconversion laser devices. While upconverted lasing by two photon absorption in solutions of organic dyes has been shown many times,<sup>5</sup> there are far fewer studies illustrating two-photon pumped lasing in the solid state using an organic material.<sup>6</sup> However, the POF shown in Figure 1-1 has been shown to exhibit no optical gain under one or two photon pumping. This is due to the photochemical instability of the dye in the polymer host, thus showing that the performance of the dye is very sensitive to the environment in which it operates. The fiber was made by Paradigm Optics<sup>1</sup> and the method by which the fiber preform was made and the drawing conditions were not available.

The aim of this work is to characterize materials with large induced emission cross-section and corresponding gain, for use in compact blue-green solid-state laser or amplifier devices including finding a suitable host material in which the chosen material can perform optimally and also incorporating the material into a high Q cavity. In addition, the possibility for two-photon pumped lasing in a solid-state device is investigated by measuring the two-photon absorption cross-section and its host dependence. Two types of cavity were chosen for investigation, namely microring cavities formed by coating silica fibers and, the possibility of making an all polymer fiber laser by doping the dye into the core of a POF.

---

<sup>1</sup> PARADIGM OPTICS INC., Pullman, WA 99163, USA.

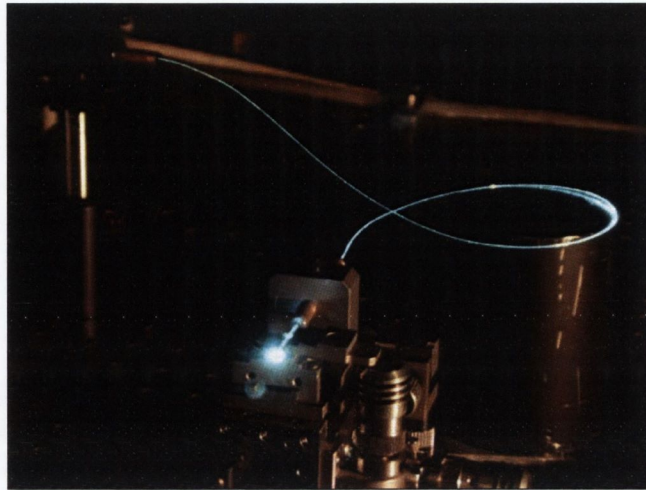


*Figure 1-1 Upconverted emission under two-photon excitation at 800 nm in a stilbene-dye doped PMMA step-index fiber.*

## 1.2 Scientific Background

Photonics is the generation, manipulation, storage and detection of photons and covers such broad-ranging research areas as lighting, display technologies, data communications, data storage, photovoltaics, and sensors technologies as well as many laboratory-based research areas like nonlinear optics, optical computing, and optical interconnects for high-speed information processing. With the fundamental limits of electronics being rapidly approached, many researchers believe that information technology based on the manipulation of photons instead of electrons may provide the key to ever faster and smaller devices.<sup>7</sup>

Most well-established optical technologies are based on inorganic materials such as the III-V semiconductors and silica which provide such high performance that much of the research has moved into optimising device fabrication and packaging to achieve low-cost manufacturing and high throughput.<sup>8</sup> There are areas however where an inherently low-cost and flexible alternative may be competitive. It is into these niche areas that organic materials have already, and may continue to fit. Essential to the realisation of the full potential of organics is the design of well-characterised materials with the required level of functionality. There is an almost endless array of organic materials to choose from with chemists continually designing and synthesising new structures. Some examples of these include

structural (saturated) polymers like poly (methyl methacrylate) and polystyrene, conjugated light-emitting polymers like polyfluorene and poly (phenylene vinylene) derivatives, small molecules such as Alq<sub>3</sub> or Rhodamine 6G and conducting polymers like polyaniline to name but a few. As the materials increase in complexity and sophistication, an ever increasing number of applications can be found and at the high end of the complexity scale, lie the naturally occurring biological materials which are now under intense investigation for fundamental studies but also as building blocks for future technological applications.<sup>9</sup>

The following review will attempt to give an overview of the history and current state of research in the area of organic materials for photonic applications with particular attention being paid to the area of research most relevant to this thesis, namely that of lasing. A review of organic materials for nonlinear optical applications will be given in Chapter 5.

### 1.2.1 Advantages of organic materials

Carbon rich organic molecular materials are unique building blocks for many applications. The solid state is composed of individual molecules held together by the relatively weak van der Waals interaction making them inherently soft and flexible. In contrast to covalently bonded semiconductors which are hard and brittle<sup>10</sup> this flexibility is one of the key advantages of organic materials (although it also means that they can be susceptible to environmental damage). Many processes that take advantage of this feature may be envisaged and have in many cases already been implemented such as ink-jet printing of active materials,<sup>11</sup> patterning by soft embossing<sup>12</sup> and micromolding,<sup>13</sup> and other simple scalable methods of patterning to produce devices that emit light in a well-defined way. For example, Paloczi *et al.*<sup>14</sup> have demonstrated a polymer Mach-Zender electro-optic modulator produced using high throughput soft stamp replica moulding. In addition, it is possible to use simple spin-coating or screen-printing of solutions on large area substrates for large area displays.

Small laser resonators made from organic materials have been made in many different ways. One of the simplest structures is that of a slab waveguide where lasing occurs along the length of a stripe pump beam<sup>15</sup> with feedback being

provided by reflections from the films edges. To provide lateral guiding, photolithographic methods can be employed to make channel waveguides.<sup>16</sup> Planar microcavity lasing in a thin polymer film sandwiched between two dielectric mirrors<sup>17</sup> and between a dielectric mirror and a metal<sup>18</sup> has been shown. Distributed feedback lasers have been formed on patterned substrates<sup>19</sup> and by micromolding.<sup>13</sup> In addition, whispering gallery mode lasing has been shown in microdisks,<sup>20</sup> microrings<sup>21</sup> and microspheres.<sup>22</sup> These studies illustrate the benefit of using organic materials for the study of interesting device geometries and related phenomenon without the need for expensive or unwieldy manufacturing processes.

Because it is the individual molecular unit that governs the photophysics of organic materials, tailoring the electronic transitions becomes possible by modifying the molecular structure. In contrast to epitaxially grown inorganic semiconductors, this is readily achievable at the synthetic level. Absorption and emission wavelengths, solubility, Stokes shift, quantum yield, and nonlinear response can all be tuned and optimised by suitable molecular engineering. Obviously, this requires detailed understanding of the photophysics of the molecules and much effort has gone into this in recent years.

In addition to this high degree of chemical flexibility, organic materials have other inherent advantages due to their molecular nature. For example, the characteristic broad absorption and emission spectrum allows broadband amplification, a wide choice of wavelengths for pumping or nonlinear optical applications, and the possibility of ultra-fast pulse generation.<sup>23</sup> In addition, the absorption cross-section of many organic materials is of the order of  $10^{-16}$  cm<sup>2</sup>, which allows for the generation of high excited state population densities under optical excitation. To a first approximation, the stimulated emission cross-section is of the same order of magnitude allowing for very large optical gain over short gain lengths leading to the possibility of extremely small laser and amplifier devices. This may be contrasted with erbium for example, where several meters of doped fiber is used in a typical erbium doped fiber amplifier.<sup>24</sup>

Since most organic material have a low glass transition temperature, much of the processing required for device fabrication, can be carried out at low temperature. For example, polymer optical fibers can be extruded below 200 °C. Due to this and

because of the low cost and inherently flexible nature of POF, short-range communication applications are an ideal destination for this robust technology. Indeed, in the aviation and automobile industries, POF networks using visible light have already been implemented.<sup>25</sup> Wavelengths of interest in these systems are 520 nm and 640 nm, and 840 nm, the former two being low loss spectral regions of acrylate polymers while the latter being one of the communication windows of polyimides and perfluorinated polymers. Recently, Matsuoka *et al.*<sup>26</sup>, and Akhter *et al.*<sup>2</sup> reported data transmission at 520 nm and 509 nm respectively in PMMA core polymer optical fiber in the green where PMMA has a low loss window. The cost of these networks could be reduced further with the use of low-cost sources, amplifiers and receivers that operate in the visible region. Although electrically pumped organic diode lasers and amplifiers are still far from being realised, this area is one of many where they could ultimately find their niche.

## 1.2.2 Organic materials for photonics

Active organic photonic materials can be roughly divided into two categories; that of small molecular systems where the molecular weight is well defined and that of conjugated polymers which are composed of repeating monomeric units of indefinite length.

### **Small Molecules**

There is an almost endless array of small organic molecules. For example, there are the many types of laser dyes having absorption bands in the UV and visible parts of the spectrum and showing high quantum yield photoluminescence like the Xanthenes and Coumarins. There are a whole range of porphyrins and phthalocyanines which have interesting nonlinear optical responses and can be engineered to be excellent phosphorescent emitters.<sup>10</sup> There are semiconductors such as Alq<sub>3</sub> and TPD which have been used in thin film electro-luminescent devices<sup>27</sup> and there are molecules with a large dipole moment for electro-optic applications.<sup>28</sup> These are only a few examples of the wide-ranging areas of interest.

The first use of an organic dye as a laser medium was demonstrated by Sorokin and Lankard, when they achieved lasing in a phthalocyanine dye pumped with a ruby laser.<sup>29</sup> (For an extensive bibliography on the early developments of dye lasers, the

reader is referred to reference 30). Shortly thereafter, Sorokin and Lankard<sup>31</sup> (1967) and Schmidt and Schäfer<sup>32</sup> (1967) demonstrated that a dye laser could be pumped with a flashlamp. Since then, many highly efficient laser dyes have been developed. The most successful of these are probably the Xanthenes, especially Rhodamine6G and the Coumarin group of dyes. Although laser dyes have been shown to lase in liquid, solid and gas phases,<sup>33</sup> they are most frequently used in solutions of organic solvents. This is because high optical quality cuvettes can be used to house the solution and cooling and replenishment of degraded dye molecules can be achieved by simply circulating the solution using a magnetic stirrer. However, organic solvents are in many cases toxic and although solution based dye lasers are very useful in the laboratory when a tuneable source is required, they have a limited range of applications outside of the laboratory.

Since the early days of their development, attempts have been made to achieve lasing in organic dyes in the solid phase.<sup>34</sup> Neat films of organic dyes do not lase due to concentration quenching and aggregate formation so it is necessary to incorporate the dye into a solid host which is most often an inorganic glass or transparent polymer.<sup>33</sup> A good host is one that is chemically stable under exposure to laser radiation and in addition, has a low thermal expansion coefficient. Low temperature sol-gel processes allow the incorporation of organic dyes into inorganic silica glasses and have been shown to have good laser efficiency.<sup>35</sup> Transparent organic polymers are also good hosts in many cases and there are two main ways in which the dye can be incorporated into the host polymer. If a solvent exists that can dissolve both the polymer and the dye, then thin films can be spin-cast from the solution to give high optical quality samples. Alternatively, the dye can be dissolved in the monomer (if they are compatible) and the monomer subsequently polymerised to form a doped-polymer bulk. The advantage of this is that the bulk takes the shape of the container in which the polymerisation takes place, which can be a useful property. For example, the bulk can be formed in a small-diameter glass capillary tube which results in the formation of a glass-clad fiber.<sup>36</sup> Alternatively, the bulk can take the shape of a fiber preform which can then be drawn into a POF.<sup>37</sup> Unfortunately, the polymerisation process can result in degradation of the dye and other problems that will be discussed in more detail in Chapter 7.



To find a real technological application, it seems likely that electrical pumping would be highly advantageous and in that sense it seems as though small molecules have a disadvantage over other organic materials such as conjugated polymers. One method that *may* solve this issue is pumping based on energy transfer.<sup>38</sup> In this case the dye is incorporated into organic or polymeric material capable of charge transport and the electrically generated excited state is transferred by energy transfer to the emitter. The main problem with devices based on this system is the same as that encountered in all electrically driven polymeric/organic devices; that of absorption of charge carriers (polaron absorption) and despite much research effort, this problem has remained prohibitive to electrically driven lasing in an organic material. Alternatively, it has been suggested that a two-component system comprised of an inorganic InGaN laser diode could be used to pump a resonator made from an organic material.<sup>39</sup> This system takes advantage of the efficient InGaN laser diode while providing the high degree of tunability and low lasing threshold of organic materials.<sup>40</sup> In this case, dye-doped polymers can compete just as effectively if not more so than conjugated polymers.

Optically pumped devices are still of practical interest, since for example optically pumped erbium doped fiber amplifiers are commercially available. However, these are generally CW devices. The problems associated with triplet absorption mean that currently from a practical point of view, pulsed pumping of organic materials is necessary.

### **Conjugated polymers**

Since the discovery of electrical conductivity in doped polyacetylene,<sup>41</sup> a large amount of progress has been made in the design and synthesis of conjugated polymers. Conjugated polymers are characterised by a large delocalisation of the  $\pi$ -electronic system due to the degree of conjugation, making them distinct from structural polymers like PMMA and polystyrene. This delocalisation of the  $\pi$ -electrons along the polymer chain leads to semiconductor behaviour where the  $\pi^*$  orbital can support mobile charge carriers.  $\pi$ - $\pi^*$  transitions occur at frequencies from the UV to the visible resulting in materials that are capable of both electrical conduction and visible photoluminescent emission. The first demonstration of

electroluminescence from a conjugated polymer was given by Burroughes *et al.*<sup>42</sup> in 1990 using PPV. This immediately prompted ambitions of electrically pumped organic light emitting diodes (OLED) and laser diodes (LD). The work on OLEDs has been very successful and has reached commercialisation.<sup>43</sup> The organic laser diode however, has remained elusive.

In 1992 Moses demonstrated photo-pumped lasing from poly(2-methoxy-5-(2'-ethylhexyloxy)-1,4-phenylene vinylene (MEH-PPV) in solution.<sup>44</sup> Photo-pumped lasing in the solid-state proved more difficult than expected and initial pump-probe studies on MEH-PPV films diluted with polystyrene<sup>45</sup> implied that the interaction between neighbouring polymer chains played an important role (exciton-exciton annihilation). Finally, in 1996 stimulated emission and lasing in neat films of conjugated polymer was demonstrated.<sup>46,47,48,49</sup> Subsequently the problems due to interchain interactions were removed by the addition of bulky side-chains<sup>50</sup> leading to materials with high luminescent quantum yields in neat films.

Estimates on the best photo-pumped organic lasers have shown that the theoretical threshold current density for lasing is at an achievable level<sup>39</sup> and yet no demonstration of electrically pumped lasing has been forthcoming. The two main reasons for this are the added losses due to metal electrode absorption and more importantly very broad-band carrier-induced absorption, neither of which are present in optically pumped resonator structures.<sup>39</sup> In addition, spin-statistics<sup>51</sup> have shown that electrically generated excitons are formed with a triplet-singlet ratio of 3:1.

### 1.3 Thesis outline

The thesis will be outlined as follows:

Chapter 2 will give the formal theoretical background for the interaction of light with matter in the linear regime using the Lorentz model to describe the response of an elastically bound electron to a time varying electric field. This will be followed by an introduction to the basic concepts of organic materials, and pertinent aspects of their photophysics.

Chapter 3 will introduce the materials used in this study namely a series of substituted stilbene dyes and present their basic spectroscopic properties in solution and solid state. Much of this basic spectroscopic information is used in later chapters.

Chapter 4 will use gain spectroscopy on thin polymer films doped with a substituted stilbene dye to demonstrate very large modal gain under UV excitation. The gain is measured at a range of wavelengths and pump fluences and the stimulated emission cross-section extracted. Low-threshold lasing is demonstrated in a rudimentary slab waveguide laser.

Chapter 5 will focus on the two-photon absorption behaviour of several dyes, with particular focus on their upconversion abilities. The measurements use fs near IR excitation to measure the two-photon absorption cross-section in solution and in solid thin films using z-scan and two-photon induced fluorescence (TPIF) method.

The subject of Chapter 6 is the design of high-Q microring lasers. The relationship between microring cavity size, geometry and quality is investigated and low threshold lasing is demonstrated

Finally, a summary of the work and outlook will be given in Chapter 7.

## References

- <sup>1</sup> G. Jordan, T. Kobayashi, W.J. Blau, H. Tillman, H.-H. Hörhold, *Adv. Funct. Mater.* **13**, 751 (2003).
- <sup>2</sup> M. Akhter, P. Maaskant, B. Roycroft, B. Corbett, P. de Mierry, B. Beaumont, K. Panzer, *Electron. Lett.* **38**, 1457 (2002).
- <sup>3</sup> W. Denk, J.H. Strickler, W.W. Webb, *Science*, **248**, 73 (1990).
- <sup>4</sup> J. Sheen, S. Hwang, Y. Niwa, H. Kobayashi, D.W. Galbraith, *Plant J.* **8**, 777 (1995).
- <sup>5</sup> G.S. He, R. Signorini, P.N. Prasad, *Applied Optics* **37**, 5720 (1998).
- <sup>6</sup> G.S. He, J.D. Bhawalkar, C.F. Zhao, C.K. Park, P.N. Prasad, *Appl. Phys. Lett.* **68**, 3549 (1996).
- <sup>7</sup> N. Savage, <http://www.spectrum.ieee.org/WEBONLY/publicfeature/aug02>
- <sup>8</sup> M.F. Dautartas, J. Fisher, H. Luo, P. Datta, A. Jeantilus, *Proceedings of IEEE Electronic Components and Technology Conference* (2002).
- <sup>9</sup> G. Subramanyam, E. Heckman, J. Grote, F. Hopkins, R. Neidhard, E. Nykiel, *Microw. Opt. Tech. Lett.* **46**, 278 (2005).
- <sup>10</sup> S.R. Forrest, *Nature* **428**, 911 (2004).
- <sup>11</sup> T.R. Hebner, C.C. Wu, D. Marcy, M.H. Lu, J.C. Sturm, *Appl. Phys. Lett.* **72**, 519 (1998).
- <sup>12</sup> M. Geissler, Y. Xia, *Adv. Mater.* **16**, 1249 (2004).
- <sup>13</sup> J.R. Lawrence, G.A. Turnbull, I.D.W. Samuel, *Appl. Phys. Lett.* **82**, 4023 (2004).
- <sup>14</sup> G.T. Paloczi, Y. Huang, A. Yariv, J. Luo, a. K.-Y. Jen, *Appl. Phys. Lett.* **85**, 1662 (2004).
- <sup>15</sup> T. Kobayashi, J.-B. Savatier, G. Jordan, W.J. Blau, Y. Suzuki, T. Kaino, *Appl. Phys. Lett.* **85**, 185 (2004).
- <sup>16</sup> A. Mukherjee, *Appl. Phys. Lett.* **62**, 3423 (1993).
- <sup>17</sup> T. Granlund, M. Theander, M. Berggren, M. Andersson, A. Ruzeckas, V. Sundström, G. Björk, M. Granström, O. Inganäs, *Chem. Phys. Lett.* **288**, 879 (1998).
- <sup>18</sup> N. Tessler, G.J. Denton, R.H. Friend, *Nature* **382**, 695 (1996).

- 
- <sup>19</sup> G. Heliotis, R. Xia, G. A. Turnbull, P. Andrew, W.L. Barnes, I.D.W. Samuel, D.C.C. Bradley, *Adv. Funct. Mater.* **14**, 91 (2004).
- <sup>20</sup> M. Kuwata-Gonokami, R.H. Jordan, A. Dodabalapur, H. E. Katz, M.L. Schilling, R.E. Slusher, *Optics Letters* **20**, 2093 (1995).
- <sup>21</sup> Y. Kawabe, Y. Kawabe, Ch. Spiegelberg, A. Schuelzgen, M. Nabor, B. Kippelen, E. A. Mash, P.M. Allemand, M. Kuwata-Gonokami, K. Takeda, N. Peyghambarian, *Appl. Phys. Lett.* **72**, 141 (1998).
- <sup>22</sup> T. Takahashi, S. Matsuo, H. Misawa, T. Karatsu, A. Kitamura, K. Kamada, K. Ohta, *Thin Solid Films* **331**, 298 (1998).
- <sup>23</sup> C.V. Shank, E.P. Ippen, in *Topics in Applied Physics: Dye Lasers*, Ed. F.P. Schäfer, (Springer-Verlag, 1977)
- <sup>24</sup> E. Desurvire, *Erbium Doped Fiber Amplifiers: Principles and Applications*, (Wiley, New York, 1994).
- <sup>25</sup> URL: <http://www.firecomms.com/Applications/Automotive.aspx>
- <sup>26</sup> T. Matsuoka, T. Ito, T. Kaino, *Electron. Lett.* **36**, 1836 (2000).
- <sup>27</sup> R.H. Friend, R.W. Gymer, A.B. Holmes, J.H. Burroughes, R.N. Marks, C. Taliani, D.C.C. Bradley, D.A. Dos Santos, J.L. Brédas, M. Lögdlund W.R. Salaneck, *Nature* **397**, 121 (1999).
- <sup>28</sup> E.G.A. Notaras, PhD Thesis, Australian National University, 2005.
- <sup>29</sup> P.P. Sorokin, J.R. Lankard, *IBM J. Res. Develop.* **10**, 162 (1966).
- <sup>30</sup> F.J. Duarte, L.W. Hillman, *Dye Laser Principles*, (Academic Press Inc., 1990).
- <sup>31</sup> P.P. Sorokin, J.R. Lankard, *IBM J. Res. Develop.* **11**, 148 (1967).
- <sup>32</sup> W. Schmidt, F.P. Schaefer, *Zeit. Forsch. (German)* **22a**, 1563 (1967).
- <sup>33</sup> A. Costela, Garcia-Moreno, R. Sastre, *Phys. Chem. Chem. Phys.* **5**, 4745 (2003).
- <sup>34</sup> H.P. Weber, R. Ulrich, *Appl. Phys. Lett.* **19**, 38 (1971).
- <sup>35</sup> M.D. Rahn, T.A. King, *Appl. Op.* **34**, 8260 (1995).
- <sup>36</sup> T. Kobayashi, W.J. Blau, H. Tillmann, H.-H. Hörhold, *Optics Letters* **26**, 1952 (2001).
- <sup>37</sup> A. Samoc, B. Luther-Davies, M. Samoc, M.S. Wong, R.M. Krolukowska, T.M. Martin, C.J. MacLeod, A.C. Freydank, G.-D. Peng, T. Whitbread, *Proceedings of SPIE* **4798**, 87, (2002).

- 
- <sup>38</sup> A. Dodabalapur, M Berggren, R.E. Slusher, Z. Bao, A. Timko, P. Schiortino, E. Laskowski, H.E., Katz, O. Nalamasu, *IEEE J. Selected Topics Quant. Elect.* **4**, 67 (1998).
- <sup>39</sup> M.D. McGehee, A.J. Heeger, *Adv. Mater.* **12**, 1655 (2000).
- <sup>40</sup> F. Hide, P. Kozodoy, S.P. DenBaars, A.J. Heeger, *Appl. Phys. Lett.* **70**, 2664 (1997).
- <sup>41</sup> C.K. Chiang, C.R. Fincher, Y.W. Park, A.J. Heeger, H. Shirakawa, E.J. Louis, S.C. Gau, A.G. MacDiarmid, *Phys. Rev. Lett.* **39**, 1098 (1977).
- <sup>42</sup> J.H. Burroughes, *Nature* **347**, 539 (1990).
- <sup>43</sup> URL: [http://www.kodak.com.ekh nec/PageQuerier.jhtml?pq-path=1473/1481/1486&pq-locale=en\\_US&pq-pf=1](http://www.kodak.com.ekh nec/PageQuerier.jhtml?pq-path=1473/1481/1486&pq-locale=en_US&pq-pf=1)
- <sup>44</sup> D. Moses, *Appl. Phys. Lett.* **60**, 3215 (1990).
- <sup>45</sup> L.J. Rothberg, M. Yan, F. Papadimitrakopoulos, M.E. Gavin, E.W. Kwock, T.M. Miller, *synth. Met.* **80**, 41 (1996).
- <sup>46</sup> W. Graupner, G. Leising, G. Lanzani, M. Nisoli, S.D. Silvestri, U. Scherf, *Phys. Rev. Lett.* **76**, 847, (1996).
- <sup>47</sup> N. Tessler, G.J. Denton, R.H. Friend., *Nature* **382**, 695 (1996).
- <sup>48</sup> F. Hide, M.A. Diaz-Garcia, B. Schwartz, M. Andersson, G. Pei, A.J. Heeger, *Science* **273**, 1833 (1996).
- <sup>49</sup> S. Frovlov, W. Gellerman, M. Ozaki, K. Yoshino, Z.V. Vardeny, *Phys. Rev. Lett.* **78**, 729 (1996).
- <sup>50</sup> B.R. Hsieh, Y. Yu, E.W. Forsythe, G.M. Schaaf, W.A. Field, *J. Em. Chem. Soc.* **120**, 231 (1998).
- <sup>51</sup> M. Reuter, M.J. Walter, P.G. Raquodakis, B. Hummel, J.S. Kolb, H.G. Roskos, U. Scherf, J.M. Lupton, *Nat. Mater.* **4**, 340 (2005).

# Chapter 2: Light–Matter Interaction and Organic Materials

## 2.1 The interaction of light with matter

### 2.1.1 Introduction

The way in which light interacts with matter gives rise to the optical properties of materials. The absorption and emission spectra, quantum yield, lifetime, nonlinearity, and amplifying ability are all a function of the way in which the time dependent electric and magnetic fields of light interact with the charges in real matter. The interaction of light with a dielectric material is most simply described via the refractive index  $n$ , which is the ratio of the speed of light in a vacuum to that in the material. This chapter will derive the form of the refractive index using the Lorentz model or classical electron oscillator (CEO) model which considers an electron elastically bound to a stationary nucleus under the influence of a time varying electric field. Despite the fact that this model does not take into account the quantum nature of matter, it is still a very useful model and leads to a description of such phenomena as dispersion and refraction. To take into account the possibility

of absorption, a damping term is included in the model which leads to a complex refractive index. The Lorentz model as presented in this chapter represents the linear response of matter to impinging light. Nonlinear optics deals with the interaction of matter with high intensity light and is the subject of Chapter 5 where the theoretical background of the nonlinear response will be introduced.

In the following discussion and subsequent chapters, vectors will be denoted by an underscore while complex variables will be represented with a tilde.

### 2.1.2 The Lorentz model

Matter is composed of charged particles such as protons and electrons. Under the influence of the external electric field of light, these charges respond and rearrange themselves setting up an internal electric field which in turn interacts with the propagating light. This back-and-forth exchange of energy between the applied field and the internal field of the material gives rise to the rich assortment of optical phenomenon that are seen in the laboratory and in the natural world.

The mathematical description of the interaction of light and matter is given by Maxwell's equations:<sup>1,2</sup>

$$\nabla \cdot \underline{D} = 0 \quad (2.1)$$

$$\nabla \cdot \underline{B} = 0 \quad (2.2)$$

$$\nabla \times \underline{E} = -\frac{\partial \underline{B}}{\partial t} \quad (2.3)$$

$$\nabla \times \underline{H} = \frac{\partial \underline{D}}{\partial t} \quad (2.4)$$

Where  $\underline{E}$  and  $\underline{H}$  represent the electric and magnetic field vectors respectively.  $\underline{D}$  and  $\underline{B}$  are the electric and magnetic displacement vectors respectively which represent the *total* electric and magnetic fields in the medium. They may be written:

$$\underline{D} = \epsilon_0 \underline{E} + \underline{P} = \epsilon \underline{E} \quad (2.5)$$



$$\underline{B} = \mu_0 \underline{H} \quad (2.6)$$

Where  $\epsilon_0$  is the electric permittivity of a vacuum,  $\epsilon$  is the permittivity of the material,  $\mu_0$  is the magnetic permeability of a vacuum and  $\underline{P}$  is the polarization per unit volume of the material through which the electromagnetic wave propagates. This term is central to understanding the electric response of the material and is the only term in Maxwell's equations that refers directly to the medium.

Applying the curl operator to Eq. 2.3

$$\nabla \times (\nabla \times \underline{E}) = \nabla \times \frac{\partial \underline{B}}{\partial t} = \frac{\partial}{\partial t} (\nabla \times \underline{B}) = -\mu_0 \frac{\partial}{\partial t} (\nabla \times \underline{H}) \quad (2.7)$$

and noting

$$\nabla \times (\nabla \times \underline{E}) = \nabla (\nabla \cdot \underline{E}) - \nabla^2 \underline{E} \quad (2.8)$$

and applying Eqs. 2.4 and 2.5 leads to:

$$\nabla^2 \underline{E} - \frac{1}{c^2} \frac{\partial^2 \underline{E}}{\partial t^2} = \mu_0 \frac{\partial^2 \underline{P}}{\partial t^2} \quad (2.9)$$

Where  $c$  is the speed of light in a vacuum given by  $c = \frac{1}{\sqrt{\epsilon_0 \mu_0}}$ . This equation describes the response of a material to an external field via the polarization. For free-space propagation,  $\underline{P} = 0$ , and the equation reduces to the homogenous form. In order to understand the nature of the polarization term in a material, it is necessary to consider the atomic nature of matter and discuss how the charges within matter respond to the applied electric field. The Lorentz model can be used to describe this response in the linear regime.

The Lorentz model represents the response of a single electric-dipole to an external electric field in terms of a restoring force that is linearly proportional to the displacement, leading to simple harmonic oscillation of the dipole. In simplified terms, it is then possible to treat the atom as a classical dipole oscillator composed of a very large stationary positively charged nucleus coupled to a single electron

which may be displaced from its equilibrium position by an external electric field. The total polarization is then treated as the sum of the individual dipole responses.

In the 1-D approximation the electron under consideration is elastically bound to the nucleus and upon being displaced from its equilibrium position by  $x(t)$ , it will experience a restoring force  $F(t)$  due to the positively charged nucleus which is linearly proportional to the displacement according to Hooke's Law:

$$F(t) = -Kx(t) \quad (2.10)$$

Where  $K$  is the spring constant. In an undriven system, once initially displaced, the electron will undergo oscillations at a natural frequency given by:

$$\omega_0 = \sqrt{\frac{K}{m_e}} \quad (2.11)$$

Where  $m_e$  is the electronic mass. The electronic charge cloud in a real atom is similar in many ways to this point charge model. When an electromagnetic wave impinges on such a cloud, it behaves as a driven oscillator. From Newton's second law, and assuming a harmonic electric field with time dependence of the form:  $E(t) = E_0 \cos \omega t$  where  $E_0$  is the field amplitude, the equation of motion of a driven oscillator in one dimension may be written as:

$$eE_0 \cos \omega t - m_e \omega_0^2 x(t) = m_e \frac{d^2 x(t)}{dt^2} \quad (2.12)$$

It may be anticipated that the electronic response will closely follow that of the driving field and using a trial solution of

$$x(t) = x_0 \cos \omega t \quad (2.13)$$

the following expression for the time dependent position is obtained:

$$x(t) = \frac{e/m_e}{(\omega_0^2 - \omega^2)} E(t) \quad (2.14)$$

The dipole moment associated with a charge  $e$  displaced by  $x(t)$  is:

$$\mu_x(t) = qx(t) \quad (2.15)$$

If there are  $N$  oscillators per unit volume orientated in the  $x$  direction, the total polarization is given by:

$$P_x(t) = N\mu_x(t) \quad (2.16)$$

and hence:

$$P_x = \frac{e^2 NE_x(t) / m_e}{(\omega_0^2 - \omega^2)} \quad (2.17)$$

Using the relation

$$(\varepsilon - \varepsilon_0) \underline{E} = \underline{P} \quad (2.18)$$

and the fact that  $n^2 = \varepsilon / \varepsilon_0$  gives

$$\varepsilon = \varepsilon_0 + \frac{\underline{E}(t)}{\underline{P}(t)} = \varepsilon_0 + \frac{e^2 N / m_e}{(\omega_0^2 - \omega^2)} \quad (2.19)$$

$$n^2(\omega) = 1 + \frac{Ne^2}{\varepsilon_0 m_e} \left( \frac{1}{\omega_0^2 - \omega^2} \right) \quad (2.20)$$

Equation 2.20 is the dispersion equation which gives the frequency dependence of the refractive index of a material and according to this analysis, is a purely real number which tends towards infinity when  $\omega = \omega_0$ . This resonance frequency corresponds to the transition frequency  $\omega_0 = \frac{\Delta E}{\hbar}$  of a real electronic transition where  $\Delta E$  is the energy gap of the transition and is more suitably described using a quantum mechanical description which will be the subject of section 2.1.3.

### Damped oscillations and radiative decay<sup>3</sup>

In a real atom, the electron cloud oscillations must lose energy in some manner and thus a real atomic system behaves as a damped driven oscillator. It is then necessary to include a damping term in the equation of motion which may now be written as:

$$\frac{d^2x(t)}{dt^2} + \gamma \frac{dx(t)}{dt} + \omega_0^2 x(t) = -\frac{e}{m} E_x(t) \quad (2.21)$$

where  $\gamma$  is the damping rate of the oscillator. The electronic displacement  $x(t)$  in an undriven system will, once disturbed at  $t=t_0$  oscillate and decay according to:

$$x(t) = x_0 \exp\left[-\left(\frac{\gamma}{2}\right)t + i\omega_0' t\right] \quad (2.22)$$

where  $\omega_0'$  is the resonant frequency of the damped oscillator which in the limit of weak damping is approximately equal to the resonant frequency of the undamped system. The damping rate could also be written as an inverse lifetime  $\tau$  such that the total energy,  $U$  of the oscillator decays according to:

$$U(t) = U(t_0)e^{-\gamma t} = U(t_0)e^{-t/\tau} \quad (2.23)$$

In light of this damping term, the relationship between the applied electric field and the polarization is not only frequency dependent but also complex. Stated another way, the dipole response can be divided into an in-phase component (real) which follows the driving field and an out of phase component which constitutes an absorptive process (imaginary). Having absorbed some of the energy of the impinging wave, the dipole re-radiates according to Eq. 2.23

The electric susceptibility  $\tilde{\chi}(\omega)$ , which is the complex, frequency dependent response function of a material to an applied electric field may be written in terms of the now complex refractive index as:

$$\tilde{\chi}(\omega) = \tilde{n}(\omega)^2 - 1 \quad (2.24)$$

and

$$\underline{\tilde{P}} = \tilde{\chi}(\omega)\epsilon_0\underline{\tilde{E}} \quad (2.25)$$

Using Eq. 2.18, the electric permittivity of the medium in terms of this susceptibility may be written as:

$$\tilde{\epsilon} = \epsilon_0(1 + \tilde{\chi}) \quad (2.26)$$

The susceptibility can then be written as

$$\tilde{\chi}(\omega) = \frac{Ne^2}{m_e\epsilon_0} \frac{1}{\omega_0^2 - \omega^2 + i\gamma\omega} \quad (2.27)$$

Thus, it can be seen that the complex susceptibility of a material fully describes the materials response to an applied electric field. The real part of the susceptibility is related to how the local electric field within the atoms changes the propagation of the electromagnetic wave as it passes through it, while the imaginary part of the susceptibility describes how the atoms can absorb and re-radiate a wave travelling through the medium.

### 2.1.3 Quantum description: electronic transitions

When the frequency of the impinging light approaches a resonant transition in the material the imaginary part of the refractive index approaches infinity and a better description can be obtained using quantum mechanics which can deal more readily with resonant transitions within the electronic system.

In general, any substance will have several resonant frequencies associated with transitions between the energy eigenstates  $\psi$  within the material. With this in mind, the susceptibility can be re-written in terms of the sum of these states:

$$\tilde{\chi}(\omega) = \frac{Ne^2}{m_e\epsilon_0} \sum_n \frac{f_n}{\omega_{0n}^2 - \omega^2 + i\gamma\omega_n} \quad (2.28)$$

Where  $\omega_n$  denotes the resonant frequency of the  $n^{\text{th}}$  transition. The terms  $f_n$  which satisfy  $\sum_n f_n = 1$  are called the oscillator strengths or transition probabilities of the transitions.

<sup>4</sup>According to quantum mechanics, the transition probability or transition rate in the dipole approximation between two states  $i$  and  $j$  is denoted  $B_{ij}$  and is proportional to,

$$B_{ij} \propto |\mu_{ji}|^2 \quad (2.29)$$

where  $\mu_{ji}$  is the magnitude of the vector,

$$\underline{\mu}_{ji} = e \int_V u_j^* \underline{r} u_i dV \quad (2.30)$$

Where  $*$  denotes the complex conjugate and  $u$  represents the amplitudes of the wavefunctions of the initial and final states. The vector quantity in Eq. 2.30 is called the transition dipole between states  $i$  and  $j$  and its magnitude depends strongly on the type of material under study.

## 2.2 Organic materials

### 2.2.1 Introduction

Organic materials are those whose chemistry is based on carbon. Carbon can form into a myriad of structures due to its ability to form single, double and triple bonds with itself and other atoms leading to the vast array of organic materials that are evident in the natural world. Organic compounds can be divided into saturated and unsaturated, the latter having at least one carbon double or triple bond. All organic materials absorb UV radiation. The presence of a double or triple bond strongly influences the wavelength at which this absorption occurs and saturated compounds generally only absorb light below 160 nm.<sup>5</sup> The photon energy at this wavelength is higher than the dissociation energy of most chemical bonds and decomposition is likely to occur. The materials studied in this thesis are organic dyes which are characterized by absorption at much longer wavelengths in the UV and emission in

the visible part of the spectrum. This is due to the high degree of conjugation in the molecules which shifts the wavelength towards the red end of the spectrum. Organic dyes come in many different forms readily emitting light from the near UV to the near IR. Some of the more notable groups of dyes are the coumarins emitting in the near UV and blue, and the xanthenes including rhodamine 6G and fluorescein emitting between 500-700 nm. The class of dyes studied in this thesis are blue-green emitting substituted stilbene molecules.

### 2.2.2 Basic concepts in organic materials<sup>6</sup>

Carbon is a unique element in its ability to form a variety of different bonds. The electronic configuration of carbon is  $1s^2 2s^2 2p^2$  which could be expected to provide a valence of 2 and allow for the formation of compounds such as  $CH_2$ . However, in ethane ( $C_2H_6$ ) for example it is energetically favourable for the carbon atom to *promote* an electron from the 2s orbital to the empty 2p orbital. The electrons arrange themselves in a process called hybridisation resulting in 4 identical hybrid  $sp^3$  orbitals which arrange themselves with one lobe pointing to the corner of a regular tetrahedron with a bond angle of  $109.5^\circ$ , as shown in Figure 2-1. Three of the hybrid orbitals on each carbon bind with the 1s electron in hydrogen leading to C-H bonds while the final  $sp^3$  orbital combines end-to-end with its equivalent on the other carbon atom forming a C-C single bond. All of these bonds are called sigma ( $\sigma$ ) bonds, and are characterized by cylindrical symmetry along the internuclear axis.

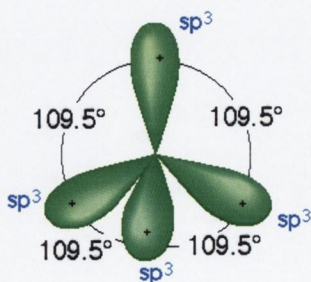


Figure 2-1 Schematic view of  $sp^3$  hybridization.<sup>7</sup>

Ethane is a saturated compound and as such requires very high energy to dissociate it making it relatively inert.

### 2.2.3 Light absorption and conjugation

Ethene  $C_2H_4$  is an example of a different type of bonding system. Ethene forms  $sp^2$  hybrid orbitals using the 2s electron and 2 of the 2p electrons leaving the other p orbital unchanged. The  $sp^2$ -orbitals arrange themselves in a plane as shown in Figure 2-2 at  $120^\circ$  angles leaving the remaining p orbital perpendicular to them. The carbon  $sp^2$  orbitals bind with the hydrogen 1s orbitals to form  $\sigma$ -bonds and additionally form an end-to-end double bond. The p-orbitals overlap in a kind of side-ways configuration to form a  $\pi$ -molecular orbit, which is recognizable by its delocalised character as shown in Figure 2-3. These  $\pi$ -bonds are much weaker than the  $\sigma$ -bonds which means they have a much lower energy and are more readily excited which extends their UV absorption wavelength further to the long wavelength end of the spectrum. All double (and triple) bonds have a  $\pi$ -bond associated with them.

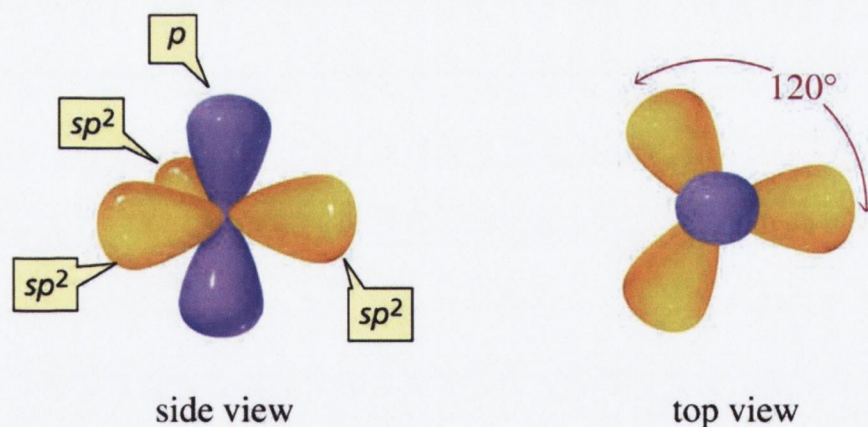


Figure 2-2 Schematic view of  $sp^2$  hybridized bonding showing also the remaining unhybridized  $p_z$  orbital<sup>7</sup>.



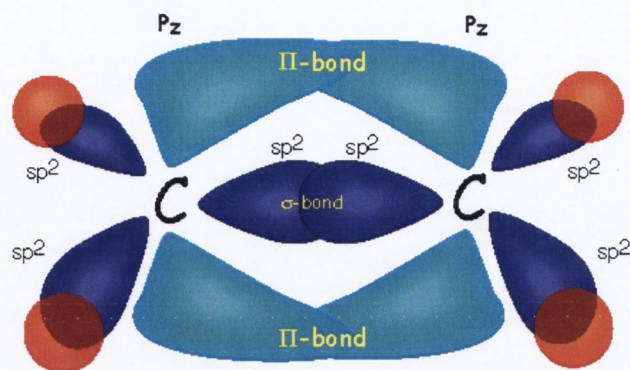


Figure 2-3 Schematic of bonding structure of ethane  $C_2H_4$ <sup>7</sup>

If two double bonds are separated by a single bond as in the molecule butadiene (Figure 2-4) the double bonds are said to be conjugated. Compounds with conjugated double bonds absorb light above 200 nm, the greater the extent of conjugation, the longer the wavelength in general.

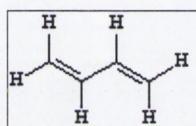
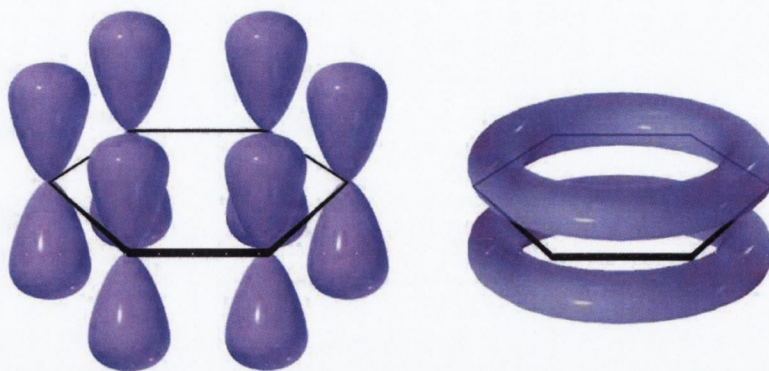


Figure 2-4 Conjugated bonds in butadiene

The delocalisation of  $\pi$ -electrons is most pronounced in the structure of benzene and its derivatives. Benzene is composed of 6 carbon atoms which are regarded as  $sp^2$  hybridized, bound in a ring with alternating single and double  $\sigma$ -bonds, with the  $\pi$  electrons completely delocalised above and below the plane of the ring as shown in Figure 2-5.

The delocalization of  $\pi$ -electrons is the key aspect to understanding the interaction of visible and near UV light with organic materials. Molecules with extensively delocalised  $\pi$ -electron systems can have the maximum of their absorption band extend far into the visible part of the spectrum. The highly polarizable  $\pi$ -electron cloud associated with conjugated systems also means that they can have very pronounced non-linear response.<sup>8</sup>



*Figure 2-5  $P_z$  orbitals in benzene resulting in highly delocalised electronic system above and below the plane of the benzene ring.<sup>7</sup>*

From the foregoing discussion, it may now be possible to make a more strict definition of the term organic *dye* as “any substance containing conjugated double bonds”.<sup>5</sup> Of course, the usefulness of a dye as a laser medium defined in this way is subject to many more constraints for example high photoluminescence quantum yield and stimulated emission-cross section. It should also be soluble in commonly available solvents and relatively immune to aggregate formation.

With this in mind, it is now appropriate to discuss the characteristic absorption and emission properties of dyes as well as other aspects of their photophysics.

#### 2.2.4 Absorption of light by organic dyes

The most salient feature of the absorption spectra of organic species as opposed to atomic materials, is the presence of wide, diffuse bands in the spectrum unlike the narrow line spectrum usually associated with atomic electronic transitions. This may readily be understood by considering the nuclear framework in which the electronic transition takes place, which may be achieved by considering the Franck-Condon principle: Because the nuclei are so much more massive than the electrons, the nuclei cannot respond over the duration of the electronic transition. The lowest electronic state in which a molecule can exist is one that contains two paired electrons of opposite spin. This type of state is called a singlet state. It is also

possible that one of the electrons can be promoted to an energetically higher state where it has a change of spin meaning that the two paired electrons have parallel spin. This is called a triplet state. Transitions between states of different multiplicity are not strictly allowed although this restriction may be relaxed in the case of strong spin-orbit coupling for example. Classically speaking, when the electron is in the electronic ground state,  $S_0$  of the molecule, the nuclei are in equilibrium and stationary. Once the electron undergoes an upwards transition due to the absorption of a photon (during which the nuclei remain stationary according to the Franck-Condon principle), there is a change in electron density which causes a change in the bond lengths in the molecule. This causes the nuclei to oscillate and what was the initially stationary bond length in the ground state becomes a turning point in the upper electronic state. From a quantum mechanical perspective, the idea of a stationary nuclear framework is unacceptable and it may be replaced by stating that the ground state configuration is the one in which the electron is in the lowest vibronic level of the singlet state, denoted  $S_{00}$ .

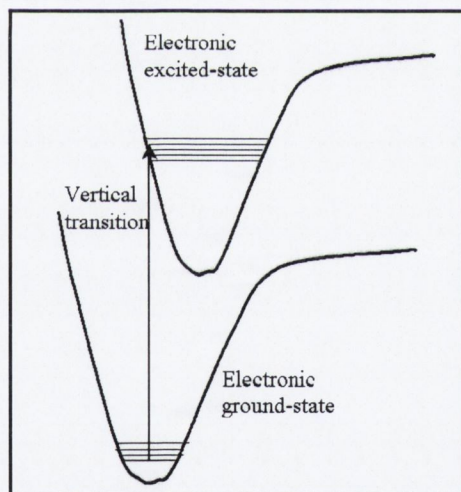


*Figure 2-6 Franck-Condon diagram showing the vertical transition of an electron in a diatomic molecule from the lowest vibronic level of the electronic ground state to some high-lying vibronic level in the first excited electronic state*

The most likely point for a transition to occur is when the nuclei have their equilibrium bond length and according to the Franck-Condon principle the nuclear framework does not change during this transition or immediately after, the electron making a vertical transition and finding itself in some highly excited vibronic level

of the upper electronic state  $S_1n$ . This transition is depicted in Figure 2-6 which is a Franck-Condon diagram for a diatomic molecule.

Of course this is not the only vibronic level accessible to the electron since the vibronic levels are very closely spaced, but the spectrum will peak at a transition whose vibrational wavefunction peaks most strongly near the equilibrium bond length. In general, a dye molecule will have many vibrational levels superimposed on any given electronic level into which the electron may go due to the different vibronic modes of which molecule is capable. In addition, collisions between the molecules, and between the molecules and the surrounding host material further broaden the individual levels. Furthermore, on top of the vibrational sub-structure, there are many modes of rotation for a given molecule many of which can couple to a given vibrational level of a given electronic level. These rotational levels are also broadened all of which results in an effective continuum of states within each electronic energy level. In the absence of any incident photons, the population of an energy level  $i$ , in thermal equilibrium with the surrounding material is given by the Boltzmann distribution:

$$N_i = N_0 \left( 1 - e^{-E_i/kT} \right) \quad (2.31)$$

Where  $N_0$  is the total population per unit volume,  $N_i$  is the population of the excited state with energy  $E_i$ ,  $T$  is the absolute temperature and  $k$  is Boltzmann's constant.

Since before absorption, most of the molecules will be in the  $S_{00}$  state, the absorption spectrum gives information about the *excited state* of the molecule. Most transitions that involve the absorption of near UV or visible light involve  $\pi$ -electron transitions of the  $\pi^* \leftarrow \pi$  (pi pi-star) type although some molecules containing oxygen for example, may have transitions due to a lone pair of non-bonding electrons ( $\pi^* \leftarrow n$ ). Although a molecule may have several electronic states into which it seems *energetically* possible to excite an electron with a UV or visible photon, not all states are accessible. The selection rules that govern which transitions are allowed depends on the symmetry of the molecule and the geometries of the ground and excited states and are the realm of group theory. This is beyond the scope of this thesis but in general, the higher the degree of symmetry in a

molecule, the more restricted the transitions. In molecules where the only symmetry operation is the identity operation, which consists of doing nothing, there are no symmetry restrictions on the electronic transitions.<sup>9</sup> In centrosymmetric molecules, the only transitions that are allowed are ones that are accompanied by a change of parity, i.e. ones that takes place between an orbital that is left unchanged under inversion in a centre of symmetry and one that has a change of sign under the same operation, and vice-versa. It should also be noted that distortions of the molecular backbone can cause a break in the symmetry and some transitions may become weakly allowed.

The strength of the absorption of electromagnetic radiation by a molecule, is described by a molecular absorption cross-section<sup>4,10</sup> which can be thought of as an area of capture for an incident photon of wavelength  $\lambda$ . In terms of the transition rate  $B$  between levels 1 and 2 as defined in Eq. 2.29, the cross-section can be defined according to:

$$\sigma = \frac{B_{21}}{F} \quad (2.32)$$

where  $F$  is the photon flux and in terms of a change of intensity, the cross-section is written:

$$I(\lambda, d) = I(\lambda, 0)e^{-N\sigma(\lambda)d} \quad (2.33)$$

Where  $I(\lambda, 0)$  is the incident light intensity,  $N$  is the number of absorbing molecules in  $\text{cm}^{-3}$ , and  $d$  is the sample thickness in cm. The absorption cross section is measured in  $\text{cm}^2$ . Good laser dyes have an absorption cross-section of the order of  $10^{-16} \text{cm}^2$ .

## 2.2.5 Relaxation and deactivation pathways for excited molecules

As stated in the previous section, the recently excited molecule finds itself in a non-equilibrium Franck-Condon state immediately after excitation. The molecule then relaxes very rapidly ( $10^{-13}$  to  $10^{-11}$  s) and non-radiatively to the lowest vibronic level of the excited state via collision and/or dipolar-relaxation via surrounding

solvent/matrix molecules. Once it has reached this level, there are several paths that the molecule can follow if left to decay spontaneously and these are depicted in the Jablonski diagram of Figure 2-7.

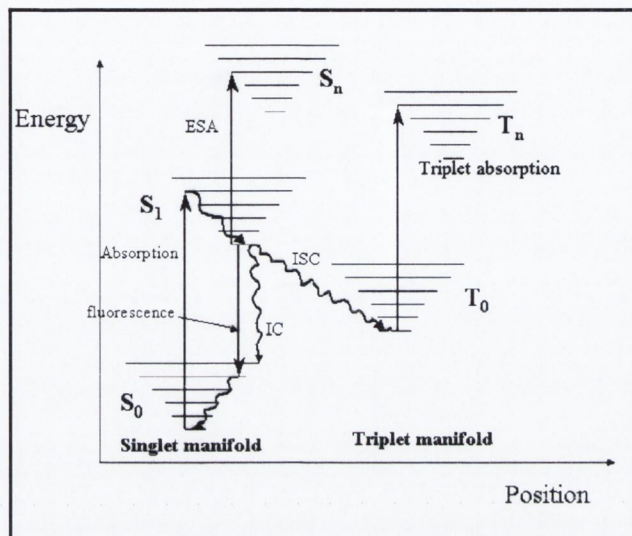


Figure 2-7 Jablonski diagram depicting some of the different photophysical processes seen in molecules. IC: internal conversion, ISC: intersystem crossing, ESA: excited state absorption

The most straightforward of these processes is the *radiative* decay of the molecule into an excited state of the ground state by spontaneous emission of fluorescence. Since this normally occurs from the lowest vibrational level of the excited state manifold to several or all of the vibronic levels of the ground state, the fluorescence spectrum provides information about the vibronic energy distribution of the *ground* state. In addition, the energy lost by the molecule in reaching thermal equilibrium in the  $S_1$  state manifests itself as a red-shift in the emission spectrum relative to the absorption spectrum which is termed the Stokes shift. Greater Stokes shift implies lower ground state re-absorption of the emitted fluorescence. In organic materials the radiative transition takes place with a lifetime  $\tau_{rf}$  of the order of 1-100 ns and is directly related to the oscillator strength of the transition which for a molecular material may be expressed by the “Strickler and Berg” formula:<sup>11</sup>

$$\frac{1}{\tau_{rf}} = 2.880 \times 10^{-9} n^2 \left\langle \tilde{\nu}_f^{-3} \right\rangle_{AV}^{-1} \int \varepsilon d \ln \tilde{\nu} \quad (2.34)$$

Where  $n$  is the refractive index,  $\left\langle \tilde{\nu}_f^{-3} \right\rangle_{AV}^{-1}$  is the reciprocal of the mean of  $\tilde{\nu}^{-3}$  in the fluorescence spectrum where  $\tilde{\nu}$  is the wavenumber,  $\varepsilon$  is the molar extinction coefficient measured in litre/(cm mole).

In addition to spontaneous emission,<sup>12</sup> there also exists the possibility that the electron can tunnel directly to the ground-state in a process called internal conversion if there is sufficient overlap in the wave-functions of the initial and final states. Internal conversion involves the radiation of heat into the surrounding environment and often involves large amplitude motion of the whole molecule.

The transition from the excited singlet state to the triplet ground state is called intersystem crossing and is not spin allowed, however perturbations such as spin-orbit coupling due to the presence of atoms with high atomic number in the molecule may induce it. In fact, phthalocyanines with heavy central metals have been designed to increase this transition probability for applications in optical limiting.<sup>13</sup> Once in the triplet state the molecule may absorb light and make a transition to a higher triplet level. Indeed this transition energy often coincides with the spontaneous emission spectrum from the molecule and can be a very troublesome source of fluorescence and gain quenching. The other route for the molecule in this triplet state is that of phosphorescence which involves a radiative transition to the singlet ground state and is also a spin forbidden transition, since it involves a transition between two states with difference multiplicity. The result of this is the much longer lifetime associated with phosphorescence as compared with fluorescence lifetimes; of the order of  $\mu$ s-ms and in some extreme case, hours and even days.

There is also the possibility of excited state absorption of either the incident beam or the fluorescence from other molecules, which will raise the molecule to some higher lying singlet state. In many cases, the electron will return non-radiatively to the  $S_1$  state with a quantum yield of less than 100 %.

All of the processes mentioned above compete with the spontaneous emission to give a quantum yield of less than 100 %. The quantum yield may be defined as:

$$\phi_f = \frac{1/\tau_{rf}}{1/\tau_{rf} + 1/\tau_{nr}} = \frac{\tau_{pl}}{\tau_{rf}} \quad (2.35)$$

Where  $\tau_{nr}$  is defined as the lifetime associated with all the non-radiative processes mentioned above and  $\tau_{pl}$  is the measurable photoluminescence lifetime.

## 2.2.6 Induced transitions and stimulated emission

As outlined above, an atom or molecule in the ground state can undergo a transition to a higher excited state under the influence of an external electromagnetic field, by absorbing a photon of the appropriate energy which is a stimulated absorption process and depends on the energy density of the incident field. From there it can undergo a downward transition with the emission of a photon via spontaneous emission which is independent of the energy density of the incident electromagnetic field. The final deactivation process that has not been yet mentioned but is of central importance to the study of optical gain is that of *stimulated emission* where an incident photon induces a downward radiative transition in a molecule already in an excited state producing a photon that is of the same wavelength and in phase with the incident photon. The transition rates due to these processes may be written:

$$\left(\frac{dN_1}{dt}\right)_{abs} = -B_{21}N_1u_\nu \quad (2.36)$$

$$\left(\frac{dN_2}{dt}\right)_{stim} = -B_{12}N_2u_\nu \quad (2.37)$$

$$\left(\frac{dN_2}{dt}\right)_{spont} = -A_{12}N_2 \quad (2.38)$$

Where  $N_i$  denotes the population of the upper or lower level,  $u_\nu$  is the spectral energy density, the subscripts *abs*, *stim*, and *spont* refer to the processes of stimulated absorption, stimulated emission and spontaneous emission respectively.



The coefficients  $A_{ij}$  and  $B_{ij}$  are referred to as Einstein's A and B coefficients and give the transition probability per unit time of a given transition.

Assuming that the atomic or molecular system is in thermal equilibrium, the rate of upward transitions must equal the rate of downward transitions, therefore:

$$B_{21}N_1u_\nu = B_{12}N_2u_\nu + A_{12}N_2 \quad (2.39)$$

Dividing across by  $N_1$  and rearranging gives the relative population of the upper and lower level:

$$\frac{N_2}{N_1} = \frac{B_{21}u_\nu}{B_{12}u_\nu + A_{12}} \quad (2.40)$$

This expression should be equal to the Maxwell-Boltzman population distribution for 2 levels in thermal equilibrium:

$$e^{-h\nu_{21}/kT} = \frac{B_{21}u_\nu}{B_{12}u_\nu + A_{12}} \quad (2.41)$$

Solving for  $u_\nu$  gives:

$$u_\nu = \frac{A_{12}/B_{12}}{\left(\frac{B_{21}}{B_{12}}\right)e^{h\nu_{21}/kT} - 1} \quad (2.42)$$

Here it may be pointed out that as  $T \rightarrow \infty$ , the spectral energy density should also approach infinity, and the only way that this will be the case is if:

$$B_{21} = B_{12} = B \quad (2.43)$$

and since the  $B$  coefficients are independent of temperature, this must also be true at all temperatures. This means that the probability of stimulated emission is identical to that of stimulated absorption. This also implies that the stimulated emission cross-section is of the same order of magnitude as the absorption cross-section for a given transition.

## References

- <sup>1</sup> A. Yariv, *Optical Electronics in Modern Communications 5<sup>th</sup> Ed.*, (Oxford University Press, Oxford, 1997).
- <sup>2</sup> E. Hecht, *Optics 3<sup>rd</sup> Ed.*, (Addison-Wiley, Harlow, 1998).
- <sup>3</sup> A. E. Siegman, *Lasers*, (Oxford University Press, Oxford, 1986).
- <sup>4</sup> O. Svelto, *Principles of Lasers 2<sup>nd</sup> Ed.*, (Plenum Press, New York and London, 1986).
- <sup>5</sup> F.P. Schäfer, in *Topics in Applied Physics: Dye Lasers 2<sup>nd</sup> Ed*, Editor: F.P. Schäfer (Springer-Verlag, Berlin, Heidelberg, New York, 1977)
- <sup>6</sup> P. Atkins, J. de Paula, *Atkins Physical Chemistry 7<sup>th</sup> Ed.*, (Oxford University Press, Oxford, 2002).
- <sup>7</sup> [http://wps.prenhall.com/wps/media/objects/724/741576/chapter\\_01.html](http://wps.prenhall.com/wps/media/objects/724/741576/chapter_01.html)
- <sup>8</sup> G.D. Stucky, S.R. Marder, J.E. Sohn, in *Linear and Nonlinear Polarizability: A Primer in Materials for Nonlinear Optic: Chemical Perspectives*, Editors: G.D. Stucky, S.R. Marder, J.E. Sohn., ACS Symposium Series, (American Chemical Society, Washington DC, 1991)
- <sup>9</sup> W. Kemp, *Organic Spectroscopy 3<sup>rd</sup> Ed.*, (Macmillan Press, Hampshire and London, 1992)
- <sup>10</sup> B.B. Snavely, in *Topics in Applied Physics: Dye Lasers 2<sup>nd</sup> Ed*, Editor: F.P. Schäfer (Springer-Verlag, Berlin, Heidelberg, New York, 1977)
- <sup>11</sup> S.J. Strickler, R.A. Berg, *J. Chem. Phys.* **37**, 814 (1962).
- <sup>12</sup> K.H. Drexhage, in *Topics in Applied Physics: Dye Lasers 2<sup>nd</sup> Ed*, Editor: F.P. Schäfer (Springer-Verlag, Berlin, Heidelberg, New York, 1977).
- <sup>13</sup> S. O'Flaherty, PhD Thesis, Trinity College Dublin, 2003.

# Chapter 3: Materials

## 3.1 Introduction

In this chapter, the materials used in this study will be introduced. Much of the work was carried out on dye-doped polymer solid-state samples so in addition to the active dye molecules, some information will be presented on the inert polymers used as host matrices. Most of the work in the subsequent chapters focuses on two molecules namely 1,4-bis(4-diphenylamino-styryl)-benzene abbreviated to SP35, and 1,4-Bis[2-[4-[N,N-di(p-tolyl)amino]phenyl]vinyl]benzene abbreviated to B2080. Additionally some measurements were performed on a closely related dye; 1,2-bis(4-diphenylaminophenyl)-ethylene or SP48 for short. The dyes emit in the blue-green spectral region.

The following sections will present the basic spectroscopic properties of the dyes under study. Much of this information will be used in later chapters.

### 3.1.1 Stilbene dyes

SP35, B2080 and SP48 can all be classed as being stilbene-like molecules. A stilbene unit is a carbon-carbon double bond attached via single carbon bonds to phenyl rings. The molecular structure of *trans*-stilbene is shown in Figure 3-1.

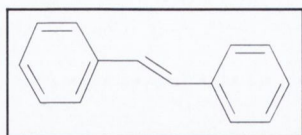


Figure 3-1 Molecular structure of *trans-stilbene*.

This molecular unit is the fundamental building block in the dyes studied in this work.

Table 3-1 Molecular structure of stilbene dyes and their full chemical names and abbreviations.

Molecular Structure	Name	Abbreviation
	1,2-bis(4-diphenylaminophenyl)-ethylene	SP48 <sup>2</sup>
	1,4-bis(4-diphenylaminostyryl)-benzene	SP35 <sup>2</sup>
	1,4-Bis[2-[4-[N,N-dimethylamino]phenyl]vinyl]benzene	B2080 <sup>3</sup>

The molecular structure of the three stilbene dyes is shown in Table 3-1. The stilbene unit forms part or all of a conjugated bridge between the symmetrically substituted diphenylamine moieties. The diphenylamine moieties are electron donating in character and the central  $\pi$ -conjugated bridge slightly electron accepting. This D- $\pi$ -D motif gives very characteristic spectroscopic properties which will be discussed in the next sections. Since the donor groups are

<sup>2</sup> Synthesised at the University of Jena by the group of Prof Hörhold.

<sup>3</sup> Tokyo Kasei Kogyo Co., Ltd.

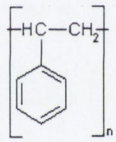
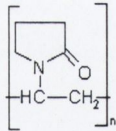
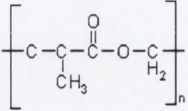
symmetrically substituted, the molecules have no net dipole in the ground state but are quadrupolar in nature.

### 3.1.2 Host polymer matrix materials

Three commercially available polymers were chosen as host matrices namely polystyrene, poly(methyl methacrylate) (PMMA) and poly(vinyl pyrrolidone) (PVP). All three are transparent in the visible region and dissolve in commonly available solvents like chloroform that are also compatible with the stilbene dyes. They also show excellent film-forming qualities.

The molecular structures of the three polymers are shown in Table 3-2.

*Table 3-2 Molecular structure of host polymer: polystyrene, PVP and PMMA. n denotes repeat unit.*

Structure	Polymer Name
	Polystyrene
	PVP
	PMMA

## 3.2 UV-Visible absorption and emission measurements

The molecular absorption cross-section of a material can be calculated from the transmission of a beam of collimated light through a sample of thickness  $d$  by:

$$\sigma(\lambda) = \frac{-\ln T(\lambda)}{Nd} \quad (3.1)$$

Where  $N$  is the number density of active molecules, which for a solution is given by:

$$N = N_A M \times 10^{-3} \quad (3.2)$$

where  $N_A$  is Avogadro's number.

### 3.2.1 Polymer Hosts

Solutions of each of the host polymers in chloroform were prepared at a concentration of 50 g/l. Films were spun on glass substrates and cured in air overnight at room temperature. UV-Visible absorption spectra of each of the polymers was taken using a Shimadzu UV-VIS spectrophotometer and an uncoated glass substrate was used as a reference sample. The absorption spectra of the three polymers is shown in Figure 3-2.

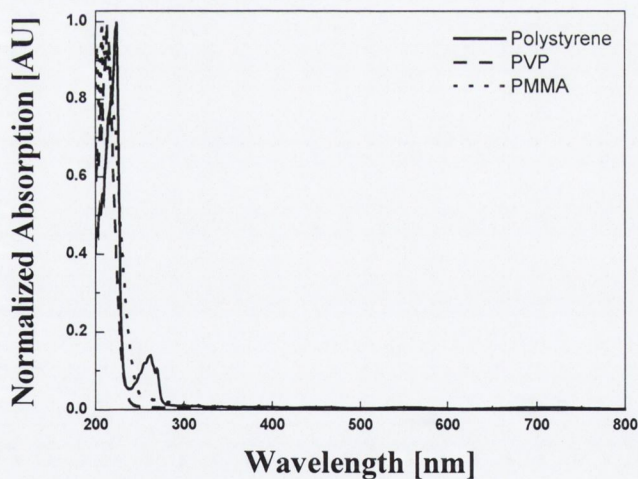


*Figure 3-2 Absorption spectra of host polymers; polystyrene, PVP and PMMA on glass substrates.*

There is no measurable absorption of any of the polymers in the region from 300 nm to 800 nm which is essential for any material under consideration as a host for a chromophore emitting in the visible region.

### 3.2.2 Absorption spectra: Dye solutions

All of the dyes studied dissolve readily in good organic solvents such as toluene, chloroform and DMSO. To prepare the solutions used for spectroscopic measurements the dyes were dissolved at a concentration of approximately  $10^{-3}$  M in the given solvent, and subsequently sonicated overnight in a sonic bath. This solution was then used as a stock solution from which lower concentrations could be made as desired. Spectrophotometric/HPLC grade solvents were used whenever possible. No further purification of the dyes was carried out, all being used as received. No evidence of scattering due to aggregation occurred in any of the solutions.

The UV-Visible absorption cross-section spectra of  $\sim 10^{-5}$  M toluene solutions of the three dyes are shown in Figure 3-3. The spectra were taken in a 1 cm quartz cuvette using a Shimadzu UV-VIS spectrophotometer with pure toluene in a matched cuvette as a reference.

All three spectra show similar spectral shape. The photophysics of D- $\pi$ -D stilbene molecules has been much studied in the literature due to their large two-photon absorption cross-section.<sup>1</sup> Absorption of UV radiation by such molecules results in a large rearrangement of the  $\pi$ -electrons due to intramolecular charge transfer (ICT) from the electron-donating terminal groups to the central  $\pi$ -bridge. The strength of this transition depends upon a number of factors.<sup>2</sup> First, the electron donating strength of the donor groups and the electron withdrawing abilities of the central bridge, which governs the *amount* of ICT associated with the transition, and also the distance over which the charge is transferred which is governed by the conjugation length of the molecule. In Figure 3-3, the strong absorption band at about 400 nm is associated with this charge transfer transition. The appreciable red-shift in absorption maximum between SP48 and the other two dyes is an effect associated with the conjugation length of the molecule. In a quasi 1-D system, the longer the conjugation length, the greater the width of the potential-well which the electron sees as it moves along the molecular backbone and hence, the longer the wavelength of absorption.<sup>3</sup> The difference in the strength of the transition between SP48 and the other two dyes is also due to the shorter conjugation length of that dye as outlined above. The difference in absorption strength between SP35 and B2080 is possibly due to the extra methyl groups which have the effect of increasing the

solubility of the dye which would reduce any effects due to aggregate formation. This could also be an effect associated with the purity of the dye. The methyl groups also have the effect of making the molecule slightly longer which is borne out by the slight red-shift (4 nm) in the absorption peak of B2080 relative to SP35. There is no measurable absorption of any of the dyes in the near IR region, which is the region of interest for two-photon absorption studies.

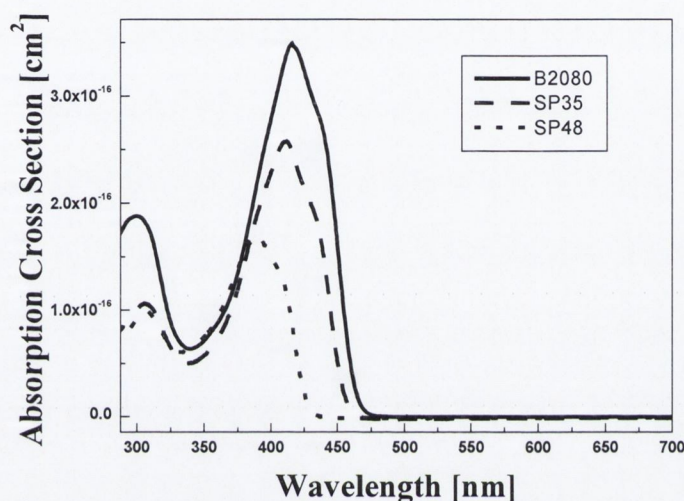


Figure 3-3 Absorption spectra of SP35, SP48 and B2080 in toluene at a concentration of  $\sim 10^{-5}$  M.

### 3.2.3 Steady-state photoluminescence: Dye solutions

Figure 3-4 shows the photoluminescence spectra of the three molecules at the same concentration ( $\sim 10^{-5}$  M) measured on a Perkin-Elmer fluorescence spectrometer. To obtain each spectrum, the molecule was pumped at the peak of the absorption spectrum.

The peaks in the emission spectra follow the same trend as the absorption with B2080 having the longest emission wavelength. The Stokes shift associated with each of the dyes is approximately 40 nm for SP48 and about 48 nm for both SP35 and B2080. This ensures low reabsorption of the dyes at the emission wavelengths. The Stokes shift is large due to the large degree of electronic rearrangement that takes place upon excitation and the subsequent large amount of rearrangement



which the molecule must undergo in the excited state before the lowest vibrational level is reached.

The vibrational substructure is more evident in the emission spectrum than in the absorption spectrum, with each of the shoulders conventionally designated as transitions from the lowest vibrational level of the excited state to one of several vibrational levels in the ground state, and may be written  $S_{10} \rightarrow S_{0n}$ . Again a possible reason for this is the very different electronic configuration of the  $S_1$  state relative to the ground state due to ICT which would remove the normal mirror image similarity between absorption and emission spectra.

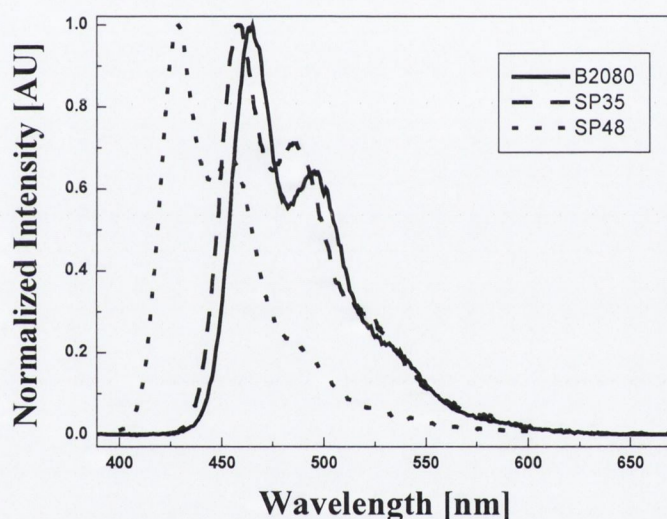


Figure 3-4 Emission spectra of SP35, SP48 and B2080 in toluene at a concentration of  $\sim 10^{-5}$  M.

#### 3.2.4 Solid state spectra

The behaviour of a molecule depends strongly on its surroundings. In solution, one manifestation of this is the solvatochromic effects such as the increase in Stokes shift with increasing solvent polarity especially in polar molecules.<sup>4</sup> Another example demonstrated by Sharafy and Muszkat<sup>5</sup> showed a strong dependence of the fluorescence quantum yield of *trans*-stilbene and some of its derivatives on the viscosity and temperature of the surrounding solvent. It was found that in more viscous solvents, the rate of internal conversion was lower since the probability and

amplitude of twisting and out-of-plane bending modes around the central double bond was reduced.

The behaviour of dyes in solid polymer hosts is not as well characterised compared to that in solution. Effects such as aggregate formation, absorption by trapped oxygen and conformational changes in the molecule can all affect the performance of the laser dye. In addition, photodegradation can have a much greater effect in a solid host compared to solution since the molecules are fixed in place and cannot be replenished as is common in solution dye lasers.<sup>6</sup>

The solid thin films used for spectroscopic measurements were made by dissolving the polymer at a concentration of 50 g/l in chloroform and adding approximately 1 wt % of dye and sonicating the solution overnight. While the solutions of polystyrene and PMMA were very transparent, the PVP solutions were very slightly cloudy which may be an indication of reduced solubility.

Good optical quality films were spun from the solutions at spin speeds varying from 600 rpm to 4000 rpm. Undoped polymer films were also spun as reference samples. All films were cured overnight at room temperature in air. The substrates used were either glass or pyrex. The final film thickness was measured using white-light interferometric profilometry. In film form, there was no visible evidence of scattering from any of the films. The absorption and emission spectra of the films were recorded as for the solutions.

### **Absorption and emission spectra-B2080**

Figure 3-5 show the absorption cross-section of B2080 in different polymer hosts on pyrex substrates.

The shape of the absorption spectrum is similar to that in toluene with the peak in the polystyrene and PVP hosts being red-shifted by about 5 nm, and the peak in PMMA blue-shifted by 2 nm. The spectrum in solid hosts is also slightly broader than in solution; a FWHM of 66 nm was measured in toluene as compared to about 70 nm in the solid host. The reason for this may be that doping of a dye into an amorphous solid could lead to increased inhomogeneous broadening because each molecule sees a different local environment.

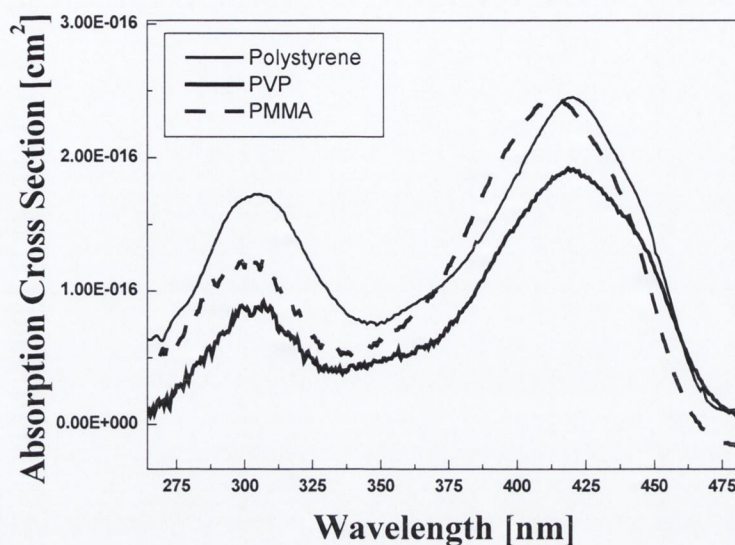


Figure 3-5 Absorption cross-section of B2080 in polystyrene, PMMA, and PVP.

The magnitude of the absorption cross-section is also considerably lower in the solid hosts than in toluene, the effect being most pronounced in PVP which is a trend that is also repeated in SP35 doped films. This reduction could be due to the reduced ability of the dye molecules to orientate themselves with the incident electric field in the solid host as compared to in solution. Additionally, since the spectrum is broadened, some reduction in the absorption peak is to be expected since it is the *integrated* absorption spectrum that gives the oscillator strength.

Figure 3-6 shows the emission spectrum of B2080 in the three different host polymers. Clearly, the emission spectrum depends much more strongly on the host polymer than the absorption spectrum with the spectrum considerably broadened in PVP and PMMA relative to polystyrene. These spectral shapes are repeated in SP35 doped films but their origin is unclear.

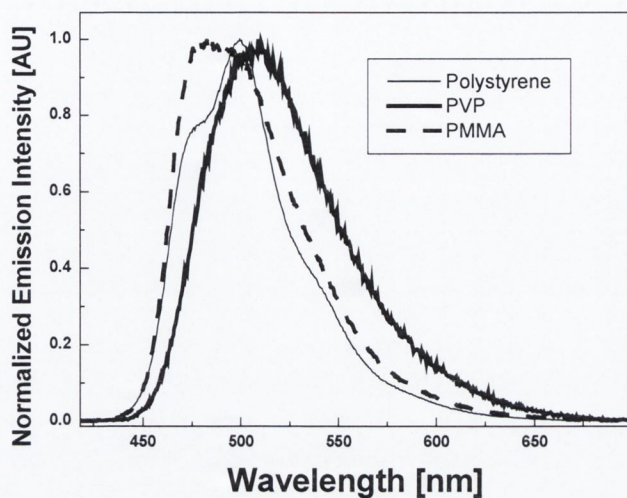


Figure 3-6 Emission spectrum of B2080 in polystyrene, PMMA and PVP.

### Absorption and emission spectra-SP35

Figure 3-7 and Figure 3-8 show the absorption and emission spectra of SP35. Similar qualitative agreement exists between these spectra and those of B2080.

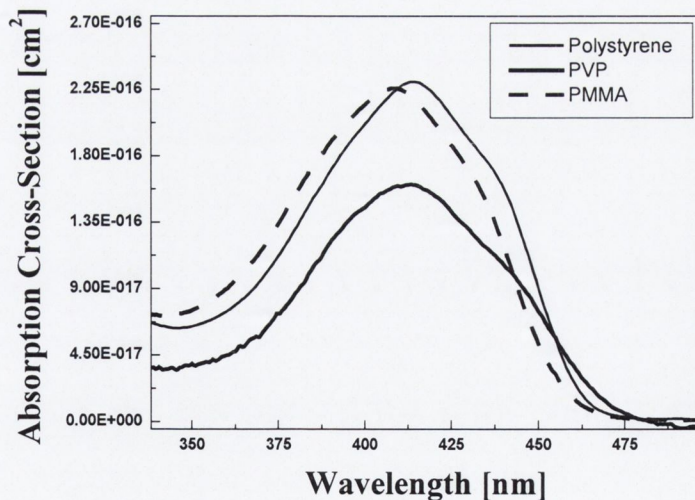


Figure 3-7 Absorption spectrum of SP35 in polystyrene, PMMA and PVP.

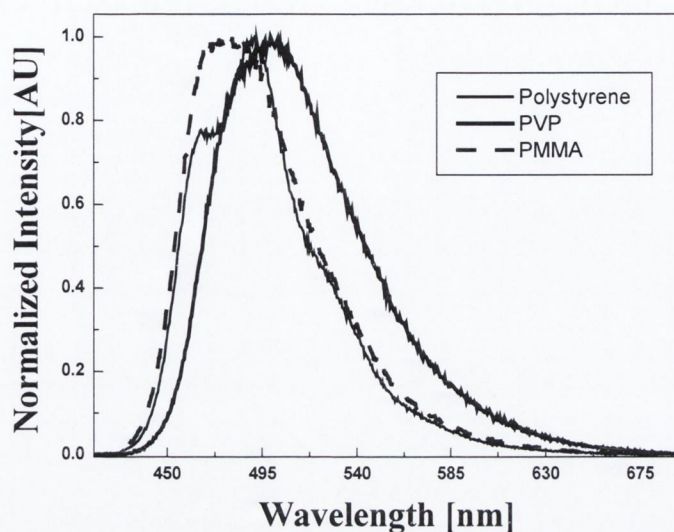


Figure 3-8 Emission spectrum of SP35 in polystyrene, PMMA and PVP.

The Stokes shifts of both SP35 and B2080 in different host polymers are shown in Table 3-3. Both molecules show similar qualitative behaviour with the Stokes shift in solid-state hosts being considerably greater than that in solution.

Table 3-3 Stokes shifts of SP35 and B2080 in different polymer hosts.

Host	Stokes shift (nm)
<b>SP35</b>	
Polystyrene	75
PVP	64
PMMA	87
<b>B2080</b>	
Polystyrene	80
PVP	67
PMMA	90

### Absorption and emission spectra-SP48

The two-photon absorption cross-section of SP48 in different host polymers is measured in Chapter 5. For that analysis, the one-photon absorption cross-section must be known. The absorption cross-section spectra of SP48 in different polymer hosts is shown in Figure 3-9. This material follows similar trends to that of B2080 and SP35 with the cross-section being slightly lower in the PVP host. One issue that affects SP48 to a much greater degree than the other two stilbene dyes is chemical stability. Since it contains one less phenylene-vinylene link, SP48 is more susceptible to torsional motion and chemical degradation. After solutions are made, the dye chemically degrades quite rapidly, at a rate that depends on the polymer in the solution.

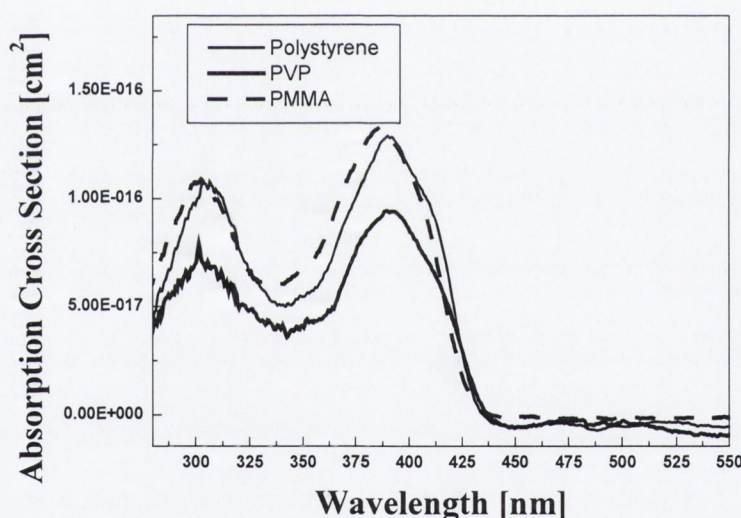
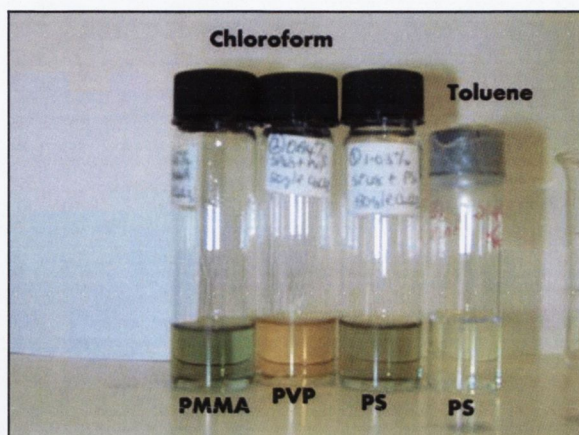


Figure 3-9 Absorption spectrum of SP48 in polystyrene, PMMA and PVP.

Figure 3-10 shows a photograph of the three chloroform solutions of SP48 and the polymers about 1 hour after sonication. Also shown is a sample of SP48 and polystyrene in toluene which is a stable solution. It is clear that there has been chemical degradation of the compound in the chloroform with the formation of some products that absorb in the visible part of the spectrum. The rate of this formation is dependent on the polymer in the solution and occurs in chloroform and not in toluene which is likely due to the slight acidity of chloroform. When preparing samples from chloroform solutions, the films are spun immediately after

sonication and the solution subsequently discarded. There is a possibility that some of the dye has degraded even at this time but it is assumed that this has occurred on a low level since there is no evidence of new absorption peaks in the spectrum of the films as shown in Figure 3-9. The undulations in the baseline of the spectrum are interference fringes that occur due to the thin film nature of the samples.



*Figure 3-10 Photograph of SP48 and polymer solutions in chloroform approximately 1 hour after sonication. Also shown is SP48 and polystyrene in toluene which is a stable solution.*

### 3.3 Photoluminescence quantum yield (PLQY)

#### 3.3.1 Introduction

While the absorption cross-section spectrum gives information about the strength of the upward transition in a particular molecule, the photoluminescence quantum yield gives information about other aspects of the photophysics of the molecule, in particular, the ratio of the radiative decay rate to the decay rates due to non-radiative processes.

The measurement of photoluminescence quantum yields was reviewed extensively by Demas and Crosby.<sup>7</sup> Their article outlines in detail the experimental procedures which should be used to accurately measure PLQY in solution. Issues which arise include correction factors for refractive index, reabsorption rates and nonlinearity of detectors. The most commonly used method for carrying out this measurement is the use of a standard material with which to compare the fluorescence and absorption of the analyte. The biggest difficulty with this method is the absence of

suitable, well-characterized standards. The quantum yield is well known to be critically dependent on solvent polarity, viscosity and temperature as well as the method of sample preparation, for example the inclusion of a nitrogen purge in the sample preparation to remove dissolved oxygen. In addition, the measurement of PLQY in solid-state samples is further complicated by the asymmetry of thin solid film samples, and the propagation and reabsorption of light in the film. The standard procedure for PLQY solid films makes use of an integrating sphere.<sup>8</sup>

### Standard Method

Measurements of the PLQY of B2080 in solution have been carried out using the method of comparison with a standard. The standard used for this measurement was coumarin120 in methanol which has a quantum yield of 77 % according to reference 9 although the details of sample preparation are not given in that paper. This standard was chosen due to the reasonably good overlap between the absorption and emission spectra of the two materials.

The method adopted was as follows.<sup>10</sup> Solutions of B2080 in toluene and coumarin120 in methanol were made such that the absorbance in a 1 cm cuvette of the solutions was about 0.5 at the reference wavelength, i.e. the wavelength at which the samples will be pumped to observe the fluorescence. In this case, the wavelength chosen was 355 nm, the 3<sup>rd</sup> harmonic of a Nd:YAG laser which is used as a pump source in subsequent experiments. The absorption spectra of both solutions were recorded and are shown in Figure 3-11.

The solutions were then diluted by a factor of 10 so as to be suitable for fluorescence measurements. A low concentration is necessary in order to minimize re-absorption effects. Both solutions were then excited at the reference wavelength and the emission spectra recorded. The fluorescence spectra are shown in Figure 3-12.

The quantum yield can then be calculated from:

$$\phi_{sample} = \frac{A_{ref}}{A_{sample}} \frac{F_{sample}}{F_{ref}} \left( \frac{n_{sample}}{n_{ref}} \right)^2 \phi_{ref} \quad (3.3)$$



Where the subscripts *sample* and *ref* refer to the analyte and reference material respectively,  $\phi$  is the quantum yield,  $A$  is the absorbance of the sample at the reference wavelength,  $F$  is the integrated emission spectrum, and  $n$  is the refractive index of the solvent.

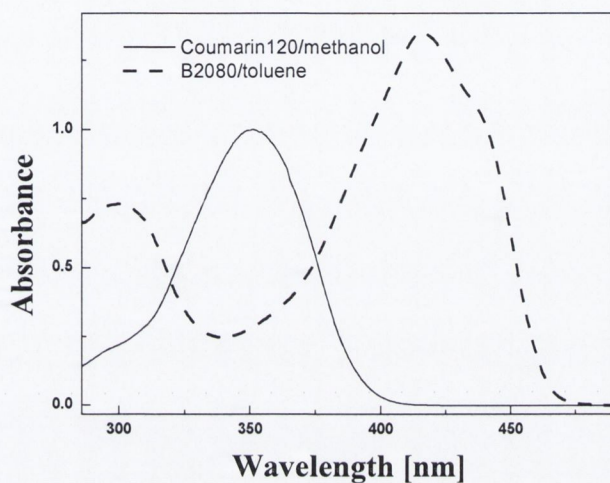


Figure 3-11 Absorption spectra of B2080 in toluene and coumarin120 in methanol measured in a 1 cm quartz cuvette

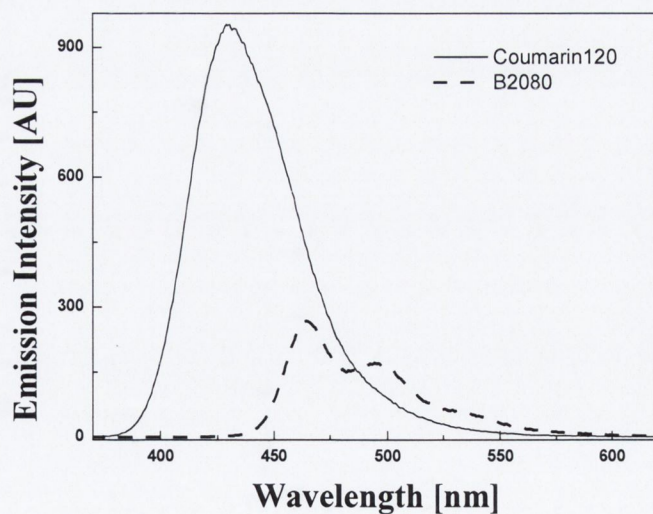


Figure 3-12 Fluorescence spectra of coumarin120 and B2080 when pumped at 355 nm.

Using this method, the PLQY of B2080 in toluene under normal atmospheric conditions was calculated to be 71 %. This is somewhat less than has been measured in the literature for similar molecules,<sup>2</sup> however, all measurements were carried out in air with no attempt being made to remove oxygen from the solution which can strongly affect the quantum yield. Also, this method naturally depends on the accuracy with which the reference sample was measured.

### 3.4 Conclusion

This chapter has introduced the materials under investigation as well as their basic spectroscopic properties and the important aspects of their photophysics. The information contained in it will be used in subsequent chapters for qualitative and quantitative analysis.

## References

- <sup>1</sup> M. Albota, D. Beljonne, J.-L. Bredas, J.E. Ehrlich, J.-Y. Fu, A.A. Heikal, S.E. Hess, T. Kogej, M.D. Levin, S.R. Marder, D. McCord-Maughon, J.W. Perry, H. Roeckel, M. Rumi, G. Subramaniam, W.W. Webb, X.-L. Wu, C. X, *Science* **281**, 1653 (1998).
- <sup>2</sup> M. Rumi, J.E. Ehrlich, A.A. Heikal, J.W. Perry, S. Barlow, Z. Hu, D. McCord-Maughon, T. C. Parker, H. Röckel, S. Thayumanavan, S.R. Marder, D. Beljonne, J.-L. Bredas, *J. Am. Chem. Soc.* **122**, 9500 (2000).
- <sup>3</sup> F.P. Schäfer, in *Topics in Applied Physics: Dye Lasers 2<sup>nd</sup> Ed*, Editor: F.P. Schäfer (Springer-Verlag, Berlin, Heidelberg, New York, 1977)
- <sup>4</sup> W. Kemp, *Organic Spectroscopy 3<sup>rd</sup> Ed.*, (Macmillan Press, Hampshire and London, 1992)
- <sup>5</sup> S. Sharafy, K.A. Muszkat, *J. Am. Chem. Soc.* **93**, 4119 (1971)
- <sup>6</sup> Rodriguez M., Costela A., Garcia-Moreno I., Florido F., Figuera J.M., Sastre R., *Meas. Sci. Technol.* **6**, 971 (1995).
- <sup>7</sup> J.N. Demas, G.A. Crosby, *J. Phys. Chem.* **75**, 8 (1971).
- <sup>8</sup> L.-O. Palsson, A.P. Monkman, *Adv. Mater.* **14**, 757 (2002).
- <sup>9</sup> Z.-l. Huang, N. Li, Y.-F. Sun, H.Z. Wang, H.-c. Song, Z.-l. Xu, *Journal of Molecular Structure* **657**, 343 (2003).
- <sup>10</sup> S.F. Forgues, D. Lavabre, *J. of Chem. Ed.* **76**, 1260 (1999).

# Chapter 4: Gain Spectroscopy

## 4.1 Introduction

The focus of this chapter is the characterisation of B2080 as an amplifying medium in the solid state. The chapter will begin with a general discussion of lasing and amplification in dye molecules. The variable stripe length method is employed to measure the modal gain of thin films of B2080 at a number of pump fluences from which the stimulated emission cross-section is extracted. In addition, low threshold lasing is shown in a basic structure which behaves as a simple Fabry-Perot oscillator. The chapter will finish with a discussion and comparison of this study with similar works in the literature.

## 4.2 The organic dye: A four-level laser system

The general electronic structure of an organic dye and the transitions between the energy levels therein were outlined in chapter 2. As shown, under excitation by an external light source, the molecule is excited to a high-lying vibronic level of the excited state from where it rapidly relaxes to the lowest vibronic level. Upon deactivation by spontaneous or stimulated emission, the molecule reaches a high lying vibronic level of the ground state which it quickly leaves to return to the ground state. Thus described, an organic dye behaves as a four-level laser system<sup>1</sup>

which is depicted schematically in Figure 4-1. In this analysis, it has been assumed that there is a negligible population residing in the triplet state. This is a reasonable assumption when the pump light source is pulsed with a rise time considerably shorter than the intersystem crossing rate.

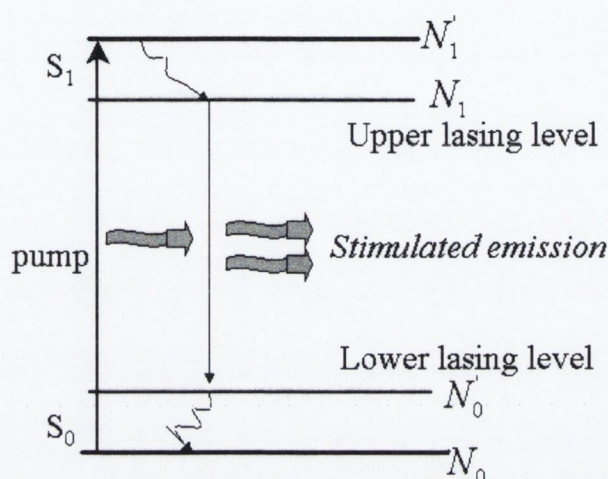


Figure 4-1 Schematic diagram of organic four-level laser system.

The rate equations for the population densities of the upper and lower lasing levels may be written:

$$\frac{dN_2}{dt} = N_1(\sigma_p(\lambda)I_p + \sigma_a(\lambda)I_e) - N_2\left(\sigma_e(\lambda)I_e + \sigma_{ex}(\lambda)I_e + \frac{1}{\tau_f}\right) \quad (4.1)$$

$$N = N_1 + N_2 \quad (4.2)$$

Where  $N_1$  and  $N_2$  are the populations of the lower ground state and upper lasing levels respectively,  $N$  is the total population,  $\sigma_p(\lambda)$  is the absorption cross-section at the pump wavelength,  $\sigma_a(\lambda)$  is the ground state absorption cross-section at the emission wavelength,  $\sigma_e(\lambda)$  is the stimulated emission cross-section and  $\sigma_{ex}(\lambda)$  is the excited state absorption cross-section from  $S_1$ .  $I_p$  and  $I_e$  are the pump and signal intensities respectively. It is assumed that the populations of  $N_1'$  and  $N_0'$  shown in Figure 4-1 are zero due to the rapid decay rates from these levels so the populations of only the levels  $N_0$  and  $N_1$  need be considered. Eq. 4.2 is the conservation of

particle number which simply states that the total number of active molecules is constant. The first term on the RHS of Eq. 4.1 is the rate at which molecules make upward transitions due predominantly to pump absorption but also due to reabsorption of emitted photons. The second term on the RHS of the equation represents the rate of decrease of excited state population density by stimulated emission, excited state absorption and spontaneous emission.

Rearranging Eq. 4.1 in terms of the signal intensity and assuming steady state pumping such that  $\frac{dN_2}{dt} = 0$  gives:

$$I_e (N_2 \sigma_e - N_1 \sigma_a - N_2 \sigma_{ex}) = N_1 \sigma_p I_p - \frac{N_2}{\tau_f} \quad (4.3)$$

The term in the brackets on the LHS of Eq. 4.3 represents the gain of the signal  $I_e$  due to the net pumping rate on the RHS. From these equations, it can be seen that the molecule is raised into the upper lasing level by absorption of the pump at a rate that depends on the pump intensity. From there it can undergo either spontaneous or stimulated emission, the latter obviously being preferable from the point of view of gain. Spontaneous emission in a macroscopic laser cavity represents noise as the emitted photons are not coupled to the input field and are thus emitted in all directions and bear no phase relationship to the laser signal. Hence spontaneous emission depopulates the upper lasing level without increasing the signal intensity. Also evident from these equations is the effect of ground state re-absorption, which results in a loss in signal intensity. This effect is reduced in molecules with a large Stokes shift.

### 4.3 Amplified spontaneous emission (ASE)

Sometimes called travelling wave lasing, amplified spontaneous emission is the amplification of spontaneously emitted photons as they propagate through a region of material which is pumped such that the net gain is greater than 1. It does not require optical feedback and its characteristics are a superlinear increase in emission intensity with excitation length and a narrowing of the gain spectrum with increasing intensity.

### 4.3.1 Variable stripe length method (VSM)

Monitoring the ASE intensity from a sample can give valuable information about the amplifying abilities of a material. For a small signal of intensity  $I$ , the increase in intensity with length can be written:

$$\frac{dI}{dz} = AP_0 + g_{net} I \quad (4.4)$$

where  $g_{net}$  is the net small signal gain. The assumption in this equation is that the propagation of the signal  $I$ , does not cause appreciable de-population of the excited state due to stimulated emission, i.e. that the gain is constant. This is not the case for arbitrarily long propagation lengths and saturation is evident beyond a length  $L_{sat}$  which depends on the pump intensity and the gain.  $AP_0$  is a constant proportional to the spontaneous emission rate.

A solution to this equation may be obtained by re-writing Eq. 4.4 as:

$$\frac{dI}{dz} - gI = AP_0 \quad (4.5)$$

Where the subscript on  $g$  has been dropped for brevity. This is a first order linear differential equation which can be solved using an integrating factor  $\mu$  such that:

$$\mu \frac{dI}{dz} - \mu gI = \mu AP_0 \quad (4.6)$$

The integrating factor  $\mu$  is:

$$\mu = e^{\int -g dz} \quad (4.7)$$

such that Eq. 4.6 can be re-written more simply as:

$$\frac{d}{dz}(\mu I) = \mu AP_0 \quad (4.8)$$

Integrating both sides leads to

$$e^{-gz} I = \int e^{-gz} AP_0 dz \quad (4.9)$$

which becomes:

$$I = AP_0 \left( ce^{gz} - \frac{1}{g} \right) \quad (4.10)$$

Now using the boundary condition:

$$I(0) = AP_0 \quad (4.11)$$

leads to:

$$c = \frac{1}{g} \quad (4.12)$$

and the solution to Eq. 4.10 becomes:

$$I = \frac{AP_0}{g} [e^{gz} - 1] \quad (4.13)$$

This expression gives the evolution of the signal intensity in a gain medium as a function of excitation length  $z$ . From this equation, it can be seen that by monitoring the ASE intensity from a sample as a function of excitation length, it is possible to extract the net gain by fitting the data to Eq. 4.13. This experimental technique is called the variable stripe length method (VSM) was first developed by Shaklee and Leheny.<sup>2</sup> Since then it has been widely used on both organic<sup>3</sup> and inorganic materials.<sup>4</sup>

Figure 4-2 shows a schematic representation of the experiment on a solid sample. The excitation length is varied by use of a beam block and the ASE measured as a function of this excitation length.



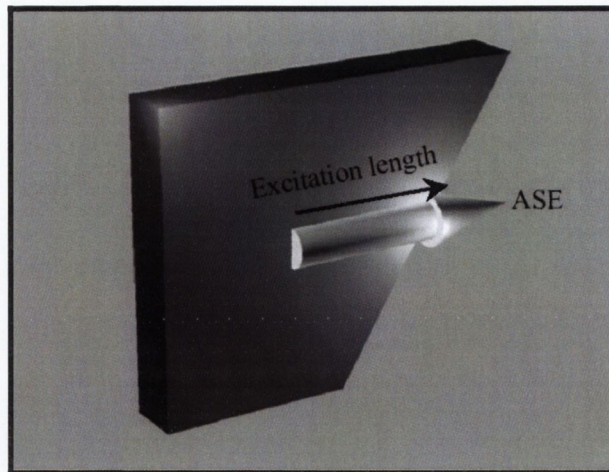


Figure 4-2 Schematic representation of variable stripe length experiment.

#### 4.4 The asymmetric slab waveguide.

The VSM is often carried out on thin film slab waveguides where the ASE is guided to the edge of the film before being detected. This is the case in this study and the waveguides were formed using B2080 doped polymer on suitable substrates. Thus formed, the samples can be described as asymmetric slab waveguides.

The dielectric slab wave-guide has been studied and discussed extensively in many texts.<sup>5,6,7</sup> The Eigenvalue equation for the propagation constants of the guided modes is obtained using a rigorous electromagnetic treatment. The discussion here will treat only the TE modes with the assumption that the solutions for the TM modes may be found using the same approach.

This study will focus on the asymmetric dielectric slab waveguide as shown in Figure 4-3 consisting of a thin planar film of active material of refractive index  $n_2$  on a dielectric substrate of refractive index  $n_3$  such that  $n_2 > n_3$ . The upper cladding layer is air of refractive index  $n_1 = 1$ . Confinement of the electromagnetic wave takes place in the  $x$ -direction by total internal reflection at the core-cladding boundary. There is no confinement of the light in the  $y$ -direction and as such all derivatives  $\partial/\partial y = 0$ . Additionally, the waveguide cladding is assumed to be semi-infinite in the  $x$ -direction such that there is no disturbance of the evanescent fields. In the case of waveguides produced in this study, the substrates are of 1 mm thickness which is

sufficiently thick that the substrate evanescent wave has decayed to an infinitesimally small amplitude before being incident on the substrate-air boundary.

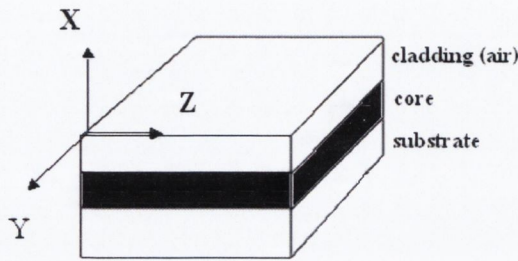


Figure 4-3 The asymmetric slab waveguide. The upper cladding layer is assumed to be air.

From a geometrical optics perspective, the guided light rays follow zig-zag paths propagating in the  $z$ -direction as shown in Figure 4-4 and suffer total internal reflection at the core-substrate and core-air boundaries.  $x = 0$  will be defined at the core-air boundary, and the core thickness is  $t$ . The angle with which the ray strikes each boundary must exceed the critical angle at that interface for total internal reflection to occur. In addition, the sum of all phase shifts incurred by the wave on travelling from  $x = -t$  to  $x = 0$  and back must be  $2\pi$ . This condition, called the transverse resonance condition, constrains the angle of incidence and hence the longitudinal propagation constants to certain discrete values. These values correspond to the guided modes of the waveguide.

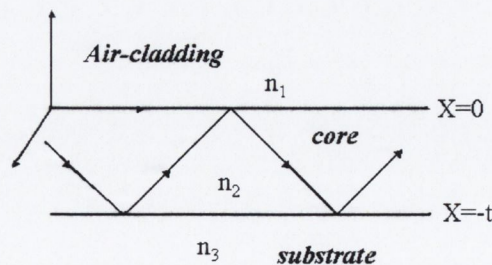


Figure 4-4 Zig-zag ray path in an asymmetric slab waveguide

As described in Chapter 2, the propagation of light through a material is best described with Maxwell's Equations and they are the starting point in the analysis of the asymmetric slab waveguide. Combining Eqs 2.1 to 2.6 and noting that the refractive index  $n$  is given by,

$$n^2 = \frac{\epsilon}{\epsilon_0} \quad (4.14)$$

the following form of Maxwell's Equations are obtained for the asymmetric slab waveguide:

$$\nabla \times \underline{H} = n_j \epsilon_0 \frac{\partial \underline{E}}{\partial t} \quad (4.15)$$

$$\nabla \times \underline{E} = -\mu_0 \frac{\partial \underline{H}}{\partial t} \quad (4.16)$$

$$\nabla \cdot \underline{E} = 0 \quad (4.17)$$

$$\nabla \cdot \underline{H} = 0 \quad (4.18)$$

Where  $n_i$  is the refractive index and the subscript refers to the layer as shown in Figure 4-4. Plane monochromatic wave propagation will be assumed, the magnetic permeability will be taken to be the same everywhere and equal to that of free space, and also the form of the electric field will be given by  $\underline{E} \propto \exp(i(\beta z - \omega t))$ , where  $\beta$  is the longitudinal propagation constant and  $\omega$  is the angular frequency.

Applying the curl operator to Eq. 4.16:

$$\begin{aligned} \nabla \times (\nabla \times \underline{E}) &= -\mu_0 \nabla \times \left( \frac{\partial \underline{H}}{\partial t} \right) = -\mu_0 \frac{\partial}{\partial t} (\nabla \times \underline{H}) \\ &= -\mu_0 n_j^2 \epsilon_0 \frac{\partial^2 \underline{E}}{\partial t^2} \end{aligned} \quad (4.19)$$

A simplification can be made by using the following expression:

$$\nabla \times (\nabla \times \underline{E}) = \nabla(\nabla \cdot \underline{E}) - \nabla^2 \underline{E} \quad (4.20)$$

Which gives:

$$\nabla^2 \underline{E} = -\mu_0 n_j^2 \varepsilon_0 \frac{\partial^2 \underline{E}}{\partial t^2} \quad (4.21)$$

Since the time dependence of  $E$  is of the form  $\exp(i\omega t)$ , defining  $k^2 = \omega^2 \mu_0 \varepsilon_0$ , noting again that all derivatives  $\partial/\partial y = 0$ , and that the  $z$ -dependence of  $E$  is of the form  $\exp(i\beta z)$ , the wave equation in the three regions of the waveguide becomes:

$$\text{Air} \quad \frac{\partial^2 \underline{E}(x, y)}{\partial x^2} + (k^2 n_1^2 - \beta^2) \underline{E}(x, y) = 0 \quad (4.22)$$

$$\text{Core} \quad \frac{\partial^2 \underline{E}(x, y)}{\partial x^2} + (k^2 n_2^2 - \beta^2) \underline{E}(x, y) = 0 \quad (4.23)$$

$$\text{Cladding} \quad \frac{\partial^2 \underline{E}(x, y)}{\partial x^2} + (k^2 n_3^2 - \beta^2) \underline{E}(x, y) = 0 \quad (4.24)$$

It is pertinent at this point to consider what range of values of the propagation constant will give solutions to these equations that correspond to guided modes in the waveguide.<sup>6</sup> For example, for  $\beta > kn_2$  then  $1/E(\partial^2 E/\partial x^2) > 0$  the solution of which is an exponential function in the core and does not correspond to a real wave. However if  $kn_3 < \beta < kn_2$ , then the solution is a sinusoid in the core region and decays exponentially in the substrate and since  $n_1 < n_3$ , it must also decay exponentially in the upper air-cladding. Thus values of  $\beta$  such that  $kn_1, kn_3 < \beta < kn_2$  provide solutions to the wave equation that are real guided modes.

#### 4.4.1 Transverse Electric (TE) modes

For transverse electric modes the only non-zero components of  $\underline{E}$  and  $\underline{H}$  are  $E_y$ ,  $H_x$ , and  $H_z$ . The magnetic field components can be written in terms of  $E_y$  as:

$$H_x = -\frac{\beta}{\omega \mu_0} E_y \quad (4.25)$$

$$H_z = -\frac{i}{\omega \mu_0} \frac{\partial E_y}{\partial x} \quad (4.26)$$

Since the magnetic components can be written in terms of  $E_y$ , all components of the field can be calculated if the  $E_y$  solutions to Eqs. 4.22-4.24 can be found.

The transverse functions  $E_y(x,y)$  can be written as:

$$\text{Air:} \quad E_y = C \exp(-qx) \quad (4.27)$$

$$\text{Core:} \quad E_y = C \left( \cos(hx) - \frac{q}{h} \sin(hx) \right) \quad (4.28)$$

$$\text{Cladding:} \quad E_y = C \left( \cos(ht) + \frac{q}{h} \sin(ht) \right) \exp[p(x+t)] \quad (4.29)$$

Where:

$$\begin{aligned} h^2 &= n_2^2 k^2 - \beta^2 \\ q^2 &= \beta^2 - n_1^2 k^2 \\ p^2 &= \beta^2 - n_3^2 k^2 \end{aligned} \quad (4.30)$$

The choice of coefficients in the equations above is such that the tangential components of the field  $E_y$ , and  $H_z$  are continuous at both interfaces. In addition, the derivative  $\delta E / \delta x$  should be continuous at  $x=0$ . Applying this to Eqs. 4.27 to 4.29 yields:

$$h \sin(ht) - q \cos(ht) = p \left( \cos(ht) + \frac{q}{h} \sin(ht) \right) \quad (4.31)$$

and

$$\tan(ht) = \frac{p+q}{h \left( 1 - \frac{pq}{h^2} \right)} \quad (4.32)$$

Equation 4.32 in combination with Eq. 4.30 is the eigenvalue equation for the propagation constants of the asymmetric slab waveguide. It may be solved most readily using a graphical method for given waveguide parameters  $n_1, n_2, n_3, \lambda, t$  by

plotting the left and right-hand side of Eq. 4.32 against  $\beta$ . The value of  $\beta$  for which the two functions intersect is an approximate solution.

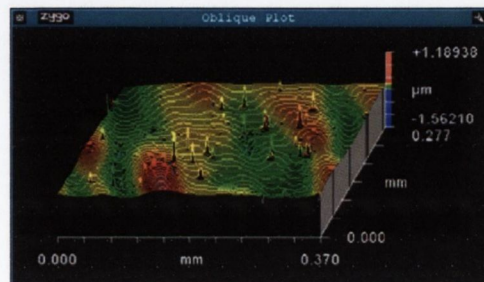
#### 4.5 Sample preparation

Thin film slab waveguides were prepared by spin coating thin films of B2080 doped into polystyrene, PVP and PMMA. All samples were doped such as to have a constant number density of  $9.5 \times 10^{18} \text{ cm}^{-3}$ . The substrates used were pyrex which has a refractive index of 1.47 and is lower than the refractive index of any of the polymers used which allows for the formation of a waveguide structure. The refractive indices of the polymers were taken from the literature and no adjustment was made for the addition of the dopant molecules since it would be expected to change the refractive index by only  $\sim 0.005$ , which in the context of this measurement was assumed negligible. The final film thickness was measured using white light interferometric profilometry. The film thickness measurements for the films are shown in Table Table 4-1

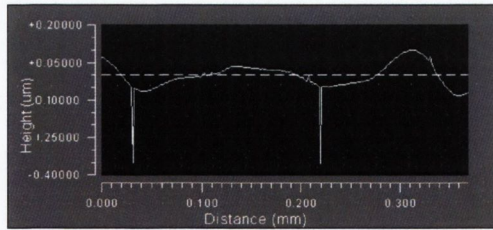
*Table 4-1 Film thickness measurements for samples.*

Host Material	Film thickness (nm)
Polystyrene	620
PVP	1350
PMMA	2100

This method also allowed a measurement of the surface profile of the films to check for inhomogeneity. A typical surface profile of each of the polymer films is shown in Figure 4-5 to Figure 4-7.

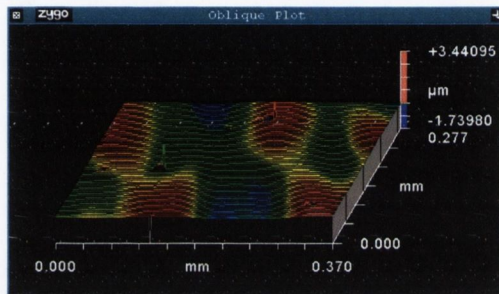


(a)

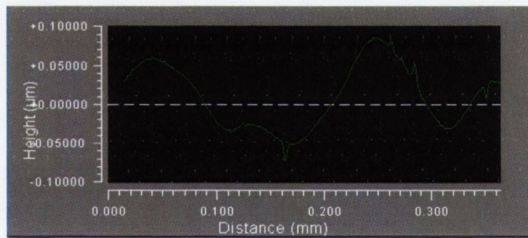


(b)

Figure 4-5 (a) Surface profile of polystyrene film and (b) cross-section of film. Spikes on surface are dust particles that have settled on the surface.

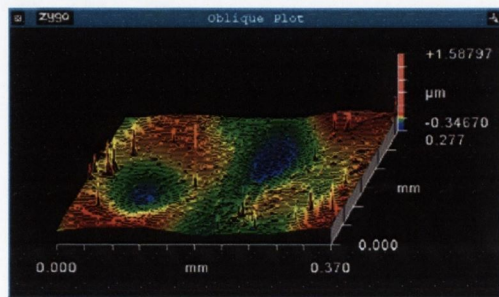


(a)

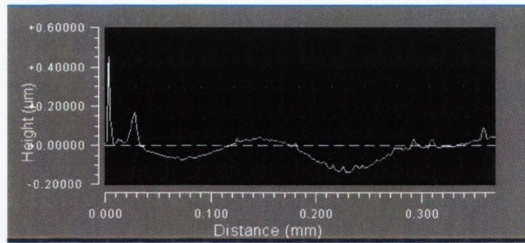


(b)

Figure 4-6 (a) Surface profile of PVP film and (b) cross-section of film. Spikes on surface are dust particles that have settled on the surface.



(a)



(b)

Figure 4-7 (a) Surface profile of PMMA film and (b) cross-section of film. Spikes on surface are dust particles that have settled on the surface.

Each of the samples has a certain amount of “waviness” on the surface although there is approximately the same degree of inhomogeneity in each of the three different polymer films which is of the order of about 6 % of the film thickness. This level of inhomogeneity does not appear to have a particularly deleterious effect on the performance of any of the waveguides.

Prior to any measurements, the samples were cleaved by scoring the back of the substrates with a diamond tip and breaking the film. It is necessary to do this because of the ridge of material that runs around the perimeter of spin cast films. Such an inhomogeneity would certainly effect the VSM measurements since the thicker area would emit far more strongly than the smoother interior causing spurious results.

The mode profile in the final films could be plotted once the film thickness was known. Figure 4-8 shows a graphical solution to the eigenvalue equation for the TE modes of a typical polystyrene waveguide. All samples produced were designed to have approximately identical mode profiles.

The calculated TE mode profile of the polystyrene waveguide is shown in Figure 4-9. The waveguide supports the two lowest order TE modes and the lowest order TM mode.



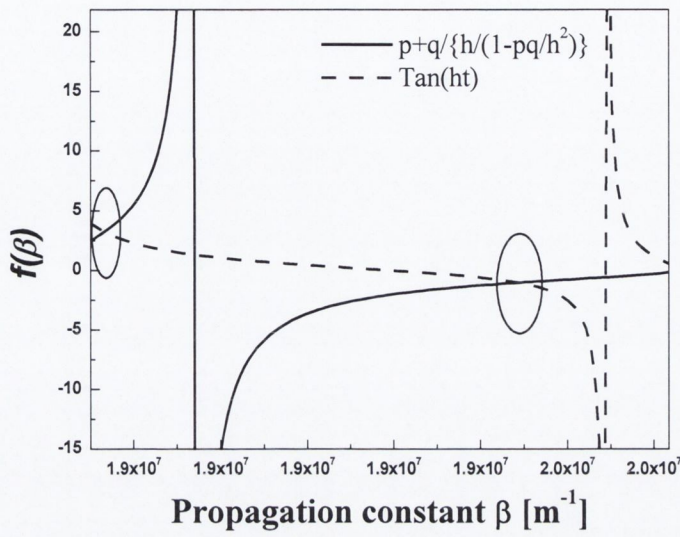


Figure 4-8 Graphical solution to the eigenvalue equation for a typical polystyrene sample. Circles mark the intersection of the two functions which represents a solution to the equation.

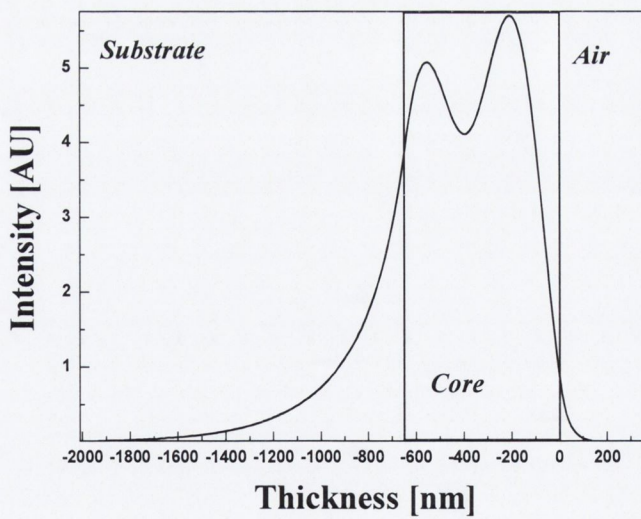


Figure 4-9 Typical TE mode profile of polystyrene asymmetric slab waveguide.

## 4.6 Modal gain measurements

### 4.6.1 Experimental procedure

The experimental setup for the modal gain measurements is shown in Figure 4-10

#### Experimental setup

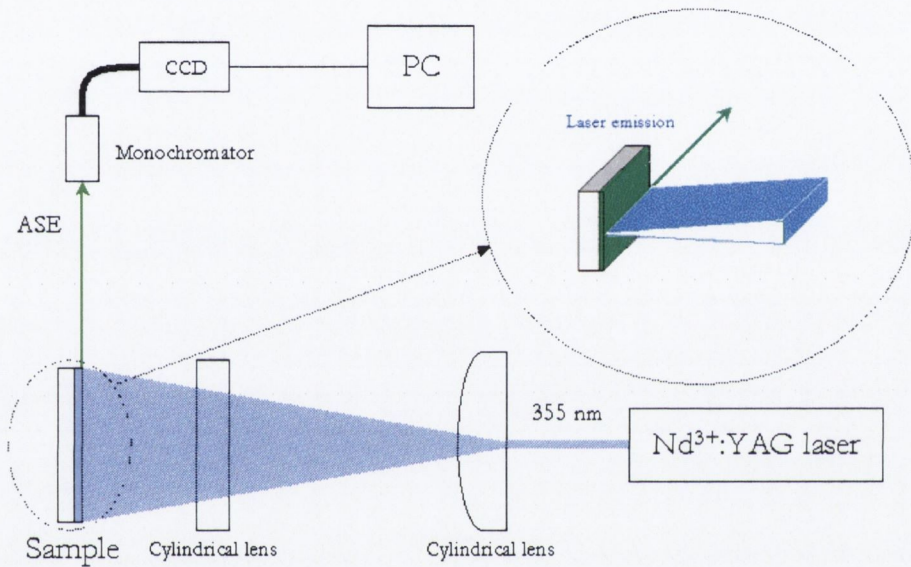


*Figure 4-10 Experimental setup used for modal gain measurements.*

The samples were pumped using the 3<sup>rd</sup> harmonic of a Nd:YAG laser with a pulse width of 3 ns and a rep rate of 10 Hz. The beam was shaped into a horizontal stripe with the use of two cylindrical lenses. The centre of the stripe was incident on the sample and the excitation length was varied by use of a straight-edged beam block which was mounted on a translational stage with a manual micrometer controller. Even though the horizontal beam profile is expected to be gaussian, the excitation lengths used in this measurement are very short compared with the full width of the beam which is 4-5 cm. For that reason, it is possible to assume that the beam intensity is constant over the excitation lengths used. The pump energy was measured using a digital energy meter and the pump fluence calculation outlined in Appendix I. To ensure that back reflections from the film facet are minimized, the sample is tilted to approximately 45 degrees as shown in Figure 4-2. The ASE was

measured from the film edge and was detected with the use of a 1 cm diameter liquid light guide coupled to a monochromator and cooled CCD array. Using the method outlined by Negro *et al.*<sup>8</sup> it was confirmed that the collection efficiency of the collection optics remained practically constant over the short excitation lengths used. The detection system resolution was approximately 1 nm.

#### 4.6.2 Initial tests

As a first test of the samples to detect for the presence of ASE an initial measurement was carried out whereby the sample was placed upright with no tilt to allow for back reflections, and the entire width of the sample was illuminated using the stripe output from the pump laser. The ASE was detected as the pump intensity was slowly increased. In the case of polystyrene films, there was a rapid collapse of the spectrum at very low pump fluences due to very strong ASE indicating the presence of considerable gain. In the case of the other two polymers, the initial signs of gain narrowing were followed by pronounced photodegradation and after a short time complete bleaching of the film was observed. Subsequently, considerable gain was measured in both the PVP and PMMA films but lasing was never observed due to this photodegradation. The reason for this requires the study of the possible photophysical mechanisms available to the molecule. The study of the photophysics of stilbenes has been underway for many years and a considerable amount of literature is available on this basic unit. In its ground state, stilbene can exist in one of two forms, namely the trans or cis form<sup>9</sup> as shown in Figure 4-11. The trans form is the lower energy state and since a large potential barrier exists between the trans and cis forms in the ground state, almost all of the dye molecules in a particular sample will be in the trans state. Under the external influence of light however, it has been shown that the molecule can undergo trans-cis isomerization.

The photophysical path for photoisomerization followed by a stilbene-like molecule is as follows: From the trans form of the ground state the molecule can absorb light in a  $\pi$ - $\pi^*$  transition to the trans form of the excited state. From there if there is sufficient energy in the system, the molecule can undergo severe torsional motion about the central double bond which can lead to a "phantom state" from which the molecule can decay non-radiatively to the cis or trans form of the ground state

(internal conversion). Obviously, this reaction is in direct competition with direct radiative decay of the molecule and would hence reduce the fluorescent quantum yield. The work of Sharafy and Muszkat<sup>10</sup> showed a marked increase in the quantum yield of stilbenes in viscous solvents due to the inhibition of this torsional motion which effectively blocks the path of trans-cis isomerization.

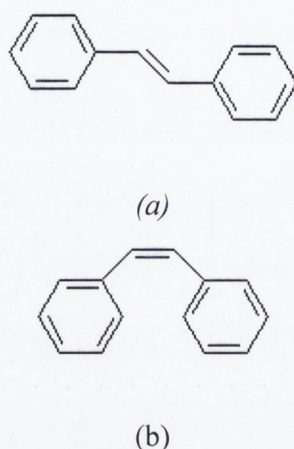


Figure 4-11 Two isomers of stilbene. (a) trans-stilbene, (b) cis-stilbene.

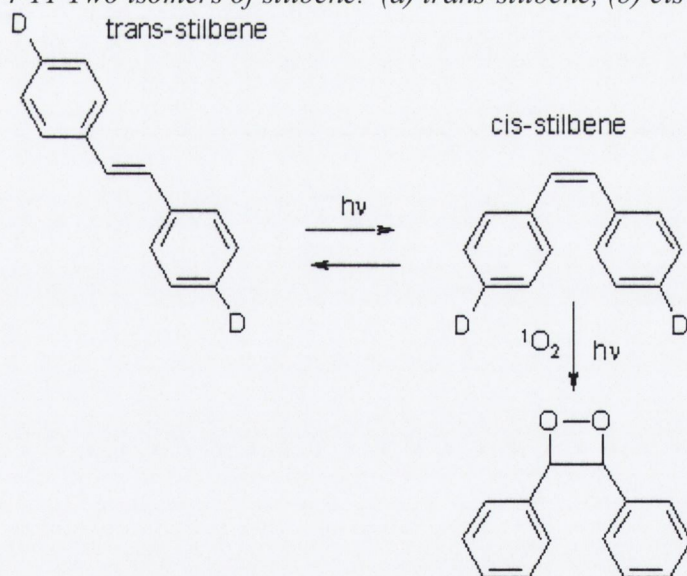


Figure 4-12 Possible route of irreversible photodegradation of symmetrically substituted stilbene molecule (adapted from reference 11).

In the case of B2080 and SP35, the large diphenylamine terminal groups would probably stabilize the molecule to a certain extent, however it has been shown that the molecules DANS<sup>11</sup> (4-N,N-dimethylamino-4' nitrostilbene) and DCM<sup>9</sup> (4-(dicyanomethylene-2-methyl-6(p-dimethyl aminostyryl)-4H-pyran) can both

undergo trans-cis isomerization in polymer hosts even though both of these molecules contain reasonably large terminal substituents.

Furthermore, it has been shown that cis-stilbene is much more susceptible to photochemical degradation than the trans form. One such photochemical reaction is shown in Figure 4-12 which is adapted from reference 11. This route requires the formation of singlet oxygen which can attack the carbon double bond and cause subsequent irreversible reactions resulting in the complete degradation of the dye. Complete bleaching was achieved in DCM doped polymer films by irradiating the sample with the green 514 nm line of an Argon ion laser. As stated above, B2080 has a much higher rate of photodegradation in PMMA and PVP than in polystyrene. Indeed, even on multiple measurements on the same spots, very little photodegradation is seen in polystyrene samples. This fact suggests that the rate of trans-cis isomerization is lower in polystyrene than in PMMA and PVP. Further study would be required to fully characterise all of the photophysical pathways that the molecules can undergo in the various environments but the pathway mentioned here is one that is certainly possible. The fact that SP48 is less stable photochemically than either SP35 or B2080 is further evidence that torsional motion is playing an important role in these processes, since it is a shorter molecule and likely to be more prone to large amplitude oscillations. Since the three polymers used are quite similar in terms of glass transition temperature, hardness and density and other mechanical properties, it seems likely that the difference between them occurs on a microscopic level, for example with the presence of micropores or microstructure.<sup>12</sup>

#### 4.6.3 Modal gain in doped polystyrene

Since polystyrene was the most suitable host for B2080 from those tested, the variable stripe length method was used to measure the net modal gain. In the initial tests, the peak of the ASE in the polystyrene hosts occurred at 501 nm indicating a peak in the gain spectrum at that wavelength. This is very close to the peak in the spontaneous emission spectrum at 500 nm.

Figure 4-13 shows the evolution of ASE intensity as a function of excitation length at a number of different pump fluences. The emission clearly follows a superlinear

increase in intensity with excitation. Also evident in this graph is the onset of saturation at longer excitation lengths. The lines in the graph are the best fit of the data to Eq. 4.13 which is restated in the inset of Figure 4-13. In order to avoid the effects of saturation, only data points below saturation were included. The last data point included in each fit is indicated in Figure 4-13 by a red arrow. The considerable errors are taken from the standard error in the fit to the data. They are large because the fitting procedure is very sensitive to very small changes in the value of a given data point. Since the films used were very thin, the signal to noise ratio is low especially at low pump fluences.

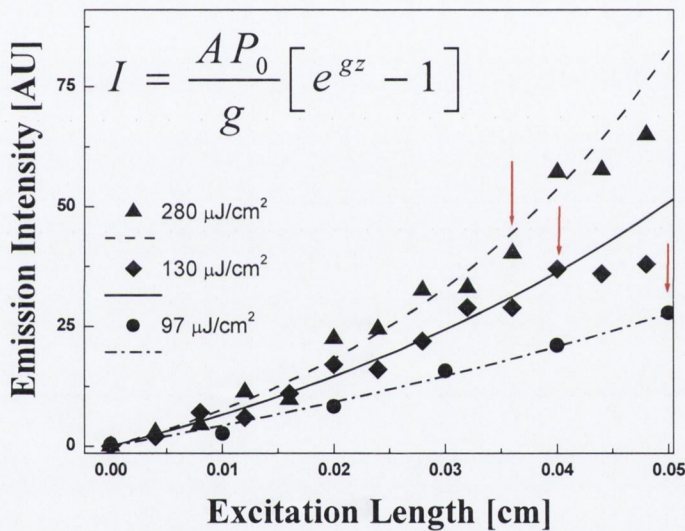


Figure 4-13 ASE intensity as a function of excitation length at pump fluences of 97  $\mu\text{J}/\text{cm}^2$ , 130  $\mu\text{J}/\text{cm}^2$ , and 280  $\mu\text{J}/\text{cm}^2$ , giving modal gain of 11  $\text{cm}^{-1}$  and 20  $\text{cm}^{-1}$  and 33  $\text{cm}^{-1}$ , respectively.

Figure 4-14 shows the measured net modal gain as a function of pump fluence. The values of the modal gain are the weighted average over several measurements. The error is the weighted average error from all the measurements. The solid line is a linear fit to the data which takes into account the error in each data point by assigning higher weight to points with lower error. At higher pump fluences the data deviates from linearity due to saturation of the pump absorption.

The induced emission cross-section is given by the following equation:

$$g_{net}(\lambda) = \sigma_e(\lambda)N_2 - \sigma_{ex}(\lambda)N_2 - \sigma_a(\lambda)N_1 - \alpha \quad (4.33)$$

where  $\sigma_e(\lambda)$  is the induced emission cross-section,  $\sigma_a(\lambda)$  is the absorption cross-section,  $\sigma_{ex}(\lambda)$  is the absorption cross-section for excited state absorption from  $S_1$  to higher singlet states,  $N_1$  and  $N_2$  are the population densities of the molecules in the first excited singlet state and ground state, respectively, and  $\alpha$  is the term describing the loss due to scattering and surface imperfection. Using Eq 4.33 and with the help of Eq. 4.2;  $N = N_1 + N_2$  gives:

$$\frac{\partial g_{net}(\lambda)}{\partial N_2} = \sigma_e(\lambda) - \sigma_{ex}(\lambda) + \sigma_a(\lambda) \quad (4.34)$$

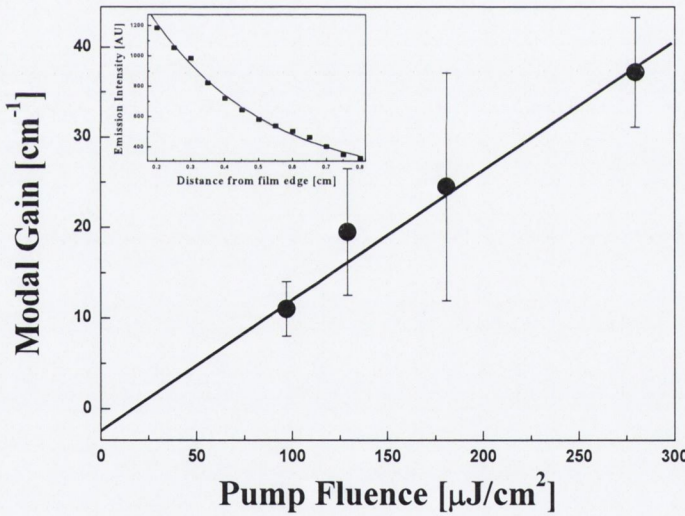
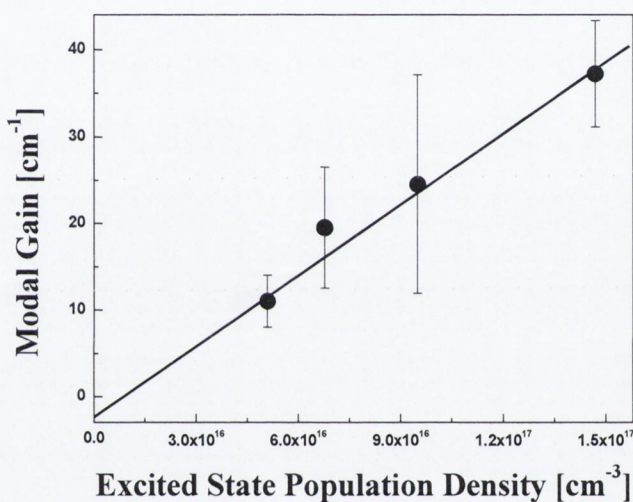


Figure 4-14 Modal gain as a function of pump fluence at 501 nm. Inset: Measured optical loss at 501 nm of  $0.33 \text{ cm}^{-1}$ .

Due to the large Stokes shift observed in B2080 it is assumed that the absorption at the peak of the gain is negligible and hence  $\sigma_a(\lambda)$  is set equal to 0. The effective induced emission cross-section is defined as

$$\sigma_e^{eff}(\lambda) = \sigma_e(\lambda) - \sigma_{ex}(\lambda) \quad (4.35)$$

Figure 4-15 shows the modal gain data replotted against excited state population density (the calculation of which is outlined in Appendix II). The line is a linear fit to the data. Using the slope of this line in combination with Eqs. 4.34 and 4.35 the effective induced emission cross-section  $\sigma_e^{eff}(\lambda)$ , is calculated to be  $(2.7 \pm 0.3) \times 10^{-16} \text{ cm}^2$  where the error quoted is the error from the straight line fit. This is in good agreement with the value of the peak absorption cross-section which has a value of  $2.45 \times 10^{-16} \text{ cm}^2$ .



*Figure 4-15 Modal gain plotted versus excited state population density. Line is a linear fit to the data yielding a value of the effective induced emission cross-section of  $(2.7 \pm 0.3) \times 10^{-16} \text{ cm}^2$ .*

Increasing the pump fluence further to  $1.1 \text{ mJ/cm}^2$  yields an average value of the modal gain of  $84 \pm 6 \text{ cm}^{-1}$  which is one of the highest measured modal gains in organic materials. This fluence value was limited by the experimental setup and is not indicative of a saturation point of the gain.

All measurements thus far have been made at the peak of the gain spectrum at 501 nm. Since the detection system used in the experiment is dispersive, it was possible to measure the gain spectrum by fitting data at each wavelength to Eq. 4.13. At each wavelength chosen, an average over the pixels on either side of the wavelength to a width of 0.5 nm was taken. Some data points in the spectrum are absent due to



very noisy pixels in the detector at that wavelength. The results of one such measurement at a fluence of  $1.1 \text{ mJ/cm}^2$  is shown in Figure 4-16. The solid line is there to guide the eye. The errors are the standard error in the fit. As can be seen, there is appreciable gain over 100 nm spectral width. Shown in the inset of Figure 4-16 is the fitting parameter  $AP_0$  which is proportional to the spontaneous emission at each wavelength for a given pump fluence and should therefore have the same spectral distribution as the spontaneous emission spectrum. The excellent agreement between the two indicates a good fitting procedure at each wavelength.

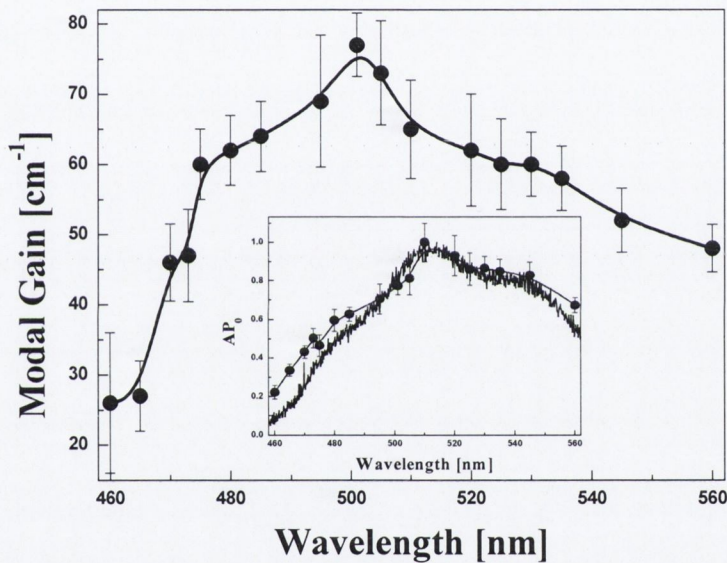


Figure 4-16 Gain spectrum of B2080 doped polystyrene waveguide at a pump fluence of  $1.1 \text{ mJ/cm}^2$ . Inset: Fitting parameter  $AP_0$  compared to spontaneous emission spectrum.

The sharp increase at the short wavelength side of the peak is due to a rapid decrease in the loss due to self-absorption. This can be seen in the loss spectrum in Figure 4-17 which was measured as described in the following section.

#### 4.6.4 Loss measurements

In order to evaluate the loss associated with the waveguides, a loss measurement was performed in the following way.<sup>13</sup> A small region of the film was weakly

excited by means of placing an aperture in the expanded laser beam. The aperture was then translated such that the photoexcited region moved further from the film edge. Some of the emitted photons are waveguided to the film edge and into the detector. In doing so, they must traverse an unexcited length of the waveguide. By measuring the emission intensity as the photoexcited region is moved from the film edge, it is possible to extract the optical loss. The loss is expected to follow the Beer-Lambert law:

$$I_{edge}(\lambda) = I_0(\lambda) \exp[-\alpha(\lambda)L] \quad (4.36)$$

Where  $\alpha$  is the loss coefficient,  $I_{edge}$  is the intensity after propagation through an unpumped region of length  $L$ ,  $I_0$  is a fitting parameter proportional to the emission intensity at the excited region. The inset of Figure 4-14 shows the emission intensity at 501 nm as a function of distance from film edge. The solid line is the best fit to Eq. 4.36, giving a loss coefficient of  $0.33 \text{ cm}^{-1}$ .

Since the emission spectrum can be measured, the whole loss spectrum can be evaluated in one measurement by fitting the data to Eq. 4.36 at each wavelength. The results of this measurement are shown in Figure 4-17. The line is there to guide the eye.

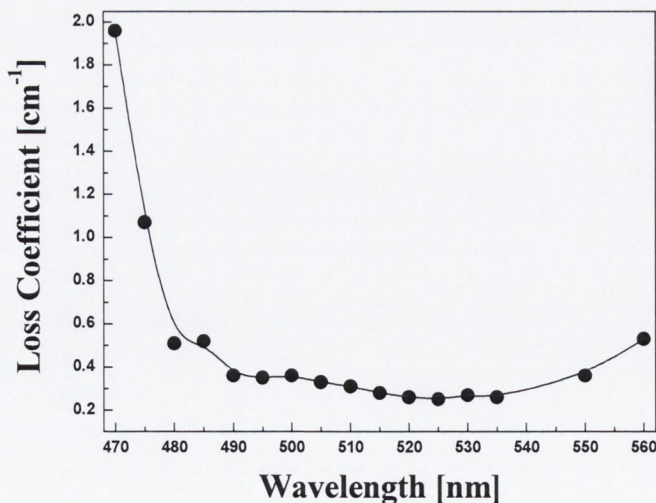


Figure 4-17 Loss spectrum of B2080 doped polystyrene waveguide. The solid line is there to guide the eye.

## 4.7 Slab waveguide laser

In order to demonstrate lasing, thin films were prepared identical to those used to measure the gain using the variable stripe length method. The laser cavity was formed by cleaving two parallel facets in the film to produce a cavity of 1 cm in length. The reflectivity at normal incidence of each facet is given by Fresnel's reflection coefficient:<sup>14</sup>

$$r = \left( \frac{n_2 - n_1}{n_2 + n_1} \right)^2 \quad (4.37)$$

Where  $n_1$  and  $n_2$  are the refractive indices of the incident and reflecting media respectively giving a reflection coefficient for a B2080-doped polystyrene waveguide of 0.05. A stripe geometry was used to transversely pump the waveguides and the emission collected as described in the previous section.

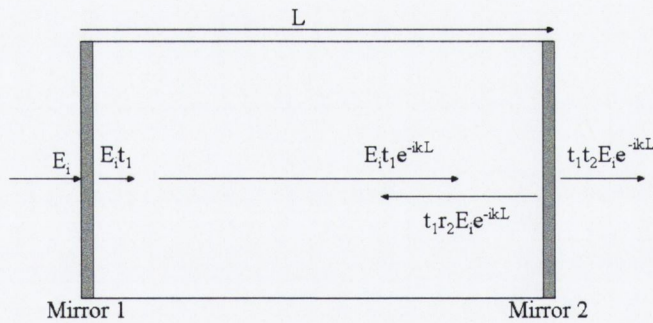


Figure 4-18 Fabry-Perot cavity of length  $L$  where  $E_i$  is the incident wave complex amplitude and  $t_n$  and  $r_n$  are the transmission and reflection coefficients respectively.

The cavity is essentially an active Fabry-Perot cavity where the facets of the film are the end mirrors as shown in Figure 4-18 and the space between the mirrors is filled with the amplifying medium.  $t_1$  and  $t_2$  are the transmission coefficients of mirror 1 and mirror 2 respectively and  $r_1$  and  $r_2$  are the reflection coefficients such that  $r_m + t_m = 1$ . The critical gain required to achieve *oscillation*, that is to say, the gain at laser threshold can be calculated under these assumptions.<sup>6</sup>

Figure 4-18 shows an incident plane wave of complex amplitude  $E_i$  on mirror 1. The transmitted portion of the wave propagates through the medium with complex propagation constant  $\tilde{k}$  and is incident on mirror 2 where part of the wave is reflected and part transmitted. The total output is the sum of all the partial waves that are transmitted at mirror 2:

$$E_t = t_1 t_2 E_i e^{-i\tilde{k}L} [1 + r_1 r_2 e^{-i\tilde{k}2L} + r_1 r_2 e^{-i\tilde{k}4L} + \dots] \quad (4.38)$$

This is a geometrical progression with a sum:

$$E_t = E_i \left[ \frac{t_1 t_2 e^{-i\tilde{k}L}}{1 - r_1 r_2 e^{-i\tilde{k}2L}} \right] \quad (4.39)$$

The complex propagation constant  $\tilde{k}$ , can be separated into real and imaginary parts.

$$\frac{E_t}{E_i} = \frac{t_1 t_2 e^{-i(k_0 + \Delta k)L} e^{(\gamma - \alpha)L/2}}{1 - r_1 r_2 e^{-2i(k_0 + \Delta k)L} e^{2(\gamma - \alpha)L}} \quad (4.40)$$

Where  $\gamma$  is the intrinsic gain and  $\alpha$  is the loss. The propagation constant has been written using the relation:

$$\tilde{k} = k_0 + \Delta k \quad (4.41)$$

where

$$\Delta k = k_0 \frac{\tilde{\chi}'(\omega)}{2n^2} \quad (4.42)$$

where  $\tilde{\chi}'(\omega)$  is the complex dielectric susceptibility of the material far from resonance which was introduced in Chapter 2. If the intrinsic gain exceeds the losses associated with the material, then the denominator in Eq. 4.40 can approach zero. This happens when

$$r_1 r_2 e^{-2i(k_0 + \Delta k)L} e^{2(\gamma - \alpha)L} = 1 \quad (4.43)$$

which implies  $E_t/E_i$  is infinite and a finite  $E_t$  can result from zero input field. That is to say oscillation has occurred.

Just taking the amplitude terms in Eq. 4.43 gives:

$$r_1 r_2 e^{2(\gamma-\alpha)L} = 1 \tag{4.44}$$

and

$$g_{net} = \gamma - \alpha = \frac{1}{2L} \ln \left( \frac{1}{r_1 r_2} \right) \tag{4.45}$$

where  $g_{net}$  is the net gain.

Using the values for the reflection coefficients for a doped polystyrene film and a cavity length of 1 cm it is possible to calculate the net gain at threshold to be  $3 \text{ cm}^{-1}$ . From Figure 4-14 it is possible to estimate the pump fluence which results in this gain to be  $37 \text{ } \mu\text{J}/\text{cm}^2$ .

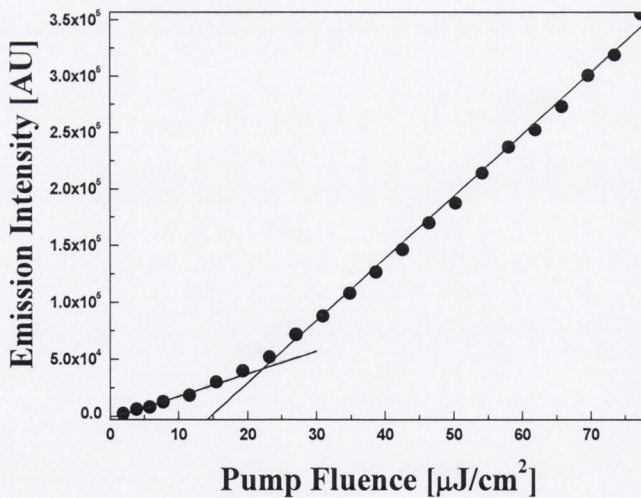


Figure 4-19 Input-output characteristics of B2080 doped polystyrene slab waveguide laser. Kink in the data at approximately  $23 \text{ } \mu\text{J}/\text{cm}^2$  indicates the onset of lasing.

The emission intensity from the film as function of pump fluence is shown in Figure 4-19. There is a clear kink in the data at about  $23 \text{ } \mu\text{J}/\text{cm}^2$  indicating the onset of

lasing. This transition into the lasing regime is accompanied by a dramatic narrowing of the spectrum. Figure 4-20 is a plot of spectral FWHM as a function of pump fluence showing this narrowing very clearly. The inset of this figure shows the spectrum above and below threshold. The spectral width above threshold is about 2.3 nm which is the expected width of a dye laser cavity without a wavelength selective element. In addition the lasing threshold predicted using the Fabry-Perot model is in good agreement with the measured threshold of  $23 \mu\text{J}/\text{cm}^2$ .

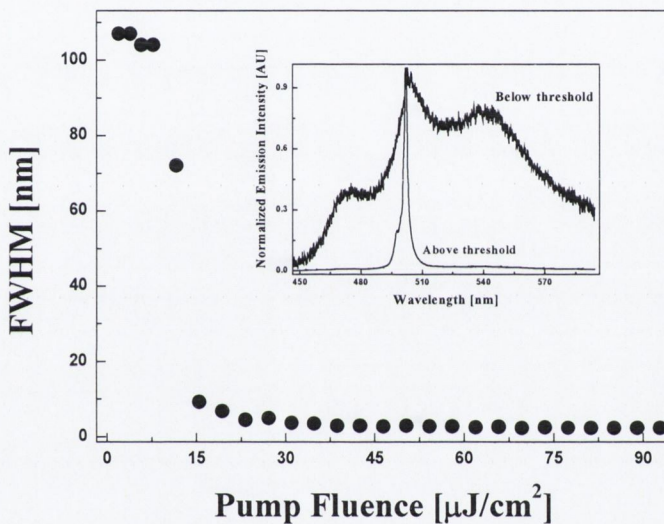


Figure 4-20 Evolution of spectral FWHM as a function of pump fluence for B2080 doped polystyrene slab waveguide laser. Inset: Emission spectrum above and below threshold.

## 4.8 Discussion

Amplification and lasing in the blue-green spectral region is an area of active research using both organic and inorganic materials. Tsutumi *et al.*<sup>15</sup> have measured the gain in B2080 doped polystyrene films with a dopant concentration of 10 wt % and a film thickness of  $4.5 \mu\text{m}$ . They measured a maximum gain of  $13.9 \text{ cm}^{-1}$  although they did not explicitly state the pump fluence used to achieve this gain. A summary of the results of some other research in this area is presented in Table 4-2. In addition to dye-doped polymer systems, neat films of conjugated

polymers and dendrimers have also exhibited large gain. One of the most extensively studied is PFO (poly(9,9-dioctylfluorene)). For example, Heliotis *et al.*<sup>16</sup> measured a net gain of  $74 \text{ cm}^{-1}$  in PFO at a fluence of  $750 \mu\text{J}/\text{cm}^2$  and Xia *et al.*<sup>17</sup> showed a gain of  $66 \text{ cm}^{-1}$  at the slightly lower fluence of  $670 \mu\text{J}/\text{cm}^2$  in a fluorene-based polymer. Lawrence *et al.*<sup>18</sup> measured a gain of  $79 \text{ cm}^{-1}$  in a neat dendrimer film although they used a higher fluence of  $3.0 \text{ mJ}/\text{cm}^2$ . Inorganic semiconductor lasers operating in the blue and UV spectral region rely mainly on GaN based material systems. Kim *et al.*<sup>19</sup> have measured the gain using the variable stripe length method of an epitaxially grown GaN based double heterostructure on a sapphire substrate and obtained a value of  $160 \text{ cm}^{-1}$  using a power density of  $200 \text{ KW}/\text{cm}^2$  which is lower than the power density used in this work. In comparison to these studies, B2080 doped polystyrene compares very well with other organic material systems.

Table 4-2 Summary of measurements of modal gain using variable stripe length method in UV to green spectral region.

	$\lambda$ (nm)	$\gamma_{\text{net}}$ ( $\text{cm}^{-1}$ )	$I_{\text{th}}$ ( $\text{MW}/\text{cm}^2$ )	$E_p$ ( $\text{mJ}/\text{cm}^2$ )	$\lambda_p(\text{nm})/\tau_p$ (ns)
<b>B2080</b> <sup>4</sup>	501	84	0.36	1.1	355/3
<b>PFO</b> <sup>16</sup>	466	74	1.5	0.75	390/0.5
<b>Dendrimer</b> <sup>18</sup>	425	79	6	3.0	337/0.5
<b>GaN</b> <sup>19</sup>	370	160	0.2	1.6	337/8

## 4.9 Summary

In summary, the variable stripe length method has been employed to measure an average net modal gain of  $84 \text{ cm}^{-1}$  at 501 nm at a pump fluence of  $1.1 \text{ mJ}/\text{cm}^2$  in doped polystyrene waveguides in the ns regime. The stimulated emission cross-section has been extracted and is in good agreement with the absorption cross-section of the material. The value of the gain obtained compares very well with

<sup>4</sup> Present study: 1,4-Bis[2-[4-[N,N-di(p-tolyl)amino]phenyl]vinyl]benzene.

other organic materials in the same spectral range. Low threshold lasing has also been achieved in a very basic slab waveguide laser under optical excitation.



## References

- <sup>1</sup> F.P. Schäfer, in *Topics in Applied Physics: Dye Lasers 2<sup>nd</sup> Ed*, Editor: F.P. Schäfer (Springer-Verlag, Berlin, Heidelberg, New York, 1977).
- <sup>2</sup> K.L. Shaklee, R.F. Leheny., *Appl. Phys. Lett.* **18**, 475 (1971).
- <sup>3</sup> M.A. Diaz-Garcia, S.F. De Avila, M.G. Kuzyk, *Appl. Phys. Lett.* **80**, 4486 (2002).
- <sup>4</sup> G. Mohs, T.Aoki, R. Shimano, M. Kuwata-Gonokami, S. Nakamura, *Solid State Communications* **108**, 105 (1998).
- <sup>5</sup> D. Marcuse, *Theory of Dielectric Optical Waveguides, 2<sup>nd</sup> Ed.*, (Academic Press, 1991).
- <sup>6</sup> A. Yariv, *Optical Electronics in Modern Communications 5<sup>th</sup> Ed.*, (Oxford University Press, Oxford, 1997).
- <sup>7</sup> M.J. Adams, *An Introduction to Optical Waveguides*, (Wiley, Chicester 1981).
- <sup>8</sup> L. D. Negro, P. Bettotti, M. Cazzanelli, D. Pacifici, L Pavesi, *Opt. Comm.* **229**, 337 (2004).
- <sup>9</sup> E. McKenna, J. Xue, A. Verdoni, M. Yetzbacher, R. Fan, A. Mickelson, *J. Opt. Soc. Am. B* **21**, 1294 (2004).
- <sup>10</sup> S. Sharafy, K.A. Muszkat, *J. Am. Chem. Soc.* **93**, 4119 (1971)
- <sup>11</sup> A. Galvan-Gonzalez, K.D. Belfield, G.I. Stegeman, M. Canva, S.R. Marder, K. Staub, G. Levina, R.J. Twieg, *J. Appl. Phys.* **94**, 756 (2003).
- <sup>12</sup> *Polymer Handbook*, (John Wiley & Sons,
- <sup>13</sup> M.D. McGehee, R Gupta, S. Veenstra, E.K. Miller, M.D. Garcia, A.J. Heeger, *Phys. Rev. B.* **58**, 7035 (1998).
- <sup>14</sup> E. Hecht, *Optics 3<sup>rd</sup> Ed.*, (Addison-Wiley, Harlow, 1998).
- <sup>15</sup> N. Tsutsumi, T. Kawahira, W. Sakai, *Appl. Phys. Lett.* **83**, 2533 (2003).
- <sup>16</sup> G. Heliotis, D.D.C. Bradley, G.A. Turnbull, I.F.W. Samuel, *Appl. Phys. Lett.* **81**, 415 (2002).
- <sup>17</sup> R. Xia, G. Heliotis, D.D.C. Bradley, *Appl. Phys. Lett.* **82**, 3599 (2003).
- <sup>18</sup> J.R. Lawrence, G.A. Turnbull, I.F.D. Samuel, G.J. Richards, P.L. Burn, *Opt. Lett.* **29**, 869 (2004).

---

<sup>19</sup> S.T. Kim, H. Amano, I. Akasaki, N. Koide, Appl. Phys. Lett. **64**, 1535 (1994).

# Chapter 5: Two-Photon Absorption Spectroscopy

## 5.1 Introduction

This chapter focuses on the nonlinear behaviour of stilbene dyes, with particular attention to their two-photon absorbing (TPA) properties. The measurements were carried out under fs excitation in solution and in solid thin films using z-scan and the two photon induced fluorescence (TPIF) method.

The chapter will begin with a review of the aspects of nonlinear optics theory most pertinent to the materials under investigation, specifically the third order susceptibility and effects associated with it. Next, a review of current research in the area of two-photon absorption is given with particular emphasis on current design strategies for efficient materials. Following this, a review of important experimental techniques in the area of TPA characterisation will be given. The remainder of the chapter will be taken up with the presentation and discussion of experimental results.

## 5.2 Nonlinear polarization

In chapter 2, the response of matter to an impinging electromagnetic wave was described in terms of the polarization  $\underline{P}$  of the material, which is a function of the input electric field  $\underline{E}$  and a complex, frequency dependent dielectric susceptibility  $\tilde{\chi}(\omega)$  according to Eq. 2.27:  $\tilde{\chi}(\omega) = Ne^2 / m_e \epsilon_0 \left[ \frac{1}{\omega_0^2 - \omega^2 + i\gamma\omega} \right]$ . This susceptibility arises due

to the harmonic oscillations associated with the classical electron oscillator, which gives rise to a polarization that is linearly dependent on the source wave.

This is an approximation, however, that only applies in the limit of low amplitude oscillations (elastic region) due to the relatively weak force of a low intensity wave. Under the influence of an intense laser beam, the electrons cannot follow the excitation in a linear fashion and the polarization can no longer be described by a linear function in  $\underline{E}$ . A more suitable and general description of the material response may be written as a power series expansion in the electric field strength:<sup>1</sup>

$$\underline{P}(t) = \tilde{\chi}^{(1)} \underline{E}(t) + \tilde{\chi}^{(2)} \underline{E}^2(t) + \tilde{\chi}^{(3)} \underline{E}^3(t) + \dots \quad (5.1)$$

The quantities  $\chi^{(n)}$  are the  $n^{\text{th}}$  order susceptibilities and since  $\underline{E}$  and  $\underline{P}$  are vectors, are tensors of rank  $n+1$  for  $n > 1$ . During the course of the following discussion, the tensor properties of  $\chi^{(n)}$  will be dropped for clarity and the tilde notation will also be discarded as the analysis will deal exclusively with the real part of the susceptibility unless otherwise stated.

The symmetry relationship  $\underline{P}(\underline{E}) = \underline{P}(-\underline{E})$  means that even order susceptibilities do not feature in materials with centrosymmetry. Since the materials under study in this thesis are isotropic, the first nonlinear contribution to their polarization takes place via  $\chi^{(3)}$ .

In the limit of the classical electron oscillator model, the nonlinear response can be understood by including higher order correction terms in the restoring force experienced by the electron. For a centrosymmetric material, the restoring force is given, not by Eq. 2.10:  $F(t) = -Kx(t)$ , but rather by

$$F_{rest} = -m\omega_0^2 x + mbx^3 \quad (5.2)$$

where  $b$  represents the strength of the nonlinear contribution. In this case, the potential energy curve is no longer a parabola as is the case in the elastic limit, but has the shape shown in Figure 5-1. The function is symmetric as it should be for a centrosymmetric material.

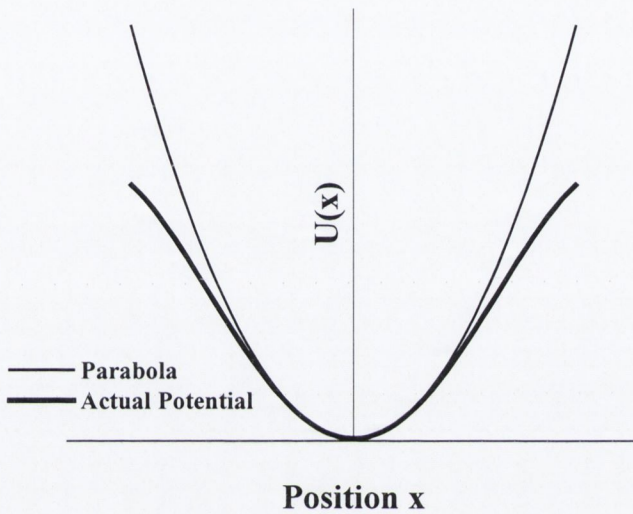


Figure 5-1 Potential energy curve for harmonic and anharmonic oscillator in a centrosymmetric material.

As an example of the new types of phenomena that become apparent due to the third order susceptibility, take the simple case of an electric field with time dependence of the form:

$$E = E_0 \cos(\omega t) \quad (5.3)$$

The third order polarization is given by:

$$P^{(3)}(t) = \chi^{(3)} E(t)^3 \quad (5.4)$$

Since

$$\cos^3(\omega t) = \frac{1}{4} \cos(3\omega t) + \frac{3}{4} \cos(\omega t) \quad (5.5)$$

the nonlinear polarization becomes:

$$P^{(3)}(t) = \frac{1}{4} \chi^{(3)} E_0^3 \cos(3\omega t) + \frac{3}{4} \chi^{(3)} E_0^3 \cos(\omega t) \quad (5.6)$$

In this specific case, it can be seen that the polarization can be composed of two parts. The first term on the RHS of Eq. 5.6 shows a response at 3 times the fundamental frequency. An electromagnetic wave with frequency  $\omega$  of sufficient intensity can cause a polarization that oscillates at  $3\omega$  in a process called third harmonic generation. From the point of view of conservation of energy, to generate a photon of energy  $3\hbar\omega$ , it is necessary to take the energy of three of the fundamental photons and convert them to one photon at the 3<sup>rd</sup> harmonic frequency. Thus, this third order process involves the mixing of 4 photons where the 4<sup>th</sup> is the sum of the other three. The 3<sup>rd</sup> order susceptibility in this process can then be written as  $\chi^{(3)}(\omega_4; \omega_1, \omega_2, \omega_3)$ .

The second term in Eq. 5.6 gives a nonlinear contribution to the polarization at the fundamental frequency and is responsible for the nonlinear refractive index. The refractive index may be written in terms of the linear value and a term that depends on the electric field strength.

$$n = n_0 + \bar{n}_2 \langle \underline{E}^2 \rangle \quad (5.7)$$

where  $\bar{n}_2$  is the nonlinear contribution to the refractive index and the angular brackets denote a time average of the electric field.

Defining the general form of the electric field as

$$E(t) = E(\omega) e^{-i\omega t} + c.c. \quad (5.8)$$

where *c.c.* denotes the complex conjugate, the refractive index can be written

$$n = n_0 + 2\bar{n}_2 |E(\omega)|^2 \quad (5.9)$$

and the third order nonlinear polarization becomes

$$P^{(3)} = 3\chi^{(3)}(\omega_4 : \omega_1 + \omega_2 - \omega_3) |E(\omega)|^2 E(\omega) \quad (5.10)$$

giving a total polarization of

$$P_{total} = \chi^{(1)}E(\omega) + 3\chi^{(3)} |E(\omega)|^2 E(\omega) \quad (5.11)$$

It is now possible to define an effective susceptibility that depends not only on the material but also on the electric field strength of the incident light:

$$\chi_{eff} = \chi^{(1)} + 3\chi^{(3)} |E(\omega)|^2 = n^2 - 1 \quad (5.12)$$

combining Eqs. 5.9, 5.11 and 5.12, the linear and nonlinear refractive indices can be related to the linear and nonlinear susceptibilities by

$$n_0^2 = 1 + \chi^{(1)} \quad (5.13)$$

$$\bar{n}_2 = \frac{3\chi^{(3)}}{4n_0} \quad (5.14)$$

In many experimental cases it is more convenient to measure the optical intensity of the incident light as opposed to its electric field strength. The refractive index may then be written:

$$n = n_0 + n_2 I = n_0 + \Delta n \quad (5.15)$$

where the intensity is defined as

$$I = 2\varepsilon_0 n_0 c |E|^2 \quad (5.16)$$

Since both definitions of the refractive index must be consistent, it is possible to write the nonlinear refractive index as:

$$\bar{n}_2 = \frac{\bar{n}_2}{n_0 c} \quad (5.17)$$

and hence the 3<sup>rd</sup> order susceptibility may now be written in terms of the intensity dependent refractive index as:

$$n_2 = \frac{3\chi^{(3)}}{4\epsilon_0 n_0^2 c} \quad (5.18)$$

The effect of the dependence of the refractive index on the intensity of the incident light is called the optical Kerr effect. In a laser beam with a non-uniform intensity profile, this effect is responsible for the phenomenon of self-focussing (or defocussing). For example, in a material with positive nonlinearity, the centre of a gaussian beam will experience a higher refractive index, which results in the material behaving as a positive lens. This process is of great importance in many aspects of nonlinear optics and laser physics. It is self-focussing that is responsible for the characteristic trace seen in a closed-aperture z-scan. In titanium sapphire mode-locked oscillators, self-focussing in the crystal along with a variable aperture allows the intense mode-locked pulses to pass through the cavity while the background CW radiation is blocked, thus providing a method of self-regulating passive mode-locking.

The foregoing discussion has focussed on processes whereby the initial and final quantum states of the system are identical. This is shown schematically in Figure 5-2.

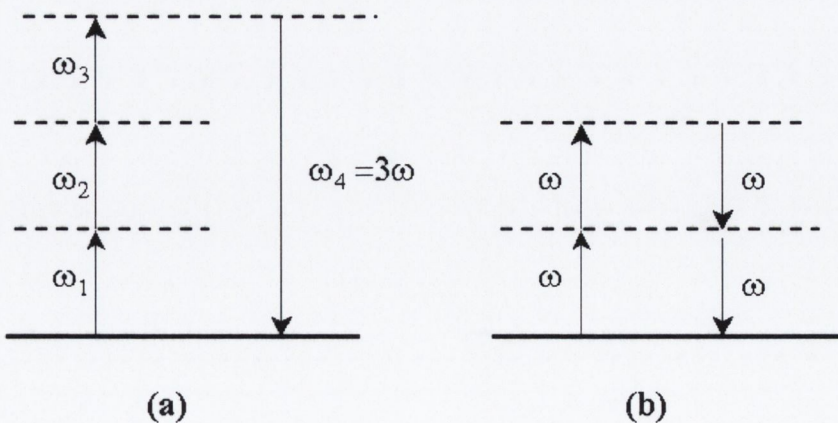


Figure 5-2 Parametric processes (a) third harmonic generation and (b) the optical kerr effect. Dashed lines denote virtual levels.



The dash lines in Figure 5-2 denote virtual levels in which the population may only reside for a length of time allowed by the uncertainty principle. There are some processes, however, that also depend nonlinearly on the intensity of the light but which result in a rearrangement of the population between real levels in the system. These processes are referred to as non-parametric process. One of these processes is two-photon absorption depicted in Figure 5-3 whereby two photons of the same frequency are excited to an upper excited state via a virtual level.

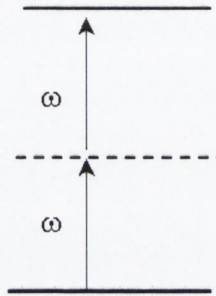


Figure 5-3 Two photon absorption via virtual level.

Unlike parametric processes, two-photon absorption results in the net absorption of the incident radiation and must be described by the imaginary part of the susceptibility:

$$\tilde{\chi}^{(3)} = \chi_{real}^{(3)} + i\chi_{imag}^{(3)} \quad (5.19)$$

This implies a change in the absorption coefficient  $\alpha$ , of the material, which depends on the intensity of the incident light. This change may be written by defining a two-photon absorption (TPA) coefficient,  $\beta$ :

$$\alpha(I) = \alpha_0 + \beta I \quad (5.20)$$

Where  $\alpha_0$  is the linear absorption coefficient and  $I$  is the intensity as defined above. The imaginary part of  $\chi^{(3)}$  can be written in terms of  $\beta$  as:

$$\chi_{imag}^{(3)} = \frac{n_0^2 \epsilon_0 c^2}{\omega} \beta \quad (5.21)$$

## 5.3 Two-photon absorption

### 5.3.1 Introduction

Multiphoton transitions involving the simultaneous absorption of more than one photon in a single quantum event were first predicted by Maria Göppert-Mayer<sup>2</sup> in 1931 and were subsequently demonstrated in the laboratory in 1961 by Kaiser and Garret<sup>3</sup> for transitions in  $\text{CaF}_2:\text{Eu}^{2+}$  with a ruby laser excitation at 694 nm. Since that time, there has been extensive research carried out into two-photon absorption from a fundamental point of view and also in applied research where this process can find many applications. Organic materials with a high degree of  $\pi$ -conjugation exhibit a large third order nonlinear response,<sup>4</sup> and much of the research in this area has been carried out on organic materials such as dyes and conjugated polymers.

### 5.3.2 Upconversion

The process by which the two-photon absorption transition is followed by a radiative decay is called upconversion. This process of converting long wavelength radiation to shorter wavelength is a very useful and much investigated phenomenon. For example, two-photon excited emission has been used to generate coherent radiation. The first two-photon pumped stimulated emission was reported by Patel *et al.* who demonstrated 6.5  $\mu\text{m}$  radiation from PbTe crystals that were pumped at 10.6  $\mu\text{m}$ .<sup>5</sup> More recently two-photon pumped stimulated emission and lasing has been shown in a variety of gain media. These include semiconductor crystals<sup>6</sup> and organic dyes both in solution and in solid-matrices.<sup>7,8,9,10</sup> In addition to being used to generate coherent radiation, two-photon pumped emission has found application in the area of two-photon fluorescence microscopy.<sup>11</sup> This technique involves the staining of the sample under investigation with a fluorescent dye, which is excited with a laser beam, in this case, a beam in the red or infrared. Since two-photon absorption is a third order process, the up-converted fluorescence is proportional to the square of the light intensity and thus the emission is confined to the focal plane providing very precise excitation. For the same reason, this allows for 3-dimensional imaging. Since its inception in 1990, two-photon microscopy has gained wide acceptance in the scientific community especially in the study of biological specimens.

### 5.3.3 Optical Limiting

Optical limiting is the term designated to the process by which high intensity light is absorbed by a sample while allowing the transmission of low-level background light. The applications of this process are immediately obvious in the area of the protection of light sensitive detectors, not least the human eye. A suitable optical limiting material will have high linear transmission (>70%) at low intensity light levels and display rapid, high extinction light-clamping behaviour at high intensity. Of the various mechanism that may be used to achieve this such as nonlinear scattering, reverse-saturable absorption<sup>12</sup> and TPA,<sup>13</sup> the latter two processes have received most attention, since both of these processes are controlled by the molecular structure and are hence accessible to molecular engineering. Of the two, TPA is suitable for controlling optical intensity of short (ps) pulses whereas reverse-saturable absorption is more suitable for longer (ns) pulses.

### 5.3.4 Two-photon spectroscopy and photochemistry

The selection rules for the absorption of two photons of incident radiation are different to those governing the absorption of one photon and different final states are reached in cases where the molecule displays a high degree of symmetry. This makes two-photon spectroscopy a useful tool for probing states that are inaccessible with one-photon absorption, providing further information on the basic structure-property relationships and photophysics of molecules.<sup>14</sup>

Furthermore, molecules in the excited state can, under certain circumstances undergo chemical changes. The site selective abilities of two-photon excitation make it a very useful tool for inducing these photochemical changes at highly localized positions. For example, materials have been developed that produce acid upon absorbing two photons which can be used in microchannel fabrication.<sup>15</sup>

## 5.4 Design strategies for two-photon absorbing materials

### 5.4.1 Introduction

Since the realization that two-photon absorbing materials could have useful applications in the areas mentioned above, much research has been carried out into

understanding the factors effecting the strength and position of the transition in a given material and several design strategies have been suggested and implemented.

Initial studies in this area focussed on characterizing molecules already known to possess reasonably high TPA cross-sections such as rhodamine B, rhodamine 6G and fluorescein.<sup>16,17</sup> During these early investigations, much of the research was directed towards experimental techniques suitable for the accurate measurement of the TPA cross section.

Since then, a more concerted effort has been undertaken to understand the photophysics involved in TPA and much focus has been placed on linear conjugated small molecules with well-defined donor and acceptor moieties. A schematic representation of such molecules are depicted schematically in Figure 5-4 which shows the motif of dipolar, quadrupolar and octupolar molecules. Much of the research has focussed on explaining and engineering the effect of symmetry, conjugation length and the strength of the effect of donor/acceptor groups.

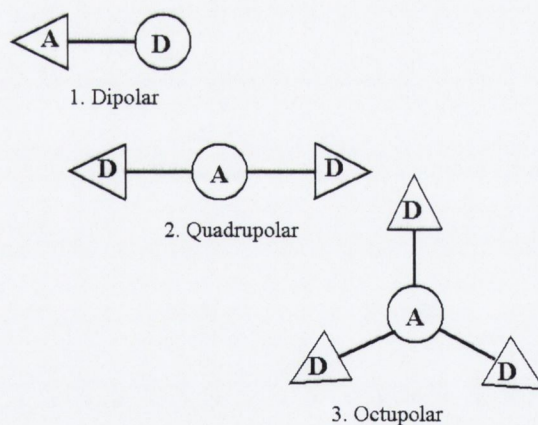


Figure 5-4 Schematic diagram of dipolar, quadrupolar and octupolar molecules. A: Acceptor, D: Donor.

#### 5.4.2 Quadrupolar molecules

The pioneering work by Albota *et al.*<sup>18</sup> describes a means to systematically investigate the effect of factors such as conjugation length, and electron donating and accepting substituents on the strength of the two-photon transition in a set of homologous molecules. Their study was based on symmetric molecules with

Donor- $\pi$ -bridge-Donor and Acceptor- $\pi$ -bridge-Acceptor motifs where the  $\pi$ -bridge was a series of phenylene-vinylene linkages. Since the molecules have a high degree of symmetry, the TPA transition was expected to take place between the ground state and the second excited singlet state  $S_2$  which is the lowest two-photon allowed transition.

The TPA cross-section was found to be proportional to the transition dipole strengths for the  $S_0 \rightarrow S_1$ , and  $S_1 \rightarrow S_2$  transitions. It was also noted that the addition of amine-based electron donating substituents to the ends of the molecule had a two-fold effect:

1. It caused an increase in the  $S_0 \rightarrow S_1$  transition dipole.
2. A large redistribution of the  $\pi$ -electrons upon excitation due to intramolecular charge transfer (ICT) took place. Specifically, a symmetrical charge transfer from the ends of the molecule to the centre (in the case of electron donating substituents) and hence an increase in the quadrupole moment, which leads to an increased delocalisation of the  $\pi$ -electron cloud upon excitation, increasing the  $S_1 \rightarrow S_2$  transition dipole strength. The strategies employed to investigate this ICT effect were as follows:
  - I. Increase in conjugation length, which increases the distance associated with the charge transfer, increasing the quadrupole moment.
  - II. Increase in the acceptor strength of the  $\pi$ -bridge by addition of suitable side groups which would increase the amount of charge transfer.
  - III. Sense of the charge transfer reversed to provide a Acceptor- $\pi$ -bridge-Acceptor structure.

These strategies were successful in increasing the TPA cross-section in the molecules studied with the Donor- $\pi$ -bridge-Donor motif being the most successful.

The molecules under investigation in this study are very similar to the quadrupolar molecules studied by Albota *et al.* and also He *et al.*<sup>19</sup> and the values obtained for the TPA cross-section are in good agreement with those published.

### 5.4.3 Dipolar “push-pull” molecules.

Another strategy employed in the design of efficient TPA materials is the “push-pull” motif where there is an asymmetric positioning of the donor and acceptor groups about the central conjugated bridge. Such molecules have a net dipole and since they are not symmetrical, two-photon excitation takes these molecules into the same excited state as one-photon excitation in many cases.

Lin *et al.*<sup>20</sup> have used the stilbenoid unit as the conjugated backbone of their molecules and have examined the effect of donor and acceptor substituents placed asymmetrically at each end. They found that stronger acceptors produce more efficient ICT and hence larger TPA cross-section although the molecules in this study did not achieve the larger molecular TPA cross-section achieved in the case of symmetric doping. Antonov *et al.*<sup>21</sup> have investigated the effect of changing the nature of the  $\pi$ -electronic bridge by insertion of nitrogen on the TPA abilities of some push-pull molecule but found that this had little effect. Both of these studies were consistent in their finding that the strength of the acceptor group is the most sensitive parameter in the molecular design of push-pull molecules. Reinhardt *et al.* underlined the significance of planarity in D- $\pi$ -A stilbenoid molecules.<sup>22</sup> Recently Beverina *et al.*<sup>23</sup> provided the first demonstration of efficient two-photon absorption at telecommunications wavelengths in a dipolar chromophore extending the available TPA spectrum considerably to longer wavelengths.

### 5.4.4 Recent advances in the design of octupolar and branching molecules for multiphoton absorption.

A considerable amount of theoretical work has gone into understanding the precise nature of the transition when a molecule absorbs two photons. Kuzyk<sup>24</sup> has used a sum-over-states quantum perturbation analysis to calculate the maximum *theoretical* limit of the two-photon absorption cross-section. One of the main results of that work was the fact that molecules with more  $\pi$ -electrons have a larger two-photon absorption cross-section and additionally, it is essential that the electron path remain conjugated if the cross-section is to be large. One approach to this is to consider branching or dendrimer structures which are basically very large conjugated molecules which possess an octupolar moment. In these materials ICT

takes place upon excitation either from electron donating peripheral groups to a core with strong acceptor character or vice versa. In the past number of years there has been a considerable surge in interest in these molecules and reasonably large TPA cross-sections have been reported in addition to high photoluminescence quantum yield which is essential for upconversion applications.<sup>25,26</sup>

## 5.5 Experimental Techniques-A Review

### 5.5.1 Introduction

There are several techniques for measuring the degenerate TPA (the absorption of two photons of the same energy) spectrum of a sample. The most common of these can be roughly divided into two categories:

- Nonlinear transmission methods
- Two-photon induced fluorescence (TPIF)

It should also be noted that neither direct nonlinear transmission methods nor the TPIF method give information about the dynamics of the absorption and/or subsequent relaxation. In order to understand the dynamic behaviour of a nonlinear system, it is necessary to use time resolved methods such as four-wave-mixing or pump-probe spectroscopy.

### 5.5.2 Nonlinear Transmission Methods

Nonlinear transmission methods have been used more widely in the past than methods based on photoluminescence since they do not rely on the secondary process of fluorescent emission to measure the strength of the nonlinearity, but rather measure the intensity dependent absorption directly. There are problems associated with the interpretation of the data from such an experiment however, since it is not always immediately obvious what process is causing the effect. For example high order effects can make the measured TPA cross-section appear higher than it is especially in the ns regime, and also thermal effects can cause spurious results when using lasers with high rep rates.<sup>27</sup>

## Direct Nonlinear Transmission

This method involves the direct measurement of the absorption of a laser beam as a function of input intensity by externally varying the intensity of the beam with filters or some other similar method. The advantage of this method is that it is readily applicable to samples that are not optically thin such as waveguides and fibers. Normally this measurement is carried out at a single wavelength<sup>28</sup> with a pulsed laser source.

Lin *et al.*<sup>20</sup> have developed a variation on this method by using a white light supercontinuum as the source. By comparing the transmission of the continuum through a pure solvent and that obtained with the solution to be measured, they have been able to extract the TPA spectrum in one measurement. In order to ensure degenerate TPA, the wavelength components of the continuum are spatially separated using a prism prior to being focussed into the sample. This is an extremely useful method since normally extracting the spectrum of values requires multiple measurements at closely spaced wavelengths across the region of interest whereas this method allows the measurement of the complete spectrum in one step.

## Z-Scan

Sheikh-Bahae<sup>29</sup> and co-workers developed the z-scan method in 1990 and since then it has become one of the most widely accepted experimental methods in nonlinear optics. It is similar to direct transmission methods in that the transmission of the sample is measured as a function of beam intensity, however in this case, the variation in input intensity is achieved by translating the sample through the focus of a lens.

Recently it has been shown that it may be possible to carry out the z-scan measurement with a white-light continuum to obtain the TPA spectrum in one measurement. While this method has not been used to measure the TPA spectrum of any organic materials, initial results indicate the method is at least feasible and should provide a very useful tool for future work.<sup>30</sup>



### 5.5.3 Two-photon induced fluorescence methods

In the case of molecules exhibiting sufficiently strong upconverted fluorescence, it is possible to use the two-photon induced fluorescence method. It involves comparing the two-photon pumped fluorescence to the emission from a reference sample<sup>31</sup> or to the emission from the same sample under one photon pumping where the linear absorption coefficient is known.<sup>32</sup> The second method has been applied to solid thin film samples.<sup>33</sup> Since this is a background free method, it has gained a large degree of acceptance in the scientific community in more recent years.

In this study, both the z-scan and two-photon pumped PL methods have been applied.

## 5.6 Z-scan Technique

### 5.6.1 Introduction

Since its development by Sheik-Bahae<sup>29</sup> *et al.* in 1990, the z-scan technique has gained rapid acceptance as the standard method for simultaneously obtaining information on the real *and* imaginary parts of the nonlinearity of a sample. This is due to its experimental simplicity, and straightforward analysis.

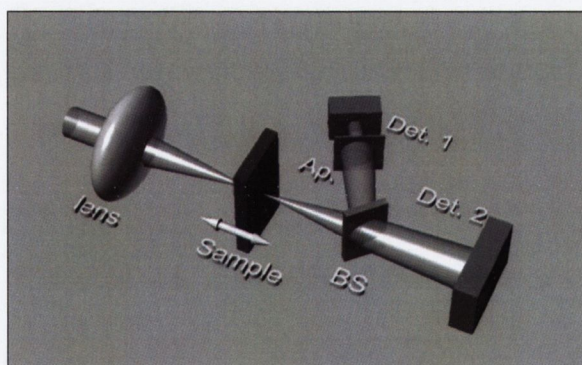


*Figure 5-5 Schematic open and closed aperture z-scan experiment. The beam is split after the sample allowing simultaneous recording of open and closed aperture trace. Det: photodetector, BS: beamsplitter*

To understand the way in which the experimental procedure works, consider the experimental set-up shown in Figure 5-5. The sample is placed in the path of a focussed laser beam as shown and as it is translated through the focus of the lens,

the transmission is recorded as a function of position, which is equivalent to measuring the transmission as a function of beam intensity. There are two types of z-scan traces, called closed-scan measured at the detector marked Det. 1 which is in the far-field of the beam and the open scan, measured at the detector marked Det. 2.

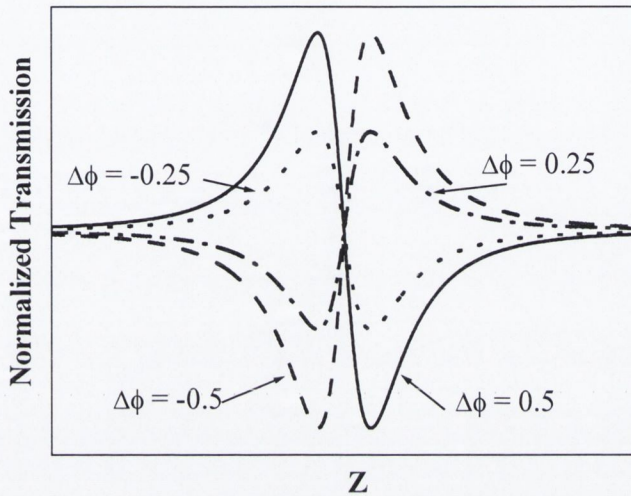


*Figure 5-6 Theoretical closed-aperture z-scans for a gaussian beam profile calculated with the use of Eq. 5.33.  $\Delta\phi$  is the nonlinear phase shift which gives the strength of the nonlinearity and will be defined below.*

Considering first the signal detected at Det. 1 and a sample with positive nonlinearity: When the sample is far from the focus, the intensity is low and the transmission is measured in the linear regime at Det. 1. As the sample is moved towards the focus from left to right as shown, the intensity will increase to a point where nonlinear changes in the refractive index will cause the onset of self-focussing. If the sample is thin, it can now be considered as a thin positive lens, which will cause the far field beam to expand resulting in a drop in transmission at the aperture. As the sample moves through the focus and beyond, the positive lensing action will tend to collimate the beam resulting in an increase in transmission at the aperture until finally, the sample moves far from focus and returns to the flat linear transmission regime. This process results in a characteristic z-scan trace. Figure 5-6 shows theoretical closed aperture z-scans calculated for a laser beam with Gaussian intensity profile.

Now consider the case where there is no aperture at the detector as in the case of Det. 2. Under these circumstances, the detector is insensitive to changes in the beam profile provided all the light from the transmitted beam is collected. This detector is sensitive to changes in the intensity of the transmitted light and as such can measure nonlinear absorption effects. The signal measured at Det.2 is called an open aperture scan and for two-photon absorption it has a characteristic shape as shown in Figure 5-7.

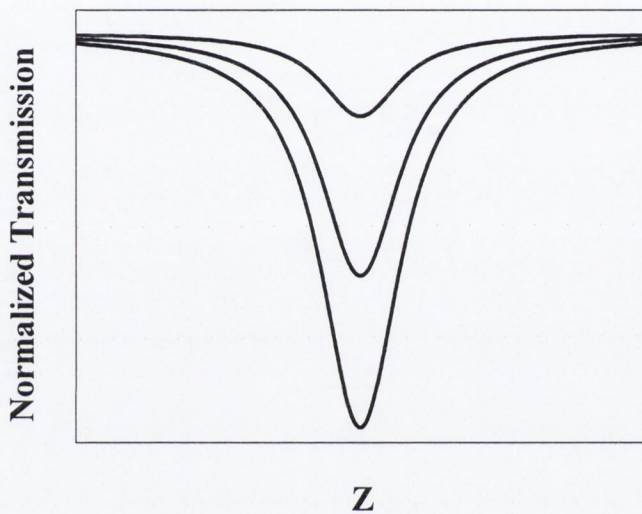


*Figure 5-7 Theoretical open-aperture z-scans for a gaussian beam profile calculated from Eq. 5.36.*

In the case where nonlinear refraction is accompanied by nonlinear absorption, the closed aperture scan becomes distorted with the absorption having the effect of deepening the valley and lowering the peak. A simple method of dividing the closed scan by the open gives a curve that closely approximates that which would be achieved if the sample had the same real nonlinearity but with no nonlinear absorption.<sup>34</sup>

### 5.6.2 Z-scan theory

In order to carry out a quantitative analysis of the curves generated in z-scan experiments, a mathematical description of the effect of nonlinear refraction and absorption on the propagation of a Gaussian beam in the slow-varying envelope

approximation is necessary. This theory has been extensively dealt with in the literature<sup>29,34</sup> and as such a full treatment of the derivation will not be given here as this would only serve to repeat an already well established procedure. The main details, however will be presented.

A Gaussian beam of waist radius  $w$  propagating in the  $+z$  direction may be written as

$$\underline{E}(z, r, t) = \underline{E}_0(t) \frac{w_0}{w(z)} \exp \left[ -\frac{r^2}{\omega^2(z)} - \frac{ikr^2}{2R(z)} - i\phi(z, t) \right] \quad (5.22)$$

where  $\underline{E}_0(t)$  is the electric field at the focus and contains the temporal envelop of the electric field.  $\omega_0$  is the waist radius at the focus,  $w(z)$  is the beam waist radius which changes as a function of  $z$  according to

$$w(z) = w_0 \left( 1 + \frac{z^2}{z_0^2} \right)^{\frac{1}{2}} \quad (5.23)$$

where  $z_0 = \frac{kw_0^2}{2}$  is the diffraction length of the beam and  $k = \frac{2\pi}{\lambda}$ ,  $\lambda$  being the wavelength.  $R(z)$  is the radius of curvature of the wavefront and is defined as:

$$R(z) = z \left( 1 + \frac{z_0^2}{z^2} \right) \quad (5.24)$$

The term  $\phi(z, t)$  is the radially invariant phase term and since only radially varying phase terms are of concern, the slow varying envelop approximation applies and all phase changes that are uniform in  $r$  are ignored.

In the following derivation, the assumption of a "thin" sample is used; that is a sample in which the local phase variations do not change the beam profile within the sample. The criterion for this is  $L \ll z_0 / \Delta\phi(0)$ , where  $L$  is the sample thickness. This criterion is automatically met under most circumstances since  $\Delta\phi$  is small. In addition, it has been found that this criterion is more restrictive than it need be and it is sufficient if  $L < z_0 / \Delta\phi(0)$ .<sup>34</sup>

The assumption of a thin sample simplifies the situation and under these circumstances, the amplitude which is proportional to  $\sqrt{I}$  and phase  $\phi$  of the electric field are now governed by the simple set of simultaneous equations.

$$\frac{d\phi}{dz'} = \Delta n(I)k \quad (5.25)$$

and

$$\frac{dI}{dz'} = -\alpha(I)I \quad (5.26)$$

where  $z'$  is the propagation depth in the sample.

In the case of cubic nonlinearity and negligible nonlinear absorption, these two equations may be simultaneously solved to give the phase shift  $\Delta\phi$  at the exit surface of the sample:

$$\Delta\phi(z, r, t) = \Delta\phi_0(z, t) \exp\left[-\frac{2r^2}{w^2(z)}\right] \quad (5.27)$$

with

$$\Delta\phi_0(z, t) = \frac{\Delta\Phi_0(t)}{1 + z^2/z_0^2} \quad (5.28)$$

where  $\Delta\Phi_0$  is the on axis phase-shift at the focus and is defined as

$$\Delta\Phi_0 = k\Delta n_0(t)L_{eff} \quad (5.29)$$

where  $L_{eff} = (1 - e^{-\alpha L})/\alpha$  is called the effective length of the sample where  $\alpha$  is the linear absorption coefficient.  $\Delta n_0$  is the intensity dependent change in refractive index at the focus given by  $\Delta n_0 = n_2 I_0$ , where  $I_0$  is the irradiance at the focus within the sample.

The complex electric field exiting the sample  $E_e$  containing the nonlinear phase shift can now be written:

$$\underline{E}_e(z, r, t) = \underline{E}(z, r, t) e^{-\frac{\alpha L}{2}} e^{i\Delta\phi(z, r, t)} \quad (5.30)$$

The method by which this exiting beam is propagated to the aperture is detailed in references 29 and 34. The method is called Gaussian decomposition<sup>35</sup> where the field  $\underline{E}_e$  is decomposed in to a summation of Gaussian beams through a Taylor series expansion in the nonlinear phase shift. Each of these Gaussians can then be propagated to the aperture plane where the beam is reconstructed. The transmitted power through the aperture is then obtained by integrating this aperture field over the area of the aperture. Including the pulse temporal variation, the normalized Z-scan transmittance can then be calculated to be

$$T(z) = \frac{\int_{-\infty}^{\infty} P_T(\Delta\Phi_0(t)) dt}{S \int_{-\infty}^{\infty} P_i(t) dt} \quad (5.31)$$

where  $P_i(t) = \pi w_0^2 I_0(t)/2$  is the instantaneous input power in the sample and  $\hat{S} = 1 - \exp\left[-2r_a^2/\omega_a^2\right]$  is the aperture linear transmittance where  $w_a$  is the beam waist at the aperture in the linear regime. Assuming the far-field condition and via other simplifications detailed in references 29 and 34, it turns out that the transmission can be geometry independent and is given by

$$T(z, \Delta\Phi_0) \approx 1 - \frac{4\Delta\phi_0 z/z_0}{(z^2/z_0^2 + 9)(z^2/z_0^2 + 1)} \quad (5.32)$$

This equation applies to nonlinear phase changes in the absence of nonlinear absorption.

As outlined in section 5.2 the intensity dependent absorption coefficient is given by Eq. 5.20. This yields an irradiance distribution and phase shift at the exit surface of the sample of:

$$\underline{I}_e(z, r, t) = \frac{\underline{I}(z, r, t) e^{-\alpha_0 L}}{1 + q(z, r, t)} \quad (5.33)$$

where  $q(z, r, t) = \beta \underline{I}(z, r, t) L_{eff}$  and

$$\Delta\phi = \frac{kn_2}{\beta} \ln[1 + q(z, r, t)] \quad (5.34)$$

Following a procedure similar to that used to obtain Eq. 5.32, the sample transmission as measured at the open aperture detector is given by:

$$T(z) = \exp(-\alpha_0 L) \frac{\ln[1 + q_0(z)]}{q_0(z)} \quad (5.35)$$

where  $q_0(z) = \beta I_0 L_{eff}$  where  $I_0$  is the peak, on-axis intensity.

Van Stryland<sup>34</sup> *et al*, have further simplified this for a Gaussian beam, under the approximation  $\beta I_0 L_{eff} \ll 1$  and for instantaneous response times with respect to the pulse width, the normalized change in transmittance is:

$$\Delta T(z) \approx -\frac{q_0}{2\sqrt{2}} \frac{1}{[1 + z^2/z_0^2]} \quad (5.36)$$

For  $z = z_0$ , the change in transmittance is maximum and  $q_0$  and hence  $\beta$  can be deduced immediately from the scan.

### 5.6.3 Experimental Procedure

The Z-scan experiments carried out in this study were performed in the femtosecond regime at 800 nm using 100 fs pulses from an amplified titanium sapphire laser system. A 76 MHz train of  $\sim 100$  fs pulses was generated using a Coherent MIRA 900-P oscillator. A Pockels cell extracted pulses which were first decompressed to  $\sim 100$  ps using a double-grating decompressor and subsequently amplified in a regenerative amplifier pumped at 30 Hz with the second harmonic of a nanosecond Nd:YAG. Subsequent recompression was achieved with a double-grating compressor to produce  $\sim 100$  fs, transform-limited pulses. Sampling was achieved using photodiodes and boxcar sampling was applied to the data collection.

Prior to each run the peak on-axis intensity at the focus of the lens was deduced in a comparative way from the closed aperture scan of a 1 mm silica slide. The non-linear phase shift is given by

$$\Delta\phi = \frac{2\pi n_2 I L_{eff}}{\lambda} \quad (5.37)$$

Where  $n_2$  is the non-linear refractive index,  $I$  is peak on-axis intensity,  $L_{eff}$  is the effective sample thickness taking into account the linear absorption at the wavelength  $\lambda$ . The non-linear refractive index of silica was assumed to be  $3 \times 10^{-16} \text{ cm}^2/\text{GW}$ .<sup>36</sup> By running a closed aperture scan on silica, the resulting intensities were deduced to be of the order of  $70 \text{ GW/cm}^2$ .

The z-scans were carried out on chloroform solutions up to a concentration of  $\sim 0.75 \text{ wt } \%$  in a 1 mm quartz cuvette. The exact concentration was deduced from the absorbance of the solution prior to each scan to avoid any errors due to evaporation of solvent. This measurement also confirmed no degradation of the sample occurred during the experiments.

#### 5.6.4 Experimental Results

The closed aperture scans for concentrations up to  $0.755 \text{ wt } \%$  SP35 in chloroform are shown in Figure 5-8 along with the curves calculated according to Eq. 5.32.

The peak-to-valley difference in the closed aperture scan is related to the real part of the non-linear phase shift. However, as outlined above, in the presence of two-photon absorption, there is a distortion of the closed-aperture trace since the two-photon absorption tends to lower the peak of the trace and deepen the valley. The procedure of dividing the closed scan by the open, has been applied to the data presented in Figure 5-8. The peak-to-valley height of the traces decreases with increasing concentration indicating that the real part of the non-linearity of SP35 has the opposite sign to that of chloroform at 800 nm.

In order to extract an accurate value for the nonlinear refractive index from the z-scan traces, concentration dependencies of the nonlinear phase shift can be used.<sup>36</sup> Measured z-scans on solutions contain information about both the solvent and



solute. In addition, the solution is contained within a glass cuvette. Effectively the scan measures contributions from the solvent, solute and the walls of the cuvette. This fact can contribute to poor fitting in the wing regions of the scans.

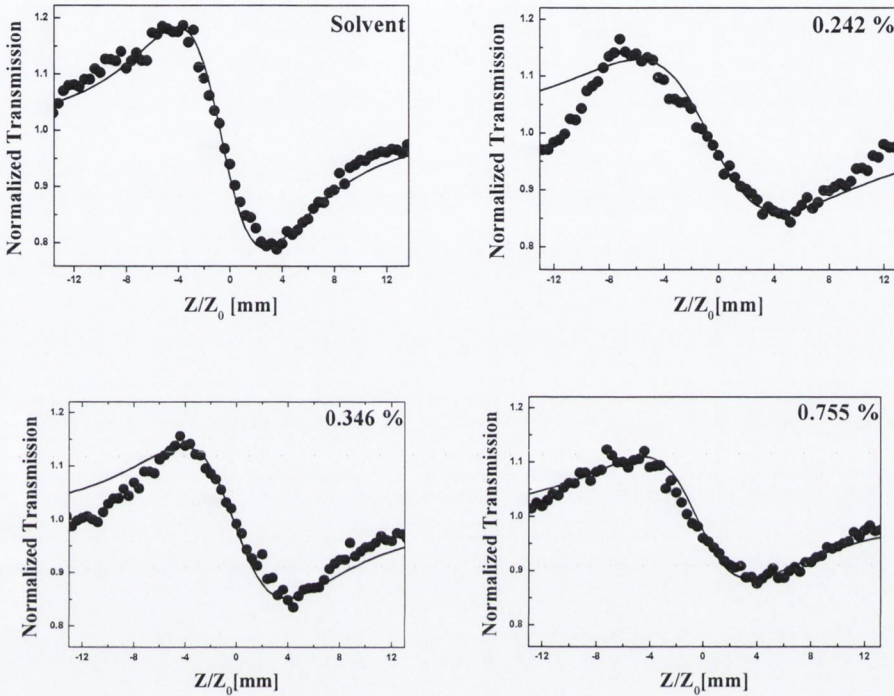


Figure 5-8 Closed aperture scans for SP35 in chloroform solutions up to 0.755 wt. Peak-to-valley difference decreases with increasing concentration indicating that the nonlinearity of SP35 has the opposite sign to that of chloroform at this wavelength. Solid lines are theoretically calculated according to Eq. 5.32:

$$T(z, \Delta\Phi_0) \approx 1 - \frac{4\Delta\phi_0 z/z_0}{(z^2/z_0^2 + 9)(z^2/z_0^2 + 1)}$$

For a dilute solution the complex refractive index can be approximated by

$$n_2 = mn_{2,dye} + (1-m)n_{2,solvent} \quad (5.38)$$

where  $m$  is the mass fraction of the dye. Since the non-linear phase shift is directly proportional to the refractive index, it can be expected to follow a similar relationship according to:

$$\Delta\phi = m\phi_{dye} + (1-m)\Delta\phi_{solvent} \quad (5.39)$$

Figure 5-9 shows the relationship between the extracted value of  $\Delta\phi_{real}$  and mass fraction. The error at each mass fraction has been estimated from experimental parameters to be approximately 10 %. Using the slope and intercept of the line in Figure 5-9, the refractive index of the solute may be obtained from

$$\frac{\Delta\phi_{solute}}{\Delta\phi_{solvent}} = \frac{n_{2,solute}}{n_{2,solvent-eff}} \quad (5.40)$$

where  $n_{2,solvent-eff}$  is the effective  $n_2$  of the solvent which includes contributions from the cuvette and is measured relative to silica at the same intensity and given by

$$n_{2,sovent-eff} = \frac{\Delta\phi_{solvent}}{\Delta\phi_{silica}} n_{2,silica} \quad (5.41)$$

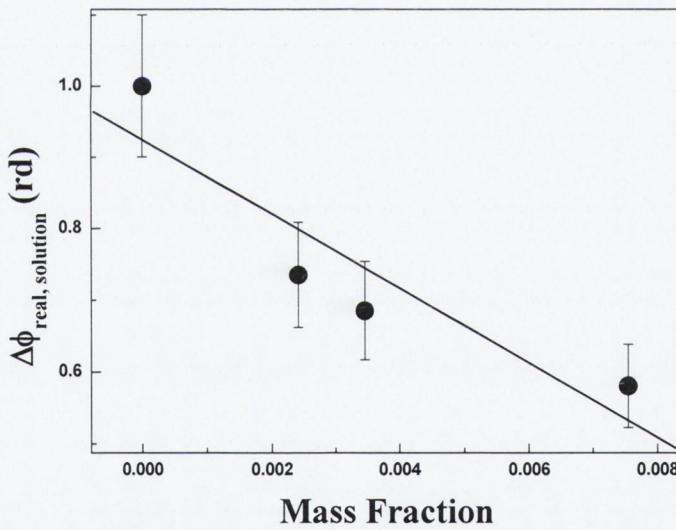


Figure 5-9 Extracted value of  $\Delta\phi_{real}$  of SP35 solution as a function of mass fraction. The resulting real part of the refractive index extracted in this way is  $(1.02 \pm 0.3) \times 10^{-13} \text{ cm}^2/\text{W}$  where the error is the error in the linear fit to the data with weighting of the data points due to their individual error included.

Figure 5-10 shows the open aperture scans at the same concentrations along with the curves calculated according to Eq. 5-35. From the curves in Figure 5-10 it is

possible to extract a value of  $\beta$  for each concentration. To change this to a molecular cross-section, it may be noted that:

$$\sigma_2 = \frac{\beta \hbar \omega}{N} \quad (5.42)$$

Where  $N$  is the number density of active molecules in the solution. Figure 5-11 shows the two-photon absorption coefficient  $\beta$  as a function of number density. From the slope of the linear fit, the TPA cross-section can be extracted. The value obtained from the graph is  $184 \pm 55$  GM where  $1 \text{ GM} = 1 \times 10^{-50} \text{ cm}^4 \text{ photon s}$ .

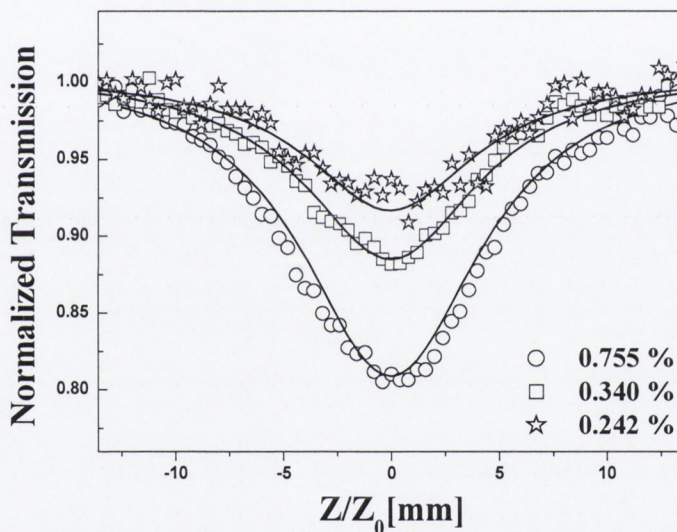


Figure 5-10 Open aperture z-scans of SP35 in chloroform for concentrations of up to 0.755 %. Solid lines are curves calculated according to Eq. 5-3:

$$T(z) = \exp(-\alpha_0 L) \frac{\ln[1 + q_0(z)]}{q_0(z)}$$

Using the approximation in Eq. 5-36, and the expression for the TPA cross-section from Eq. 5-42, the following expression for  $\Delta T(z=z_0)$  as a function of number density is obtained:

$$\Delta T(z = z_0) = -\frac{\sigma_2' N I_0 L_{eff}}{\hbar \omega 2\sqrt{2}} \quad (5.43)$$

Figure 5-12 depicts the maximum change in transmission at  $z=z_0$  as a function of number density. The solid line is a linear fit to the data. Using the value of the slope of this line and Eq. 5.43 the two-photon absorption cross-section of SP35 in chloroform is calculated to be  $197 \pm 40$  GM. This value is in good agreement with the value obtained using the previous method.

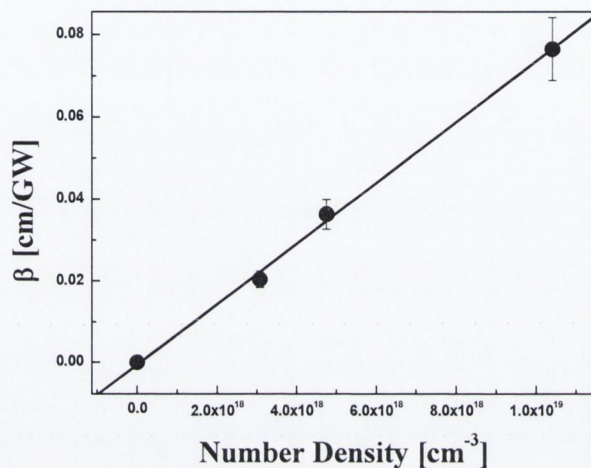


Figure 5-11 Two-photon absorption coefficient versus number density of active molecules for SP35 in chloroform. Straight line is linear fit to data.

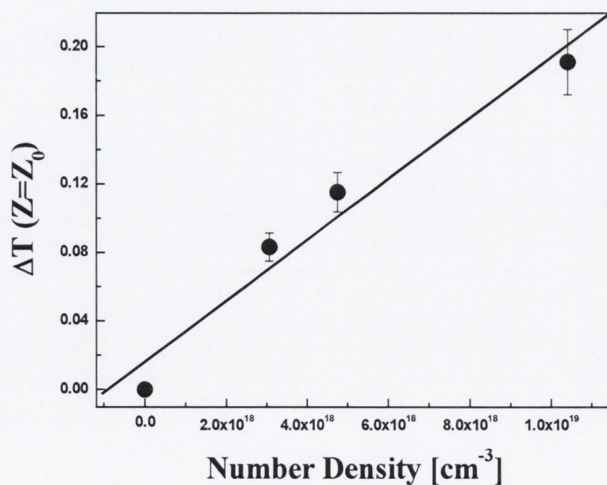


Figure 5-12 Maximum change in transmission as a function of number density of active molecules of SP35 in chloroform.

## 5.7 TPIF-Solid state measurements

### 5.7.1 Introduction

In this section measurements of the TPA cross-section using the TPIF method will be presented. Firstly, an outline of the experimental principle and procedure will be given, then results on several dyes in solid polymer hosts will be presented.

### 5.7.2 Experimental details

#### **Sample Prep**

The host polymers chosen were polystyrene, PMMA and PVP. The polymer and dyes were dissolved in chloroform and spin-cast onto glass slides. The final dye concentration was 1 wt %. The film thickness was measured using white light interferometric profilometry and in all cases films had a thickness of 2-7  $\mu\text{m}$ .

#### **Principle**

The principle behind this experimental technique is depicted schematically in Figure 5-13. This figure shows the process by which photoluminescence is generated under one and two photon pumping. In the case of two-photon pumping, it has been assumed that the final state reached is the  $S_2$  state from where the molecule undergoes rapid relaxation to the  $S_1$  state. This is followed by a downward radiative transition from the same state as for one photon pumping. This assumption is justified in molecules with centrosymmetry where the upward transition from the ground state to the first excited state is spin-forbidden with two-photons. In dipolar molecules however, this transition is more strongly allowed and in many cases, the TPA spectrum peaks at twice the wavelength of the one-photon absorption spectrum indicating that it is the first excited state that is reached under two-photon pumping.

Since the generated photoluminescence intensity under both pumping conditions is related to the absorption cross-section, comparing this emission intensity under one- and two-photon excitation gives information about the two-photon absorption cross-section provided that the linear absorption cross-section is known.

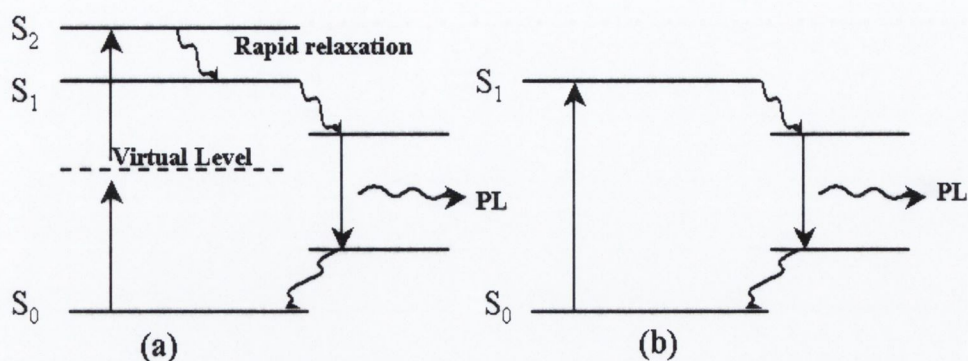


Figure 5-13 Schematic representation of TPIF experimental procedure. (a) Two-photon pumped upconversion, (b) one-photon pumped photoluminescence.

### Experimental procedure

The experimental setup for the measurement is shown in Figure 5-14. The source was a titanium sapphire mode-locked oscillator operating at 76 MHz with a pulse width of approximately 200 fs. The output was reliably tuneable over about 60 nm from 760 nm to 820 nm. The pulse width was measured at each wavelength using an autocorrelator. The beam was split into two sections as shown, one leg of which was frequency doubled in a BBO crystal, the other leg being left at the fundamental frequency. A dichroic mirror was employed which allowed the transmission of the IR beam while reflecting the second harmonic. These beams were carefully aligned so as to co-propagate and overlap exactly at the sample. A second wide aperture lens captured the emitted PL and focussed it into the detection system. The pump beams were filtered from the detected signal using band-pass filters. The detection system used was a monochromator and CCD camera array with a resolution of approximately 2 nm. This allowed the monitoring of the emission spectrum during the experiment. It also allowed any signal due to remnant pump to be eliminated.

During the experiment, the power of the fundamental and second harmonic and the pulse width were measured. Each of the beams was then alternately blocked and the emission due to the other beam measured.

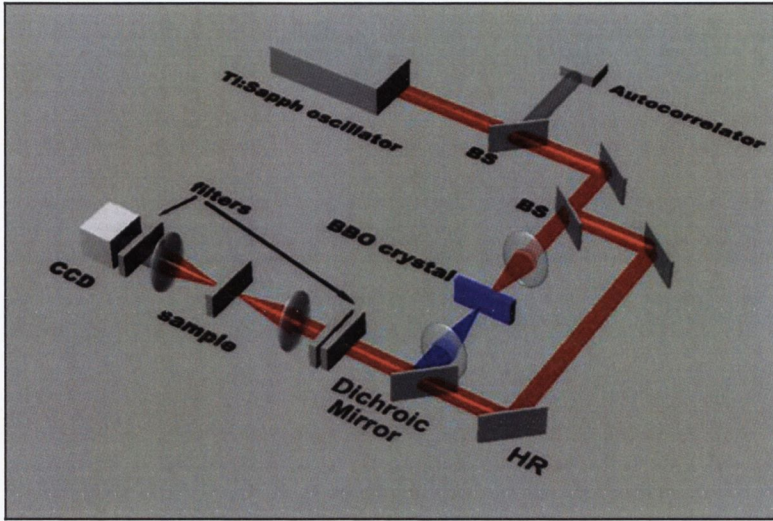


Figure 5-14 Experimental setup used for TPIF measurement. HR: High reflector, CCD: Charge coupled device.

### 5.7.3 Analysis

In the experiment described above the fluorescence spectrum is measured under one and two-photon pumping. The strength of the resulting signal depends on several parameters such as the pump intensity and the absorption cross-section in each case. The signal measured is the time average of the generated photons over the pulse duration and over many pulses.

Assuming the pump beam in both cases has a gaussian temporal and transverse spatial profile, the intensity  $I$  of the pump pulse may be defined as

$$I(x, y, t) = \frac{P_{av}}{r_p} f(t) F(x, y) \quad (5.44)$$

$P_{av}$  is the laser average power,  $r_p$  is the repetition rate of the laser and  $f(t)$ ,  $F(x, y)$ , are the normalized temporal and transverse spatial distributions respectively and are defined as:

$$f(t) = \frac{1}{\sqrt{\pi\tau}} \exp\left[-t^2/\tau\right] \quad (5.45)$$

$$F(x, y) = \frac{2}{\pi w^2} \exp\left[\frac{-2x^2 - 2y^2}{w^2}\right] \quad (5.46)$$

Where  $w$  and  $\tau$  are the 1/e spatial and temporal half-widths of the beam respectively. For a laser beam with a wavelength  $\lambda$ , of beam diameter  $d$  focussed with a lens of focal length  $f$ , the diameter of the airy disk at the focus of the lens is given by:<sup>37</sup>

$$\Delta x = \frac{2.44\lambda f}{d} \quad (5.47)$$

The 1/e half-width is related to the FWHM diameter by:

$$w = \frac{FWHM}{2\sqrt{\ln(0.5)}} \quad (5.48)$$

In addition, the propagation of the beam in the longitudinal direction  $z$ , is expected to follow the Beer-Lambert law such that

$$I(z) = I(0)\exp[-\alpha z] \quad (5.49)$$

where  $\alpha$  is the linear absorption coefficient. Nonlinear absorption effects are expected to be sufficiently weak and the samples sufficiently thin such that it is possible to ignore changes in the beam intensity due to nonlinear absorption.

Under one-photon pumping with femtosecond excitation, the number of emitted photons is proportional to the number of absorbed photons and the fluorescence quantum yield. The time averaged one-photon pumped photoluminescence signal  $PL_I$  is proportional to the number of emitted photons and is given by:

$$PL_I = \frac{K_I \phi_I N L \sigma_I}{h\nu_I} \int_{x,y,z} \int_t I_1(x,y,z,t) \quad (5.50)$$

Where  $K_I$  is a constant,  $\phi_I$  is the quantum yield under one-photon excitation,  $N$  number density of active molecules,  $L$  is the sample thickness,  $\sigma_I$  is the one-photon absorption cross-section measured in  $\text{cm}^2$ ,  $h$  is Planck's constant and  $\nu_I$  is the pump frequency and  $I_1(x,y,z,t)$  is the pump intensity as defined above.

Carrying out the integration, the one-photon pumped photoluminescence is given by:



$$PL_1 = K_1 \phi_1 N \sigma_1 L_{eff} \frac{P_{av}}{rh\nu_1} \quad (5.51)$$

where  $L_{eff}$  is the effective length defined as:

$$L_{eff} = \frac{1 - e^{-\alpha L}}{\alpha} \quad (5.52)$$

$L$  being the sample thickness and  $\alpha$  is the linear absorption coefficient.

Under two-photon pumping, the absorption and hence the PL intensity is proportional to the square of the pump intensity. The two-photon pumped PL signal,  $PL_2$  is then given by:

$$PL_2 = K_2 \frac{\phi_2}{2} N \sigma_2 L \frac{P_{2av}^2}{(rh\nu_2)^2} \int_{-\infty}^{\infty} f^2(t) dt \int_{-\infty}^{\infty} F^2(x, y) dx dy \quad (5.53)$$

The quantum yield under two-photon pumping  $\phi_2$  is divided by two since two incident photons are converted to one PL photon in the upconversion process.

The measured quantity in the experiment is  $S$  the emission spectrum which is integrated across all wavelengths. Combining Eqs. 5.51 and 5.53 results in the following expression for the TPA cross-section.

$$\frac{\phi_2}{\phi_1} \sigma_2 = \frac{S_2}{S_1} \sigma_1 \frac{L_{eff}}{L} \frac{P_{1av}}{P_{2av}^2} hr \frac{V_2^2}{\nu_1} w^2 \tau 2^{3/2} \pi^{3/2} \quad (5.54)$$

The factor involving the ratio of the quantum yields is often left out of the final expression under the assumption that it tends towards unity when the final state reached under one and two-photon pumping is the same and/or the quantum yield is the same under both pumping conditions. This is not the case for quadrupolar dyes under consideration in this study and the factor has been retained. The quantity on the LHS of Eq. 5.54 is a measure of the upconversion efficiency of the molecule and is an essential property in the characterization of TPA molecules for use in upconversion lasing systems and microscopy and will be referred to as the upconversion efficiency parameter. In situations where the quantum yield ratio tends to 1, then this reduces to the two-photon absorption cross-section.

#### 5.7.4 Experimental Results: Commercial Dyes: Rhodamine 6G and Coumarin120

In order to verify the experimental technique, the upconversion efficiency parameters of two commercial dyes were measured and the values obtained compared with those in the literature. There is almost no data in the literature reporting the values of the TPA cross-sections of dyes in solid hosts. Fischer<sup>32</sup> *et al.* measured the TPA cross-section spectra of Rhodamine 6G and Coumarin120 in ethanol solutions using the TPIF method. The values reported in that paper have been included here to provide some reference data.

##### Rhodamine 6G

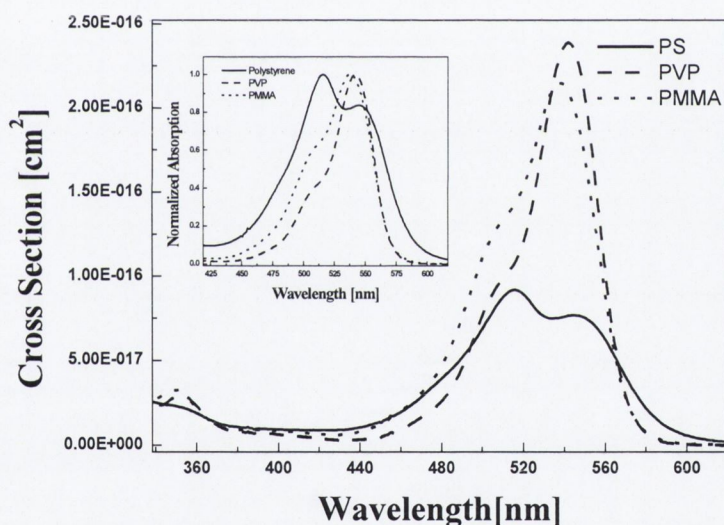


Figure 5-15 Absorption cross-section of Rhodamine 6G in three different polymer hosts. Inset: normalized absorption spectra.

Figure 5-15 shows the linear absorption cross-section spectrum and normalized absorption spectrum of Rhodamine 6G (inset) in the three host polymers. The spectrum in polystyrene is considerably broadened compared to that in the other two hosts and in addition, the absorption cross-section is lower. This is evidence that Rhodamine 6G is not well-dissolved in polystyrene and may be forming aggregates as the solvent evaporates from the thin film.<sup>38</sup>

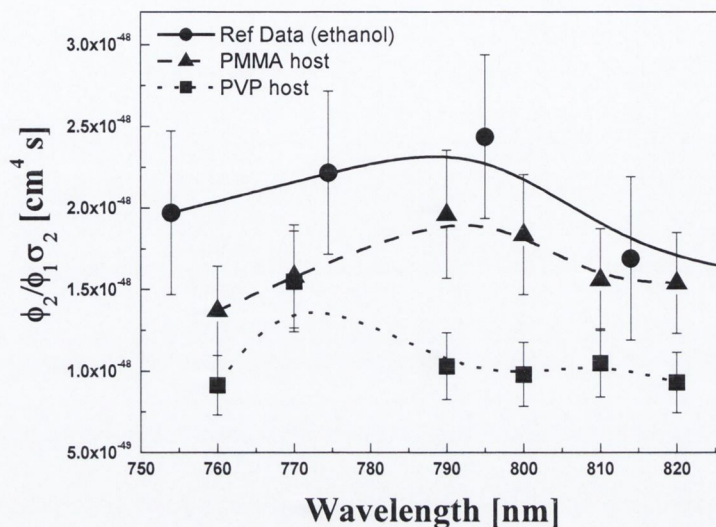


Figure 5-16 Upconversion efficiency parameter of Rhodamine 6G in PMMA and PVP. Also shown is TPA cross-section in ethanol as reported in reference 32. Solid lines are provided to guide the eye.

Figure 5-16 shows the upconversion efficiency parameter of Rhodamine 6G in solid polymer hosts and also, the values obtained in reference 32 in ethanol which were quoted there as the TPA cross-section. It should be noted that since Rhodamine 6G does not dissolve well in polystyrene, thin films of that material exhibit much lower fluorescence under one-photon pumping and barely any upconverted emission making it impossible to use this method of measurement on those samples. The shape of the spectrum in the PMMA host is in good agreement with that in ethanol with the position of the peak indicating that two-photon excitation in Rhodamine 6G takes place into some state other than the  $S_1$  state. The spectrum in PVP is blue-shifted and lower. The reason for this is unclear but may also be related to the solubility of Rhodamine 6G in PVP.

### Coumarin120

Figure 5-17 shows the linear absorption cross-section spectra and normalized absorption spectra of Coumarin 120 in different host polymers. Again, there is a very strong dependence of the linear absorption characteristics of the dye on host polymer with polystyrene giving the lowest cross-section again. Additionally,

Coumarin120 is practically non-fluorescent in polystyrene so its TPA characteristics have not been measured in that host.

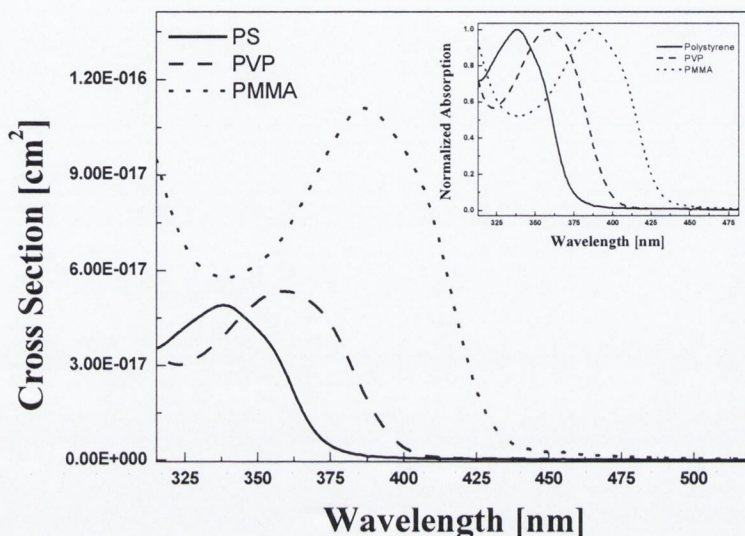


Figure 5-17 Linear absorption cross-section of Coumarin120 in different polymer hosts. Inset: Normalized absorption spectra.

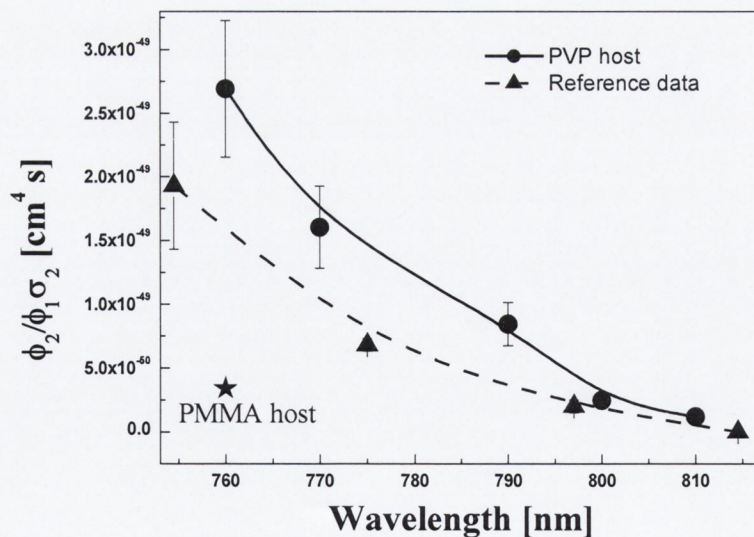


Figure 5-18 Upconversion efficiency parameter of Coumarin120 in PVP and PMMA. Also shown is TPA cross-section of coumarin120 in ethanol taken from ref. 32.

Figure 5-18 shows the upconversion efficiency parameter of Coumarin120 in PVP and PMMA and the TPA cross-section in ethanol taken from reference 32. Due to its very low upconversion efficiency in PMMA, it was only possible to measure one wavelength of the spectrum of coumarin120 in that host and it is an order of magnitude lower than that in PVP. The shape of the spectrum of the dye in PVP is in good agreement with that in solution although it is slightly higher. Overall, the TPA ability of coumarin120 is many times lower than that of Rhodamine 6G. This is a general property of the coumarin class of dyes as compared to the Xanthenes and has been reported previously.<sup>32</sup>

## 5.8 Stilbene dyes: SP35 and SP48

Figure 5-19 and Figure 5-20 show the upconversion efficiency parameter of SP35 and SP48 in the three solid polymer hosts. Also shown in Figure 5-19 is the TPA cross-section of SP35 in chloroform measured using the fs z-scan technique described in section 5.7.2. The upconversion efficiency parameter of both molecules in all three polymers increases towards shorter wavelengths as the peak in the  $S_0$ - $S_2$  transition is approached.

Comparing the magnitude of the TPA between the two molecules, it is clear that SP35 shows a much better performance than SP48. This is in good agreement with measurements and calculations carried out by Albota *et al.*<sup>18</sup> which showed that increasing the conjugation length by inserting more phenylene-vinylene linkages in stilbene molecules increases the quadrupole moment upon excitation which results in an increase in the TPA cross-section. In addition, since the linear absorption of SP48 is blue shifted relative to that of SP35, it can be expected that the TPA absorption peak will also be blue shifted and it is possible that the wavelength range under consideration is further from that TPA peak in SP48 than that in SP35.

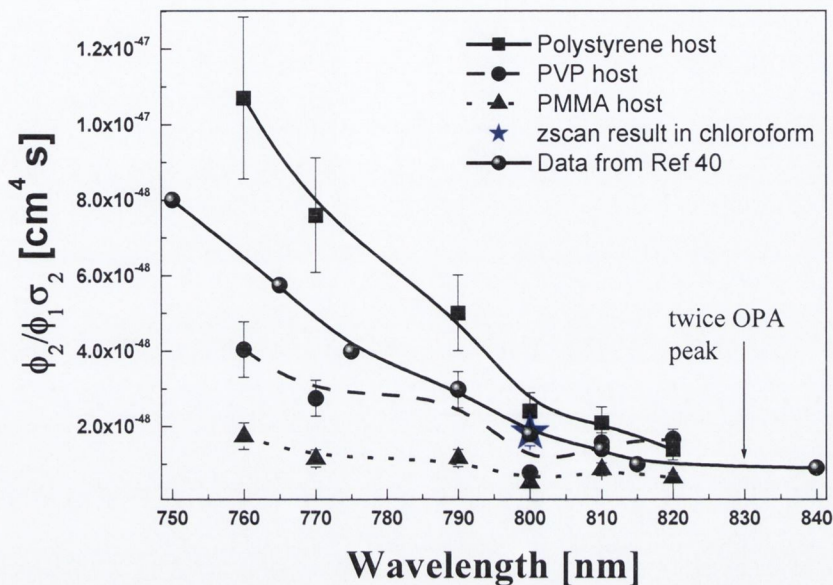


Figure 5-19 Upconversion efficiency of SP35 in different polymer hosts. Also shown is the result of z-scan experiment in chloroform. In addition, data on a similar molecule has also been included from ref. 40.

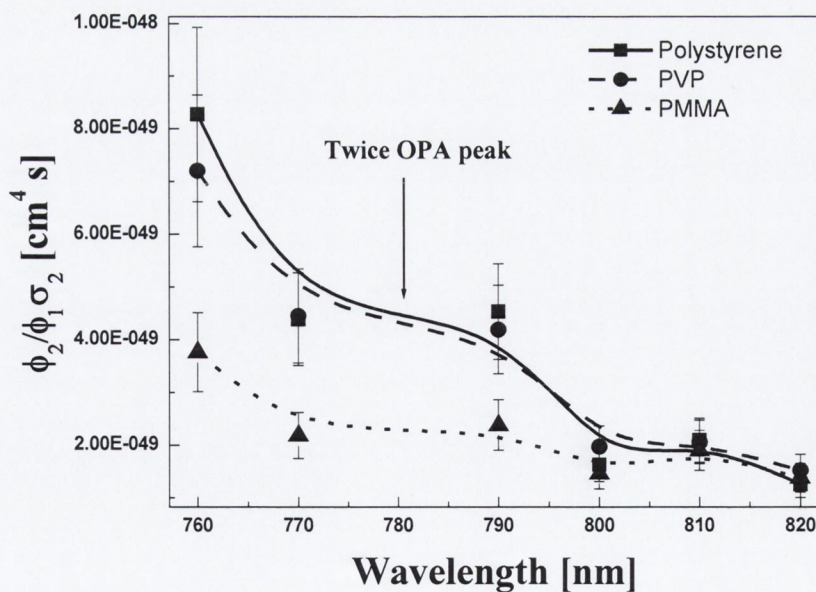


Figure 5-20 Upconversion efficiency parameter of SP48 in different polymer hosts.

Ehrlich *et al.*<sup>39</sup> have measured the TPA cross-section spectrum of SP48 in the ns regime from 550 nm to 750 nm using the nonlinear transmission method and have shown a peak in the spectrum at approximately 675 nm. Although there are no reports of measurements of the TPA spectrum of SP35, Rumi *et al.*<sup>40</sup> have measured the TPA cross-section (in toluene) of a molecule of very similar molecular structure containing additional methyl groups on one of the two terminating phenyl rings at both ends of the molecule. The data from that paper is also included in Figure 5-19. There is reasonable agreement between the two measurements once the different local environment is taken into consideration.

One of the most salient features of both of these graphs is the strong dependence of the upconversion efficiency parameter on the host polymer. There can be several reasons for this although the precise nature of such a dependence is complex one and may be due to several contributions. Since the measured quantity in this experiment is the TPA cross-section times the ratio of the quantum yield under one- and two-photon pumping, this host dependence can be due to changes in either one of these quantities in the different hosts.

## 5.9 Discussion

The following discussion will focus on some of the important parameters that should be considered in explaining the host dependence effect seen in the TPIF measurement results.

### 5.9.1 Local field factor:

The TPA cross-section is defined in terms of the *microscopic* hyperpolarizability according to:

$$\sigma_2(\omega) = \frac{8\pi^2 \hbar \omega^2}{n^2 c^2} L^4 \text{Im} \langle \gamma \rangle (-\omega; \omega, \omega, -\omega) \quad (5.55)$$

where  $\hbar$  is Planck's constant,  $c$  is the speed of light,  $n$  is the refractive index of the material,  $\langle \gamma \rangle$  is the orientational average of  $\gamma$  and  $L$  is the Lorentz factor defined as:<sup>1</sup>

$$L = \frac{n^2 + 2}{3} \quad (5.56)$$

According to Eq. 5.55, it may be seen that the measured TPA cross-section of a material with a certain value of  $\gamma$ , will depend on the refractive index of the host material. Table 5-1 shows the factor  $L^4/n^2$  for the three different host polymers and chloroform.

Table 5-1 Factor  $L^4/n^2$  for the three different host polymers and chloroform.

Material	$L^4/n^2$
Polystyrene	2.05
PVP	1.87
PMMA	1.76
Chloroform	1.65

From this table it can be seen that for the same hyperpolarizability, the TPA cross-section in chloroform should be 80 % of that in polystyrene. The actual measured ratio in the cross-section assuming unity for the QY ratio in polystyrene is 76 % which indicates good agreement between the measurements. It may be thus assumed that the quantum yield ratio in the case of SP35 in polystyrene is unity or close to it. Due to the similar molecular structure of SP48, it is likely that this is the case for that dye too. The difference in local field factor cannot however, explain the difference in observed upconversion efficiency parameter between the three polymers.

### 5.9.2 $S_0$ - $S_1$ transition dipole

In symmetrically substituted quadrupolar dyes, it has been shown that the TPA cross-section, due to the  $S_0$ - $S_2$  transition can be expressed as:<sup>18</sup>

$$\sigma_{s_0 \rightarrow s_1} \propto \frac{M_{01}^2 M_{12}^2}{(E_1 - E_0 - \hbar\omega)^2 \Gamma}$$

Where 1, 0 and 2 refer to the  $S_0$ ,  $S_1$  and  $S_2$  state respectively,  $M_{mn}$  is the transition dipole moment between state  $m$  and  $n$  and  $\Gamma$  is the damping factor or transition



linewidth. The linear absorption cross-section gives information about the transition dipole from the ground state to the first excited state. In chapter 2 it was shown that the linear absorption cross-section of SP35 in PVP is considerably lower than in either PMMA or polystyrene. Since this implies that the transition dipole in PVP is lower, this may go some way to explaining why the TPA cross-section is lower in PVP.

### 5.9.3 Quantum Yield Ratio

Since the linear absorption cross-section of SP35 and to a lesser extent SP48 in PMMA is very similar to that in polystyrene in both strength and width it seems unlikely that the large discrepancy in the upconversion efficiency is due to a large difference in the TPA absorption cross-section. It may be more likely that the ratio of the quantum yield is considerably less than unity. The possible reasons for this will be considered here.

It was noted in chapter 4 that the rate of photodegradation of B2080 in polystyrene was considerably less than that in either PMMA or PVP. Due to the very similar molecular structure of B2080 and SP35, similar spectroscopic behaviour can be expected and it is assumed that the same is true for SP35. A likely reason for this was also outlined as being related to severe torsional motion of the molecule about the double bond in the excited state leading to an increased rate of internal conversion and subsequent photodegradation. Under the influence of the intense IR beam in the case of two-photon pumping, it may be envisaged that there would be a considerable rise in temperature in the solid film that would increase the amplitude of these twisting and bending modes leading to a further drop in the fluorescent quantum yield as internal conversion to the ground state becomes more dominant. This could reduce the ratio of the quantum yield considerably in PMMA since it appears that those motions are facilitated in that polymer more readily. This hypothesis is in agreement with the different rates of photodegradation observed in B2080 in different host polymers as outlined in Chapter 4.

## 5.10 Summary

In conclusion, it has been shown that SP35 has a very large upconversion efficiency parameter. Its performance is considerably higher in polystyrene than that in either PVP or PMMA. In addition, it is considerably higher in the wavelength region considered than that of SP48 which is due to its better molecular design and detuning effects. Since it has been shown in previous chapters that B2080 doped polystyrene shows excellent photostability and very large gain, it is clear that for nonlinear optics and laser applications using stilbene dyes, polystyrene is a well suited host material.

*Table 5-2 Comparison of results of study of SP35 with selected results from literature.*

<b>Molecule</b>	$\lambda_{pump}(\text{nm})$	<b>Emission region</b>	<b>Host/solvent</b>	$\sigma_2 \times 10^{-50}$ <b>(cm<sup>4</sup> s)</b>
SP35 <sup>5</sup>	760	Blue green	polystyrene	1000
Quadrupole molecule (Bis-(styryl)benzene derivative) <sup>40</sup>	745	Blue-green	toluene	805
Push-pull molecule (BT101) <sup>20</sup>	760	Green	THF	~100
Octupolar propeller dye <sup>25</sup>	740	Green	toluene	1080

Table 5-2 gives a comparison of TPA properties of SP35 in polystyrene with some selected results from the literature. As mentioned above, a Bis-(styryl)benzene derivative which is similar to SP35 investigated by Rumi *et al.*<sup>40</sup> gave very similar values of the TPA cross section. To compare these results with molecules with differently engineered geometries, the results for a push-pull type molecule with a similar conjugated backbone to SP35 are also shown.<sup>20</sup> In addition, recent results of

<sup>5</sup> Present study: SP35 in polystyrene

a study on octupolar dyes by Porres *et al.*<sup>25</sup> are shown. From these results it can be seen that SP35 doped polystyrene shows excellent performance, comparable to some of the best materials available.

## References

- <sup>1</sup> R.W. Boyd, *Nonlinear Optics* (Academic Press, Inc. London, 1992).
- <sup>2</sup> M. Göppert-Mayer, *Ann. Phys.*, **9**, 273 (1931).
- <sup>3</sup> W. K. Kaiser, C. G. B. Garrett, *Phys. Rev. Lett.* **7**, 229 (1961).
- <sup>4</sup> W.M. Dennis, W. Blau, D.J. Bradley, *Appl. Phys. Lett.* **47**, 200 (1985).
- <sup>5</sup> C. K. N. Patel, P. A. Fleury, R. E. Slusher, H. L. Frisch, *Phys. Rev. Lett.* **16**, 971 (1966).
- <sup>6</sup> X.H. Yang, J.M. Hays, W. Shan, J.J. Song, , *Appl. Phys. Lett.* **62**, 1071 (1993).
- <sup>7</sup> G.S. He, L. Yuan, P.N. Prasad, A. Abbotto, A. Facchetti, G.A. Pagani, *Optics Communications* **140**, 49 (1997).
- <sup>8</sup> G.S. He, C.F. Zhao, J.D. Bhawalkar, P.N. Prasad, *Appl. Phys. Lett.* **67**, 3703 (1995).
- <sup>9</sup> A.S. Kwok, A. Serpenguzel, W.-F. Hsieh, R.K. Chang, *Optics Letters* **17**, 1435 (1992).
- <sup>10</sup> G.S. He, J.D. Bhawalkar, C.F. Zhao, C.K. Park, , *Appl. Phys. Lett.* **68**, 3549 (1996).
- <sup>11</sup> W. Denk, J.H. Strickler, W.W. Webb, *Science* **248**, 73 (1990).
- <sup>12</sup> M.G. Silly, L. Porres, O. Mongin, P.-A. Chollet, M. Blanchard-Desce, *Chem. Phys. Lett.* **379**, 74 (2003).
- <sup>13</sup> S.M. O'Flaherty, S.V. Hold, M.J. Cook, T. Torres, Y. Chen, M. Hanack, W.J. Blau, *Adv. Mater.* **15**, 19 (2003).
- <sup>14</sup> W.A. Pender, A.J. Boyle, P. Lambkin, K. Mazaheri, D.J. Westland, V. Skarda, M. Sparpaglione, *Appl. Phys. Lett.* **66**, 786 (1995).
- <sup>15</sup> W.H. Zhou, S.M. Kuebler, K.L. Braun, T.Y. Yu, J.K. Cammack, C.K. Ober, J.W. Perry, S.R. Marder, *Science* **296**, 1106 (2002).
- <sup>16</sup> M.A. Albota, C. Xu, W.W. Webb, *Appl. Opt.* **37**, 7352 (1998)
- <sup>17</sup> C. Xu, W.W. Webb, *J. Opt. Soc. Am. B* **13** 481 (1996).

- 
- <sup>18</sup> M. Albota, D. Beljonne, J.-L. Bredas, J.E. Ehrlich, J.-Y. Fu, A.A. Heikal, S.E. Hess, T. Kogej, M.D. Levin, S.R. Marder, D. McCord-Maughon, J.W. Perry, H. Roedel, M. Rumi, G. Subramaniam, W.W. Webb, X.-L. Wu, C. X, *Science* **281**, 1653 (1998).
- <sup>19</sup> G.S. He, T.-C. Lin, P.N. Prasad, R. Kannan, R.A. Vaia, L.-S. Tan, *J. Phys. Chem. B* **106**, 11081 (2002).
- <sup>20</sup> T.-C. Lin, G.S. He, P.N. Prasad, L.-S. Tan, *J. Mater. Chem.* **14**, 982 (2004).
- <sup>21</sup> L. Antonov, K. Kamada, K. Ohta, F.S. Kamounah, *Phys. Chem. Chem. Phys.* **5**, 1193 (2003).
- <sup>22</sup> B.A. Reinhardt, L.L. Brott, S.J. Clarson, A.G. Dillard, J.C. Bhatt, R. Kannan, L. Yuan, G.S. He, P.N. Prasad, *Chem. Mater.* **10**, 1863 (1998).
- <sup>23</sup> L. Beverina, J. Fu, A. Leclercq, E. Zojer, P. Pacher, S. Barlow, E.W. Van Stryland, D.J. Hagan, J.-L. Bredas, S. R. Marder, *J. Am. Chem. Soc.* **127**, 7282 (2005).
- <sup>24</sup> M. Kuzyk, *J. Chem. Phys.* **119**, 8327 (2003).
- <sup>25</sup> L. Porres, O. Mongin, C. Katan, M. Charlot, T. Pons, J. Mertz, M. Blanchard-Desce, *Org. Lett.* **6**, 47 (2004).
- <sup>26</sup> C. Katan, F. Terenziani, O. Mongin, M.H.V. Werts, L. Porres, T. Pons, J. Mertz, S. Tretiak, M. Blanchard-Desce, *J. Phys. Chem. A* **109**, 3024 (2005).
- <sup>27</sup> K. Kamada, K. Matsungaga, A. Yoshino, K. Ohta, *J. Opt. Soc. Am. B* **20**, 529 (2003).
- <sup>28</sup> G.S. He, J.D. Bhawalker, C.F. Zhao, P.N. Prasad, *Appl. Phys. Lett.* **67**, 2433 (1995).
- <sup>29</sup> M. Sheik-Bahae, A.A. Said, T.-H. Wei, D.J. Hagan, E.W. Van Stryland, *IEEE J. Quant. Electron.* **26**, 760 (1990).
- <sup>30</sup> M. Balu, J. Hales, d.J. Hagan, E.W. Van Stryland, *Optics Express* **13**, 3594 (2005).
- <sup>31</sup> M.A. Albota, C. Xu, W.W. Webb, *Appl. Opt.* **37**, 7352 (1998).
- <sup>32</sup> A. Fischer, C. Cremer, E.H.K. Stelzer, *Appl. Opt.* **34**, 1989 (1995).
- <sup>33</sup> N. Mukherjee, A Mukherjee, B.A. Reinhardt, *Appl. Phys. Lett.* **70**, 1524 (1997).
- <sup>34</sup> E.W. Van Stryland, M. Sheik-Bahae in *Characterization techniques and tabulations for organic nonlinear optical materials*, Eds M. Kuzyk and C. Dirk, (Marcel Decker 1998).

- 
- <sup>35</sup> D. Weaire, B.S. Wherret, D.A.B. Miller, S.D. Smith, *Opt. Lett.* **4**, 331 (1974).
- <sup>36</sup> Samoc M., Samoc A. Luther-Davies B., Bao Z., Yu L., Hsieh B., Scherf U, *J. Opt. Soc. Am. B* **15**, 817 (1998).
- <sup>37</sup> A. E. Siegman, *Lasers*, (Oxford University Press, Oxford, 1986).
- <sup>38</sup> A. Ghanadzadeh, M.A. Zanjanchi, *Spectrochimica Acta A* **57**, 1865 (2001).
- <sup>39</sup> J.E. Ehrlich, X.L. Wu, I.-Y.S. Lee, Z.-Y. Hu, H. Röckel, S.R. Marder, J.W. Perry, *Opt. Lett.* **22**, 1843 (1997).
- <sup>40</sup> M. Rumi, J.E. Ehrlich, A.A. Heikal, J.W. Perry, S. Barlow, Z. Hu, D. McCord-Maughon, T. C. Parker, H. Röckel, S. Thayumanavan, S.R. Marder, D. Beljonne, J.-L. Bredas, *J. Am. Chem. Soc.* **122**, 9500 (2000).

# Chapter 6: Microring Laser Cavities

## 6.1 Introduction

In Chapter 4, low-threshold lasing was presented in a Fabry-Perot type asymmetric slab waveguide laser. The feedback in this structure was provided by Fresnel reflections from the end facets which are by their nature lossy and hence provide quite a low cavity quality factor  $Q$ . In order to fully probe the potential of a material for amplification and lasing it is useful to incorporate it into the best possible device structure. One approach to this that has been extensively studied is the use of a high- $Q$  microresonator or microcavity. A microcavity is often described as one in which the cavity volume approaches that of the wavelength cubed. While cavities of quite such small dimensions are not the subject of this study, the structures under investigation do have the property that the cavity length is sufficiently small that the longitudinal modes may be resolved.

Microcavities based on inorganic semiconductor materials have been studied extensively. Yamamoto and Björk were pioneers in this field having studied the behaviour of planar dielectric stack microcavities with particular attention paid to the enhancement of spontaneous emission by the microcavity and resulting large spontaneous emission coupling coefficient into the laser modes.<sup>1,2,3</sup> Slusher *et al.*<sup>4</sup>

and Frateschi *et al.*<sup>5</sup> produced microdisk lasers for use at telecommunications wavelengths using InGaAs/InGaAsP and Rex *et al.*<sup>6</sup> showed whispering gallery mode coupled lasing in a micropillar in the UV spectral region using GaN.

In addition to these studies, there have been many studies of organic light emitting materials incorporated into microcavities. Geometries such as microdroplets,<sup>7</sup> microdisks,<sup>8</sup> planar microcavities<sup>9</sup> and microrings<sup>10</sup> have all been formed from a variety of organic materials such as conjugated polymers, dye-doped polymers and dye solutions. Of these, one of the most easily produced is the microring cavity which can be made by dip coating glass fibers. The first demonstration of this was in 1971 by Weber and Ulrich<sup>11</sup> who coated a glass rod with rhodamine6G-doped polyurethane. The ring was pumped with the output from a nitrogen laser and the emission coupled out of the ring using a prism in loose contact with the rod. They noted that the modes in the ring could be viewed as analogous to the modes in a Fabry-Perot laser resonator whose mirror spacing is equal to half the circumference of the ring.

### 6.1.1 The microring cavity

In general, a microring laser is formed by thinly coating a cylindrical surface with an active material. Resonance occurs around the circumference of the cylindrical structure. Such microrings can be solution processed by dip coating glass fibers into solutions of the active material. Subsequent evaporation of the solvent leaves a coating of the active material on the fiber surface. The final ring is heavily dependent on the material used and the diameter and wettability of the glass fiber. The quality of the resulting resonator depends greatly on the ability to produce a good quality coating on the fiber surface. The rest of this chapter will present the results of a study into the formation and performance of microring cavities with particular attention focussing on the relationship between ring structure and laser performance and characteristics.



## 6.2 The formation of films on fiber substrates

### 6.2.1 Introduction

When placed on a flat horizontal surface, many liquids do not spread uniformly over the surface but form a droplet. The shape of this droplet provides information about the chemical bonding nature of the surface to the liquid. This droplet has a contact angle associated with it, which is shown schematically in Figure 6-1 and is defined as the angle between the tangent to the droplet's surface at the contact point and the tangent to the substrate surface.

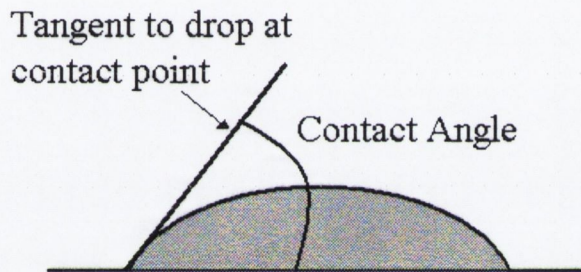


*Figure 6-1 Diagram showing the contact angle between a liquid droplet and a flat horizontal substrate.*

More specifically, the contact angle between a certain liquid and a given substrate depends on the surface energy  $\gamma_s$  of the substrate and the surface tension  $\gamma_l$  of the liquid. The nature of the surface energy is the “dangling” unsatisfied bonds that exist on the surface of materials, which may be satisfied when another material is brought into close proximity. This is the source of adhesion in materials. The source of surface tension in liquids is the same as surface energy in a solid, the distinction being made because fluids will change their shape in response to surface tension/energy.<sup>12</sup> Solids and liquids tend to minimize their energy/tension and in general there is an equilibrium droplet shape for a given substrate which in the case of a flat horizontal surface is a spherical droplet.<sup>13</sup> If the surface tension of the droplet is below the surface energy of the surface, the droplet cannot hold its shape and the fluid will flow over the surface. In this case, the fluid is said to wet the

surface. The thickness of the resulting film is dependent on the strength of the Van Der Waals forces.<sup>14</sup> Thus high wettability is associated with vanishing contact angle on a flat substrate.

A fluid that fully wets a flat substrate of a given material may not wet the same material in cylindrical or fiber form and the wettability of a surface depends not only on the chemical nature of the material but the geometry of the substrate. McHale *et al.*<sup>15</sup> have shown that the equilibrium shape of a droplet on a small cylindrical surface can be a barrel droplet type or a clam-shell type. These two shapes are shown in Fig 6-2. (adapted from reference 15). In this study only droplets of the Barrel type have been observed which have coatings that cover the entire circumference of the fiber. While vanishing contact angle on a flat surface is indicative of complete wetting, the contact angle of a Barrel type droplet can go to zero (and in fact there is a point of inflexion on the surface), without resulting in full wetting of the fiber.

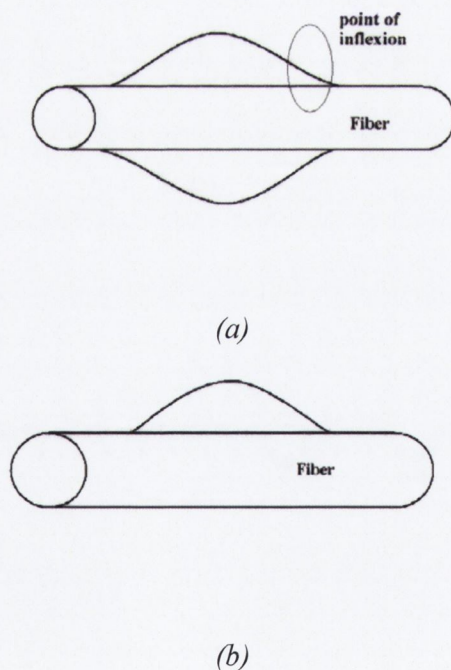


Figure 6-2 Equilibrium droplet shapes on fiber substrates (adapted from reference 15). (a) Barrel droplet shape, (b) Clam-shell droplet shape.

Thus far, consideration has only been given to the formation of stable droplets on substrates where the volume of the liquid is constant. In this study, solutions of

volatile solvents such as toluene were used, so it is important at this point to consider what happens to droplets made up of material suspended in a volatile liquid. An everyday example of this is the formation of ring-like deposits after the evaporation of water from coffee or salt solution. Deegan *et al.*<sup>16</sup> have attributed this phenomenon to a type of capillary flow and have shown that the evaporation of the suspending liquid causes a flow of material to the edge of the droplet so that once all the liquid has evaporated, there will be more material at the edge of the ring than in the centre.

### 6.2.2 Ring formation: Experimental results

The microring cavities used in this study were composed of 0.1 – 1 wt % dye-doped polystyrene, drawn from 50 g/l toluene solutions onto silica fibers of different diameters. Initial studies on dip-coating silica fibers showed that higher concentrations of polymer formed very thick and inhomogeneous layers. Lower concentrations meant that the solution slid off the surface providing very poor wetting of the fiber. To further probe the wetting of silica with this material, contact angle analysis was used on flat silica substrates and optical microscopy was used to characterise the coated fibers.

#### **Contact Angle Measurements**

Figure 6-3 is a screen shot of the contact angle analysis software used in this study. A small droplet of the particular solution was dropped onto the surface and a photograph of the droplet was taken after it had settled on the surface. Lines are drawn along the surface of the droplet and the software calculates the tangent to the droplet surface and the contact angle. From this the average contact angle of the left and right side of the droplet is calculated. The measurement is repeated over many drops to reduce the inherent variance in droplet shape.

Contact angle analysis was carried out on silica substrates that were cleaned in an alcoholic potassium hydroxide (KOH) cleaning solution and subsequently washed in deionised water and solvents to remove any residual material on the surface. An identical pre-treatment was used on the silica fibers prior to dip coating.

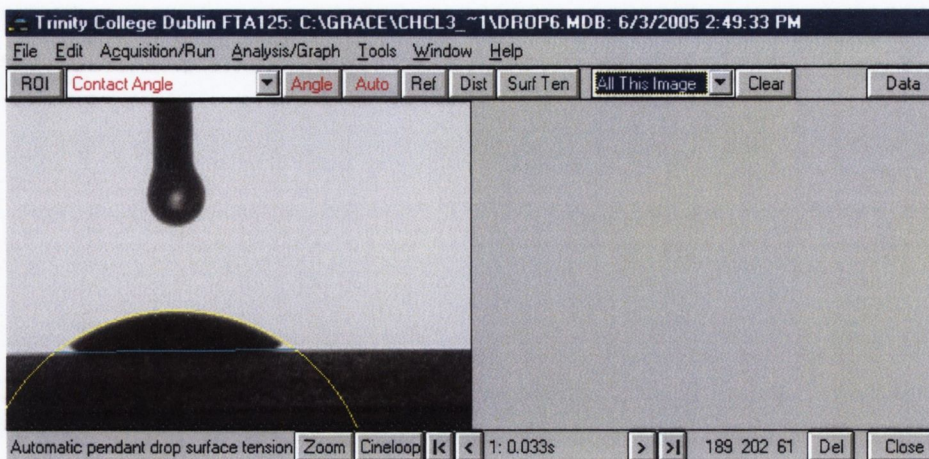


*Figure 6-3 Screen shot of contact angle analysis software used to calculate contact angle on flat silica substrates.*

The average contact angle of polystyrene and B2080 in toluene at a concentration of 50g/l on the cleaned substrates is 20°. Anything less than 20° is considered low so this material provides reasonably good wetting of silica although it does not completely wet the surface.

### **Ring formation on fibers**

As outlined above, the actual wetting of a surface depends on both the chemical nature of the materials and the geometry of the substrate. While the contact angle measurements carried out give an indication of whether or not a solution could provide good wetting on a fiber substrate, the degree of wetting can only be assessed by carrying out measurements on actual fibers. To that end, 200-micron fibers were dip-coated in the same solutions and optical microscopy was used to examine the resulting coatings.

The images in the following section were taken on two different microscopes. One was an uncalibrated low-resolution microscope. The other had several objectives each of which was calibrated using a graticule. At each magnification, a fluorescence image of the device was taken in addition to an image under normal illumination. In this way, it was possible to identify the coating material as opposed to other contaminants or inhomogeneities on the fiber surface. In images where the magnification is not stated, it is unknown. These images are just used qualitatively and no quantitative analysis is carried out on them.

Figure 6-4 shows a 200  $\mu\text{m}$  diameter fiber coated with doped polystyrene from a toluene solution. The rings have been excited with a UV photodiode for clarity. Figure 6-5 shows an image of the microrings at a magnification of 10X. There is evidence at this magnification of bubbles and a large degree of surface irregularity.

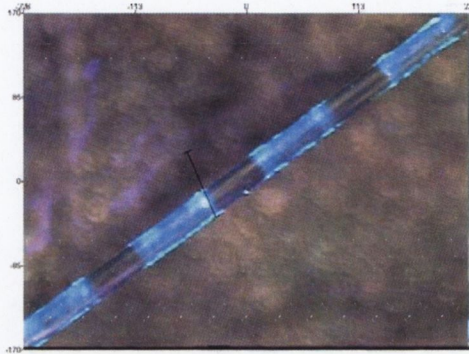


*Figure 6-4 Dye doped polystyrene microrings formed from toluene solutions on 200  $\mu\text{m}$  diameter fiber.*

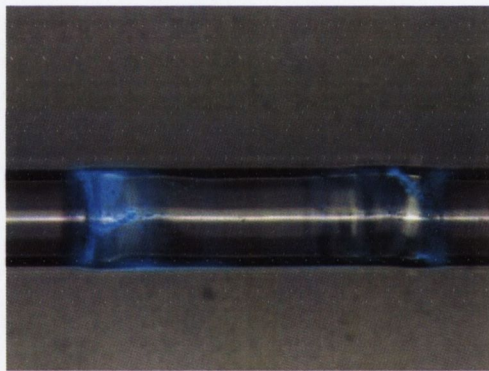


*Figure 6-5 Image of microring on 200  $\mu\text{m}$  diameter fiber at a magnification of 10 X. Bubbles and inhomogeneities are evident on surface.*

It can be seen from the images that the solution has not completely wetted the surface with the result that droplets have formed on the fiber. Subsequent evaporation of the solvent has caused the flow described in section 6.2.1 to make the ends of each ring slightly thicker than the middle. While the rings are inhomogeneous on a certain scale, there are sections of the ring where the surface is smooth enough to provide a good enough cavity for lasing.

Image-Pro© software was used to analyse the images. The sizes of the fiber and the microrings were measured using a line-length tool in order to get an estimate of the thickness of the coating. At 10 X magnification, the fiber diameter was measured

using this method on several images and an average value obtained. There is inevitable error in this measurement due to the curved nature of the fiber surface. However, this method does provide an estimate and since the fibers and rings have quite a large diameter, the error is manageable. The average diameter of the fiber measured using this method was 200  $\mu\text{m}$ . The thick rings at the ends of each coated section had an average thickness of 210  $\mu\text{m}$  and the central smooth part of the coating had an outer average diameter of 204  $\mu\text{m}$ .

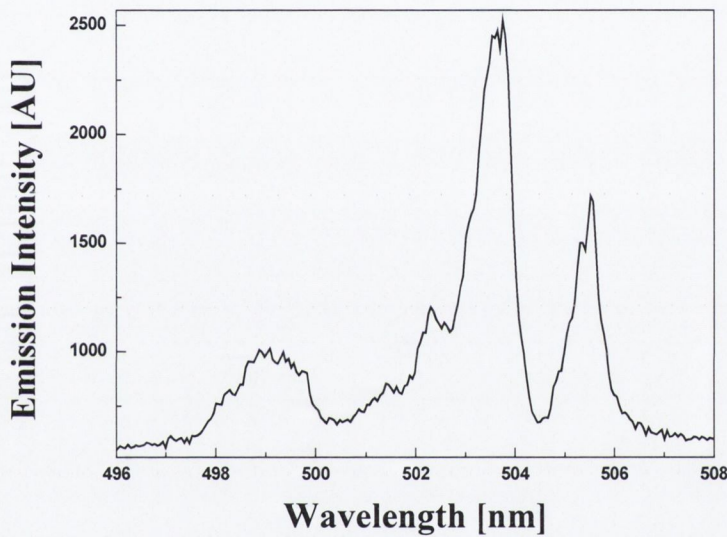


*Figure 6-6 Emission spectrum from thickly coated 200 mm diameter microring laser*

It was observed for devices of this type that lasing occurred at the areas of thicker coating. The emission was highly multimode and the mode spacing was such that it was not possible to resolve individual peaks in the spectrum as shown in Figure 6-6 which is a typical emission spectrum from such a device. Since the coatings are quite thick, this is probably in part due to the presence of several radial modes in the spectrum which make it very complicated. Smaller diameter fibers and thinner coatings produced better results both in regard to lasing threshold and more well-defined spectral characteristics.

Finally, the last method employed in the formation of microrings used the inner surface of glass capillaries as the substrate. The capillaries had a nominal core diameter of 100  $\mu\text{m}$ . The solution was sucked up into the capillary and subsequently blown out using a modified pipette. This resulted in a thin coating on the inside of the capillary walls, which could then be pumped transversely to give microring lasing. A schematic of such a ring is shown in Figure 6-7.

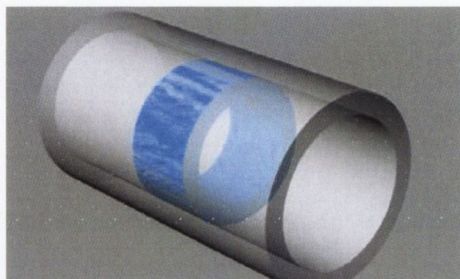


*Figure 6-7 Schematic of microring cavity formed on the inside of a glass capillary.*

### 6.3 Characterization of laser devices: Experimental set-up

In general, the microrings in this study were all characterized using the same experimental setup.

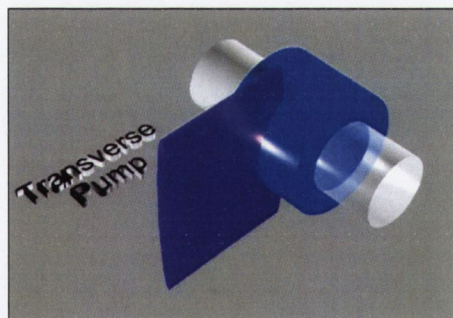


*Figure 6-8 Schematic of transverse pumping of microring using a stripe pump beam geometry.*

The microrings were photo-pumped with the 355 nm output of a Nd:YAG laser. The pulse width was 3 ns at a repetition rate of 10-15 Hz. The beam was expanded into a vertical stripe using cylindrical lenses and the microring pumped perpendicularly to the capillary axis. A 3 mm diameter light-guide was placed above the excited region to collect the radial emission and the spectrum measured using a monochromator and CCD camera, which had a maximum resolution of 0.07 nm.

The pump pulse power was measured on a calibrated laser power meter or laser energy meter. The fluence calculation is outlined in Appendix I. This configuration is referred to in the following sections as transverse pumping and is shown schematically in Figure 6-8.

## 6.4 The wave equation in cylindrical coordinates

Maxwell's equations were used in previous chapters to derive the wave equation and apply it to the asymmetric slab waveguide. In order to adapt this analysis to the cylindrical shape of the microrings under investigation, the wave equation must be transformed to cylindrical coordinates. Solutions will then describe the types of modes that a microring is capable of supporting. The Helmholtz form of the wave equation is:

$$\nabla^2 \underline{E} + k^2 \underline{E} = 0 \quad (6.1)$$

where  $k^2 = \omega^2 n^2 / c^2$ , where  $\omega$  is the angular frequency,  $n$  is the refractive index and  $c$  the velocity of light in a vacuum. Since the waveguides in question have cylindrical symmetry, it is more convenient to re-write this equation in cylindrical coordinates which are shown schematically in Figure 6-9.

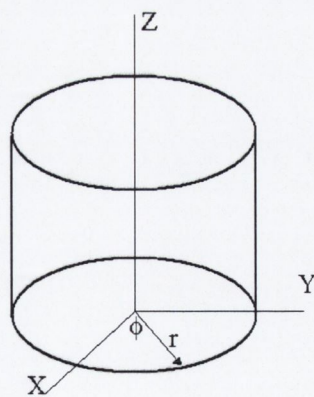


Figure 6-9 Cylindrical coordinate system.



The relationship between normal Cartesian coordinates and the new cylindrical coordinates may be expressed as:

$$\begin{aligned} r &= \sqrt{x^2 + y^2} \\ \phi &= \tan^{-1}\left(\frac{x}{y}\right) \\ z &= z \end{aligned} \quad (6.2)$$

In cylindrical coordinates, the Laplacian operator is given by:

$$\nabla^2 = \frac{1}{r} \frac{\partial}{\partial r} \left( r \frac{\partial}{\partial r} \right) + \frac{1}{r^2} \frac{\partial^2}{\partial \phi^2} + \frac{\partial^2}{\partial z^2} \quad (6.3)$$

Treating the component of the electric field polarized parallel to the cylinder axis (TE mode) and applying Eq. 6.3 to Eq. 6.1 gives:

$$\frac{\partial^2 E_z}{\partial r^2} + \frac{1}{r} \frac{\partial E_z}{\partial r} + \frac{1}{r^2} \frac{\partial^2 E_z}{\partial \phi^2} + \frac{\partial^2 E_z}{\partial z^2} + k^2 E_z = 0 \quad (6.4)$$

The method of separation of variables can be used to find a full solution:

$$E = R(r)\Theta(\phi)Z(z) \quad (6.5)$$

Applying this to Eq. 6.4 and multiplying by  $r^2/R\Theta Z$  gives:

$$\left[ \frac{r^2}{R} \frac{\partial^2 R}{\partial r^2} + \frac{r}{R} \frac{\partial R}{\partial r} \right] + \left[ \frac{1}{\Theta} \frac{\partial^2 \Theta}{\partial \phi^2} \right] + \left[ \frac{r^2}{z} \frac{\partial^2 Z}{\partial z^2} \right] + k^2 r^2 = 0 \quad (6.6)$$

Unlike a cylindrical waveguide such as a fiber, the modes in a microdisk or microring are stationary in the  $z$  direction and propagate around the perimeter of the device. In the case of a microdisk of thickness  $d$ , Chin<sup>17</sup> *et al* constructed the eigenmodes of a microdisk of thickness  $d$  and radius  $R$  by summing  $+z$  and  $-z$  propagating modes to form stationary modes in the  $z$  direction. In the case of the microrings studied here, there is no definite boundary in the  $z$ -direction. Frovlov<sup>18</sup> *et al.* have measured the angular dependence of the emission from a polymer microring and found that the lateral size of the ring mode was smaller than the (100

$\mu\text{m}$ ) excitation stripe used. In this case, it cannot be said that the ring is bounded by gain guiding but rather the  $z$ -limit is placed on the ring by inhomogeneities in the polymer film. In the absence of a definite boundary in the  $z$ -direction, the  $z$ -dependence of the mode will be neglected and focus will be placed on the solutions to the equation that are stationary in the radial and azimuthal directions.

A solution to the azimuthal function is:

$$\frac{1}{\Theta} \frac{\partial^2 \Theta}{\partial \phi^2} = -m^2 \quad (6.7)$$

which has a solution:

$$\Theta = e^{im\phi} \quad (6.8)$$

If  $z$  dependence in Eq. 6.6 is neglected, substitution of Eq. 6.7 into Eq. 6.6 and multiplying by  $R/r^2$  gives:

$$\frac{\partial^2 R}{\partial r^2} + \frac{1}{r} \frac{\partial R}{\partial r} + \left( k^2 - \frac{m^2}{r^2} \right) R = 0 \quad (6.9)$$

This is a modified form of the Bessel differential equation, which has the general solution:

$$R(r) = A_m J_m \left( X_m^N \right) \quad (6.10)$$

where  $J_m$  is a Bessel function of the first kind and  $A_m$  is a normalization constant.  $X_m^N$  is a size parameter given by:

$$X_m^N = \frac{n_{\text{eff}} \omega_{m,N} r}{c} \quad (6.11)$$

where  $\omega_{m,N}$  are the resonant frequencies of the structure and  $n_{\text{eff}}$  is the effective index of a given mode. The subscripts  $m$  and  $N$  denote the azimuthal and radial mode number respectively. The final solution for the transverse field  $\psi(r, \phi)$  can be written:

$$\psi(r, \phi) = A_m J_m(X_m^N) e^{\pm im\phi} \quad (6.12)$$

It can be seen from this solution that for a given  $m$  there is a two-fold degeneracy representing two counter-propagating waves which interfere to form the resonant standing-wave mode in the azimuthal direction. The value of  $m$  gives the order of the Bessel function and the number of nodes in the azimuthal function. For each value of  $m$  there are many resonant frequencies, each corresponding to a different number of nodes in the radial direction, which are denoted by the subscript  $N$ .

All of the microring devices studied this work, have a similar structure, namely that of a thin polymer coating on a transparent dielectric cylinder, of either glass or in the case of the coated capillary devices, air. It is pertinent at this point to consider what types of modes this type of structure is capable of supporting.

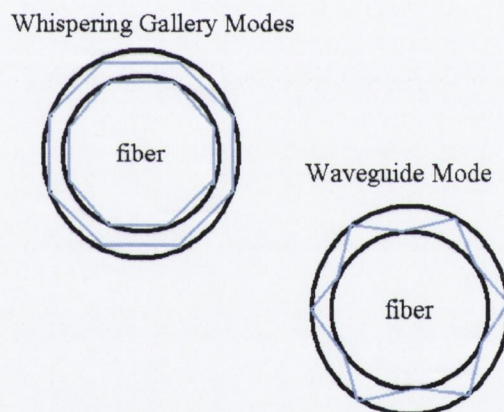


*Figure 6-10 Two types of modes in cylindrical cavity. Whispering gallery modes propagate by successive reflections at the outer boundary, while waveguide modes propagate by alternating reflections from inner and outer boundaries.*

There are, in general two types of modes that can be supported by this type of structure, which can be described as either whispering gallery modes (WGM) or waveguide (WG) modes. These modes are depicted schematically in Figure 6-10. Waveguide modes are similar to waveguide modes found in asymmetric planar waveguides where total internal reflection from the air-polymer interface and the polymer glass interface guides the light around the circumference of the cylinder. Whispering gallery modes are distinct in that total internal reflection only occurs at one interface. In the case of a WGM mode in the polymer layer, successive

reflections from the polymer-air interface guide the light in the layer, while in the case of a WGM mode in the actual fiber, reflections from the glass polymer interface guide the mode if the refractive index of the polymer is lower than that of the glass.

The simplest mode of such microdisks or microrings is the whispering gallery mode where  $N=1$  in Eq 6.12. The resonant frequency of a disk or ring with outer radius  $R$  can be obtained by making the approximation that the field is zero at the boundary. Hence:

$$\psi(R, \phi) = 0 \quad (6.13)$$

i.e. the root of the equation:

$$J_m(X_m^1) = 0 \quad (6.14)$$

That is to say, the value of the first zero in the Bessel function of order  $m$ , which gives the resonant frequencies as:

$$\omega_{m,1} = \frac{X_m^1 c}{n_{eff} R} \quad (6.15)$$

where  $n'_{eff}$  is the effective index of the whispering gallery modes in the disk. Frateschi *et al.*<sup>5</sup> have shown that solutions subject to the boundary condition Eq. 6.13, have no net energy flux in the radial direction, i.e. no energy can escape the cavity. This does not correspond to the devices in this study which have a definite radial emission. However in the limit of large  $m$  the radial flux is very small so the whispering gallery mode behaviour is a good approximation. For small  $m$ , solutions depart significantly from the WGM approximation.

As stated above, the polymer layer can support whispering gallery modes. In the absence of the polymer layer, light in the fiber can also propagate around the fiber circumference in a whispering gallery mode. When the polymer layer is deposited on the glass surface, the whispering gallery modes become lossy, since the polymer has a higher refractive index. However the structure is still capable of supporting these modes as has been shown by Frovlov *et al.*<sup>18</sup> Since these modes are lossy,

they will have a lower Q value than those in the polymer layer and will therefore not dominate the emission.

Equation 6.6 can be applied to the waveguide modes in the polymer layer, which also have cylindrical symmetry giving resonant modes defined by Eq. 6.12. In the limit of large  $m$ , these modes can also be thought of as similar to those in a Fabry-Perot resonator where the mirror spacing is equal to half the circumference of the ring.<sup>11</sup> The resonant wavelengths of such a cavity are given by the simple standing wave condition:

$$M\lambda = 2\pi Rn_{eff} \quad (6.16)$$

Where  $n_{eff}$  is the effective index of the modes,  $M$  is the order of the mode and for whispering gallery modes with large  $M$ ,  $M \approx X_m^1$ .<sup>19</sup>

The wavelength spacing between the modes is given by the cavity free spectral range (FSR),  $\Delta\lambda = \lambda_{m+1} - \lambda_m$ :

$$\Delta\lambda = \frac{\lambda^2}{2\pi n_{eff} R} \quad (6.17)$$

Using Eq. 6.17 it is possible to calculate the factor  $Rn_{eff}$  from the wavelength spacing in a particular part of the emission spectrum from a given device, if the peaks are evenly spaced and well described by WG modes. Substituting this value into Eq. 6.15 allows for the calculation of the size parameter at the particular wavelength using mathematical tables. The size parameters on either side of this value can then be used to predict the position of the neighbouring wavelength peaks by noting  $\lambda = \Delta\lambda X_m$ . Good agreement between this theory and the measured position of the peaks indicates that the real modes are well described by the lowest order radial WG mode in the polymer layer.

An interaction between the WGM modes and the WG modes supported by a structure can also be used to explain some interesting phenomenon observed such as the modulation of the laser emission spectrum from a device, as the WGM and the WG modes move in and out of resonance.<sup>18</sup>

A detailed analysis of the modes supported in a given device, allows a better understanding of the physics of the device and provides potential for improving the device further, for example by making the polymer layer thin enough such that it only supports the lowest order radial modes. Additionally, if the radius of the device is sufficiently small such that the mode spacing is wider than the gain bandwidth, single mode operation is possible. Devices with such small modal density of states are extremely interesting from a fundamental point of view since the fluorescence from the molecules can be enhanced (or inhibited) by the presence of the micro-cavity due to quantum electrodynamic effects (QED). This can lead to a large spontaneous emission coupling coefficient  $\beta$ , and hence in theory “thresholdless” lasing may be approached. In any case, even in the regime where QED is not significant, lasers with smaller mode volume and higher quality are desirable, because of their lower threshold since emission takes place into only a few modes of the cavity.<sup>20</sup>

## 6.5 Quality factor

Optical resonators and cavities have a quality factor,  $Q$  associated with them which is a measure of the ability of the resonator to store up energy. The  $Q$  of a cold-cavity is used to define the cavity quality and is defined as  $2\pi$  times the number of optical cycles for the field to decay to  $1/e$  times its initial value or

$$Q = \omega t_c \quad (6.18)$$

where  $\omega$  is the angular frequency and  $t_c$  is the photon lifetime in the cavity. There are several factors that influence the  $Q$  of a given cavity and their contributions may be added as follows:<sup>21</sup>

$$Q^{-1} = Q_{rad}^{-1} + Q_{scat}^{-1} + Q_{abs}^{-1} \quad (6.19)$$

Where  $Q_{rad}^{-1}$  denotes the intrinsic radiation loss due to the surface curvature,  $Q_{scat}^{-1}$  is a contribution due to surface scattering and inhomogeneity, and  $Q_{abs}^{-1}$  represents the intrinsic losses associated with ground state reabsorption.  $Q_{rad}^{-1}$  decreases exponentially with increasing size and in the case of rings with diameter  $\sim 100 \mu\text{m}$

this contribution may be neglected. Surface imperfections and inhomogeneities can make  $Q_{scat}^{-1}$  non-negligible. From the microscope images taken of the devices studied, there is evidence of irregularity in the coating. This contribution can be considerably lowered however, by improving the production process for the microrings. The final contribution in Eq. 6.19 is a property that is inherent to a given material and cannot be changed. Its value may be estimated from the following equation:

$$Q_{abs} = \frac{2\pi n}{\alpha\lambda} \quad (6.20)$$

Where  $n$  is the refractive index at wavelength  $\lambda$  and  $\alpha$  is the residual absorption at the lasing wavelength.

There are several methods with which to estimate the  $Q$  of a laser cavity. In cavities that are sufficiently small such that spontaneous emission enhancement is evident,  $Q$  can be estimated from the linewidth  $\Delta\lambda$  of the enhanced spontaneous emission peaks:<sup>18</sup>

$$Q = \frac{\lambda}{\Delta\lambda} \quad (6.21)$$

In larger cavities where there is no spontaneous emission enhancement, no lines appear in the spectrum below threshold. Some authors<sup>22</sup> have used the approximation that the linewidth does not change appreciably above the lasing threshold and Eq. 6.21 can provide an approximate value for  $Q$ . It could also be argued that the free spectral range defined as the frequency spacing between modes in the cavity is the maximum value of the linewidth since if the lines were broader than the FSR, then the detection system would not be able to resolve the individual peaks<sup>18</sup>. In this case it may be possible to get a lower estimate of  $Q$  using Eq. 6.21 where  $\Delta\lambda$  is the wavelength spacing between the emission peaks.

## 6.6 Device Characterization: Results and Analysis

### 6.6.1 Capillary Device

#### Device Description

The microring was drawn onto the inner surface of a silica capillary which had a nominal inner diameter of  $100 \pm 4 \mu\text{m}$ , from a 0.1 wt % solution of SP35 in polystyrene. The polymer was dissolved at a concentration of 50 g/l in toluene. Once the solution was drawn into the capillary, it was quickly evacuated using a modified pipette to leave a thin coating on the inner surface of the capillary as shown schematically in Figure 6-11. While it wasn't possible to estimate the thickness of the layer inside the capillary, it is assumed that the layer is of the order of 1-2  $\mu\text{m}$ . This is confirmed by the presence of only the lowest order radial mode in the emission spectrum.

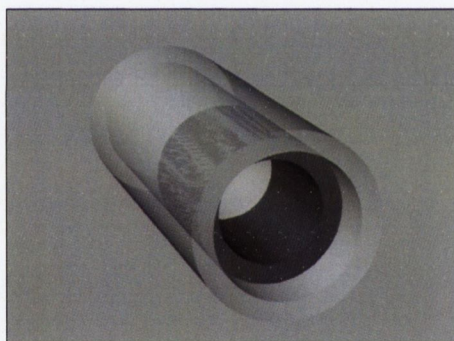


*Figure 6-11 Schematic representation of microring cavity formed on inner surface of silica capillary.*



## Spectral analysis

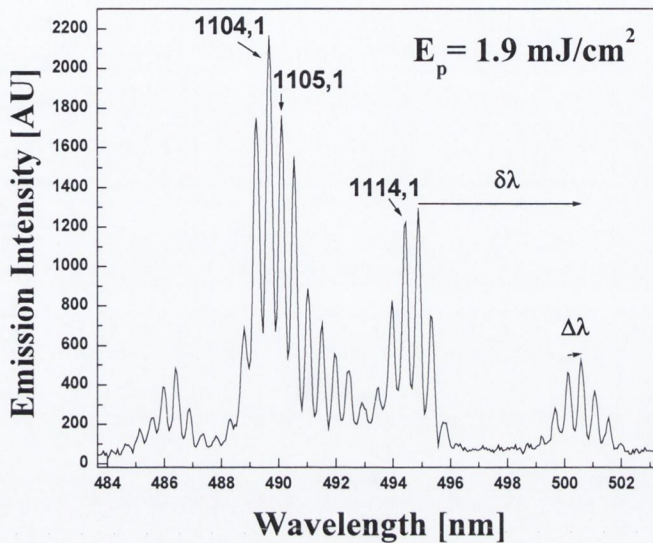


Figure 6-12 Typical emission spectrum from microring at a pump fluence of  $1.9 \text{ mJ/cm}^2$ . Strong modulation of the emission spectrum is evident. Some of the peaks have been labelled with the order of the Bessel function.

Figure 6-12 shows the emission spectrum from the microring at a transverse pump fluence of  $1.9 \text{ mJ/cm}^2$ . The emission is highly multimode and contains only the lowest order radial mode of the ring. To show this, it is possible to apply the analysis outlined in section 6.4 to label the peaks in the emission spectrum with the azimuthal mode number and thus show that the emission spectrum is well defined by the lowest order WG mode in the polymer layer.

For example, the mode spacing between the peaks at  $489.24 \text{ nm}$  and  $489.677 \text{ nm}$  is  $0.436 \text{ nm}$ . Using Eq. 6.17;  $\Delta\lambda = \frac{\lambda^2}{2\pi n_{\text{eff}} R}$ , the product  $Rn_{\text{eff}}$  can be calculated to be

$87.57 \mu\text{m}$ . Assuming that the modes are well confined within the polymer layer, the approximation  $n_{\text{eff}} = n_{\text{polymer}}$  can be made. This gives a ring diameter of  $110 \mu\text{m}$ , which is in reasonable agreement with the nominal ring diameter obtained from the manufacturer of  $100 \pm 4 \mu\text{m}$ .

Taking this value of  $Rn_{eff}$  Eq. 6.15 is used to calculate the value  $X_m$ . Using mathematical software (Mathematica©) it is possible to find the value of  $m$  that has its first root at  $X_m$ . In the case of the wavelengths just mentioned this gives a value of  $m = 1104$ . This procedure can be applied to many peaks in the spectrum as described in section 6.4 and some of the peaks in Figure 6-12 are labelled accordingly.

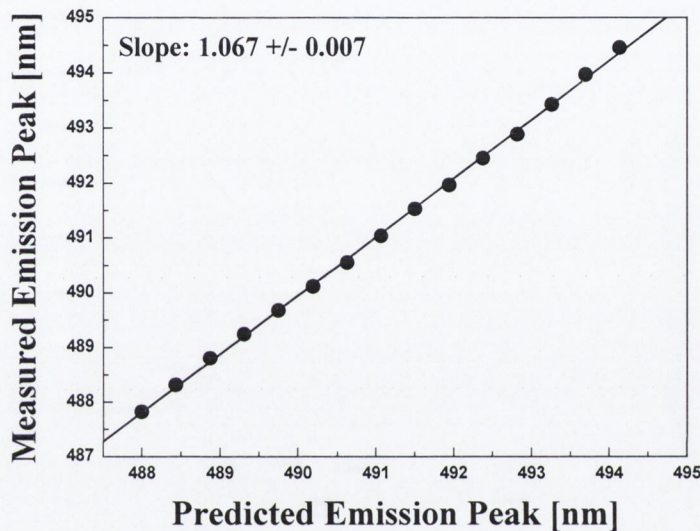


Figure 6-13 Measured position of spectral peak from capillary microring versus predicted peak using method outlined above. Slope of very close to 1 indicates good agreement between theory and experiment.

In Figure 6-13 the peak predicted using this method against the measured value for several of the peaks around the centre of the spectrum has been plotted. The relationship is linear with a slope of close to 1 which indicates good agreement with theory. The fact that the slope is not exactly 1 probably represents a slight offset in the calibration of the detection system or a lack of sensitivity. It is thus possible to conclude that the emission from the rings is indeed well described by the lowest order radial mode in the polymer layer.

Another salient feature of the emission spectrum is a very strong modulation of the emission with wavelength. Similar behaviour has been observed previously by Frovlov *et al.*<sup>18</sup>, and Dou *et al.*<sup>23</sup> According to Frovlov, the explanation for this is

that in addition to supporting WG modes in the polymer layer, the structure is capable of supporting WGM propagating around the edge of the core of the structure. Since the polymer layer has a higher refractive index, these modes are lossy but can cause a modulation of the Q of the WG modes which results in a modulation of the spectrum as the WG modes and WGM modes move in and out of resonance. Frolov *et al* showed that a structure without a full ring structure was still capable of supporting these WGM modes close to the fiber surface. In addition, it was shown that it was possible to predict the difference in effective index of the two types of modes from the equation:

$$\delta\nu = \Delta\nu \frac{n_{eff}}{\Delta n_{eff}} \quad (6.22)$$

Where  $\delta\nu$  is the modulation frequency spacing,  $\Delta\nu$  is the WG mode spacing, and  $\Delta n_{eff}$  is the difference in effective index of the two sets of modes. This analysis assumes that the only modes supported in the structure are the lowest order radial modes in both the fiber and the waveguide. This results in an evenly spaced modulation of the spectrum since only two sets of modes are interfering.

Another way of approaching the problem is to think of two (or more) different cavities or sets of cavity modes that are supported in the same structure which are capable of interacting. One represents a set of strongly confined modes in the polymer layer while the other consists of a set of modes that penetrate into the glass fiber or into the air surrounding the layer. It cannot be said that these cavities are predominantly outside of the polymer layer since if this was the case, they would not experience any gain and thus lasing of the resonance modes would not be observed in an incomplete ring. However these modes penetrate further into the fiber or air than the strongly confined waveguide modes of the polymer layer, and can be expected to have a lower effective index since the glass/air has a lower refractive index. It is the interaction of these families of modes that causes the modulation that appears in the spectrum. An analagous effect has been studied by Corbett *et al.*<sup>24</sup> in Fabry-Perot cavities made from InP/InGaAsP. In that study, controlled perturbations have been incorporated into Fabry-Perot cavities in the form of slots. These slots constitute weakly coupled sub-cavities within the main

cavity causing a modulation in the emission spectrum. When the number of slots exceeds a certain number, the laser is capable of emitting at just one wavelength with a very strong suppression of the other modes in the cavity. Additionally, the position of the emission peak is controllable by suitable position of the slots in the cavity. Tunable single mode lasers are very desirable for telecommunications applications especially wavelength division multiplexing devices.

It can be seen from Figure 6-12, that the modulation in the spectrum from the microring device used in this study is not evenly spaced in wavelength. This would suggest that there are more than two sets of modes interfering to produce the resulting emission pattern. This considerably complicates the analysis of the ring although it is possible to say that the emission is certainly dominated by the lowest order ring WG modes, which would suggest that they have the highest  $Q$ .

### **Cavity $Q$**

In estimating the cavity  $Q$ , some of the approximations outlined in section 6.5 were made. Taking the free spectral range as the distance between emission peaks gives an estimate of  $Q = 1120$ . This value can certainly be regarded as a lower end estimate. Assuming that the linewidth does not change above threshold gives a cavity  $Q = 2500$ . From these estimates it is fair to assume that  $Q$  for the WG modes is of the order of  $10^3$ , which is in good agreement with similar structures from literature.<sup>10</sup>

### **Input-output characteristics**

To illustrate that the spectral lines observed are due to laser emission, the integrated emission spectrum was measured as a function of pump fluence. The results of this measurement are shown in Fig. 6.12.

A clear kink in the data exists at  $1.1 \text{ mJ/cm}^2$  which is indicative of a lasing threshold. The value of  $1.1 \text{ mJ/cm}^2$  is quite a high threshold considering the cavity has a high  $Q$  value. Part of the reason for this is the inefficiency of the pumping mechanism since in addition to only pumping part of the ring, the pump beam must traverse the silica of the capillary before it reaches the ring. Therefore in addition to

being absorbed by the silica, it will undergo reflection loss at the air-silica boundary and also at the silica-polymer boundary. Furthermore, a dopant concentration of only 0.1 wt % has been used which may not be optimal. Improvements in device design will be shown to bring this lasing threshold down considerably.

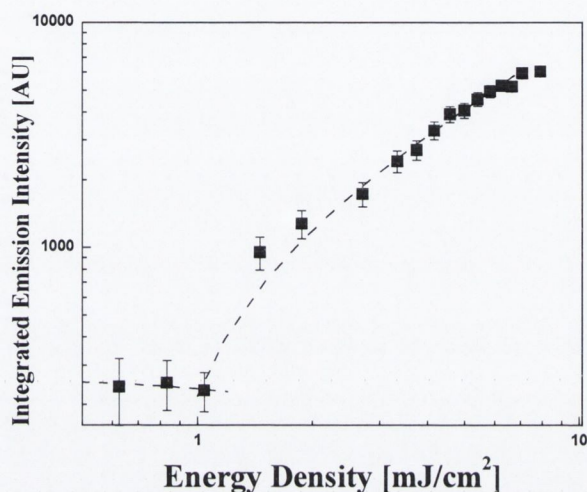


Figure 6-14 Integrated emission intensity as a function of pump fluence. Kink in the data at about  $1.1 \text{ mJ/cm}^2$  indicates the onset of lasing.

## 6.6.2 80 micron diameter microrings

### Device Description

The microrings studied in this section are made from 1 wt % B2080 in polystyrene drawn from a 50 g/l toluene solution.

Figure 6-15 shows a microscope image of such a fiber, which has been illuminated by a UV photodiode for clarity. From the image it is clear that two regions of coverage exist. In region A, the coating is thin and uniform while in region B, the coating has formed from droplets which has resulted in a thicker final ring. An initial experiment was carried out to assess the differences in behaviour of rings from region A and region B.

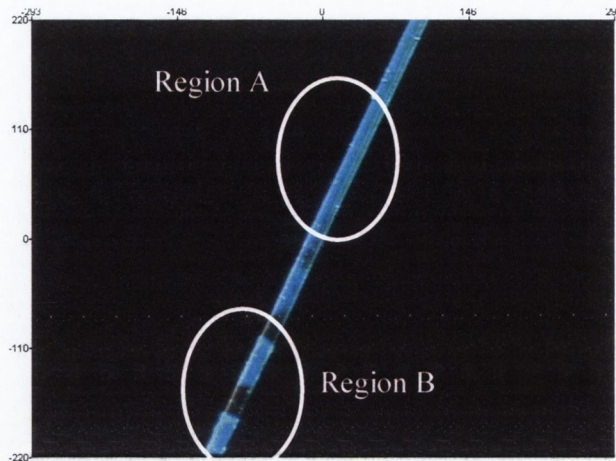


*Figure 6-15 Microscope image of coated 80 $\mu\text{m}$  silica fiber. Regions A and B denote regions of different coverage.*

Figure 6-16 shows the emission spectrum from a thinly excited stripe in region B. The emission is highly multimode with several well-defined very evenly spaced peaks. The wavelength spacing is 0.588 nm.  $Rn_{eff}$  is calculated to be 67.56  $\mu\text{m}$  and assuming the effective index can be approximated by the refractive index of the doped polymer, this results in an estimated ring diameter of 85.4  $\mu\text{m}$ . Assuming the layer thickness to be on the order of 1-2  $\mu\text{m}$ , this value is in excellent agreement with the nominal fiber diameter of 80  $\mu\text{m}$  plus a coating. Typical threshold values of devices with this kind of emission spectrum are of the order of 100  $\mu\text{J}/\text{cm}^2$  or higher. The presence of such evenly spaced spectral peaks is also indication that the emission is well described by strongly confined WG modes in the polymer layer.

The emission from region A however, looks very different as shown in Figure 6-17. In this region the emission displays a much smaller number of more widely spaced emission lines which are not evenly spaced. Since this device is formed from a very thin layer of polymer on the fiber, it may be possible that the modes are not well confined to the polymer layer but penetrate more deeply into the glass fiber, in which case, the analysis outlined in section 6.4 may not be applied. The question arises as to what physical phenomenon could give rise to the emission spectrum observed from this device and if it is related to the phenomenon observed in this study and in others, of the modulation of one set of modes in the device by the presence of another.

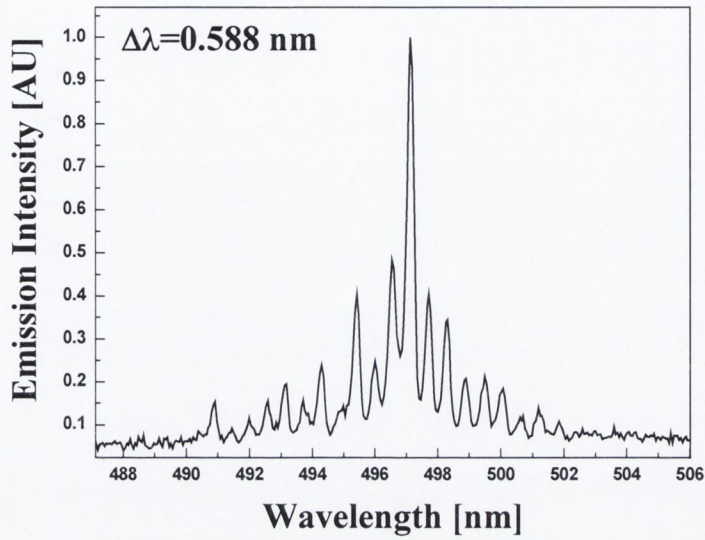


Figure 6-16 Typical emission spectrum from Region B of Figure 6-15.

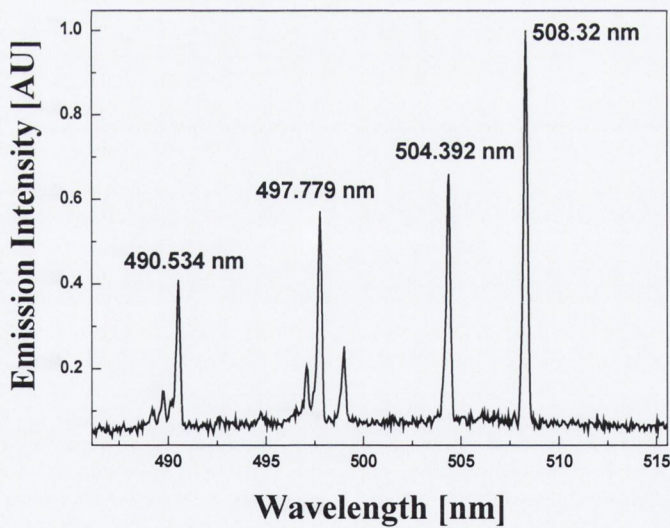
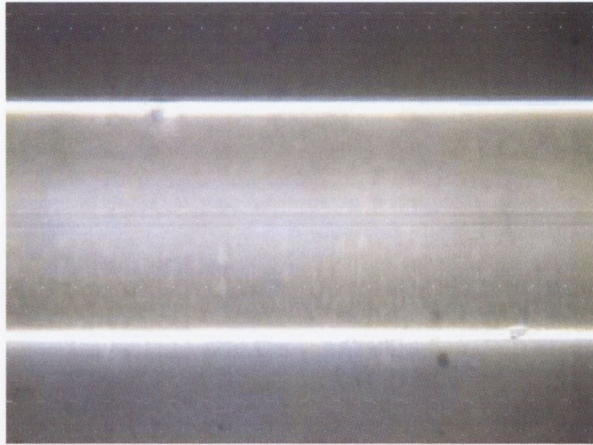


Figure 6-17 Typical emission spectrum from Region A of Figure 6-15

To further study this effect and to characterize the rings more carefully, a detailed analysis of the structure and laser emission from a device which shows emission characteristics intermediate between these two states was carried out.

### Microscope image analysis

As mentioned above, the fibers were cleaned in a KOH solution prior to dip coating. Figure 6-18 shows a 50 X image of an uncoated fiber. The image has been slightly defocused in order to capture the whole fiber since the surface is curved.



*Figure 6-18 80  $\mu\text{m}$  diameter fiber after cleaning in KOH solution prior to coating. Fiber core is visible in centre of fiber . Magnification: 50 X*

Figure 6-19 shows a 50 X magnified image of the actual surface of the fiber. There is evidence of the presence of some surface contaminants. There are many possible sources of this material since there are many stages in the cleaning process.

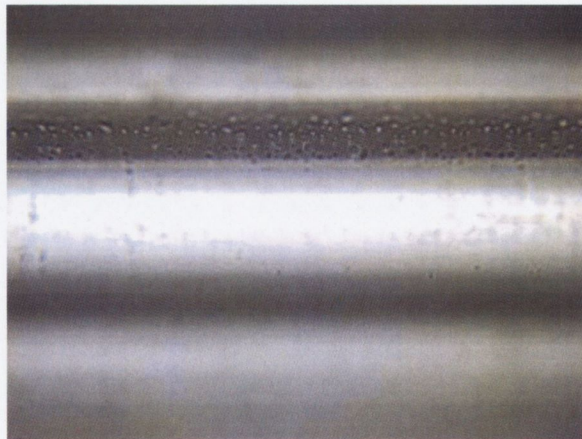
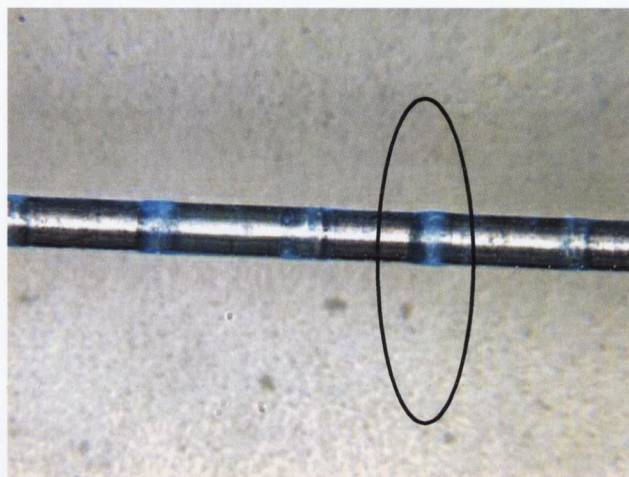


*Figure 6-19 Surface of 80  $\mu\text{m}$  diameter fiber after cleaning in KOH solution prior to coating. Magnification: 50 X*

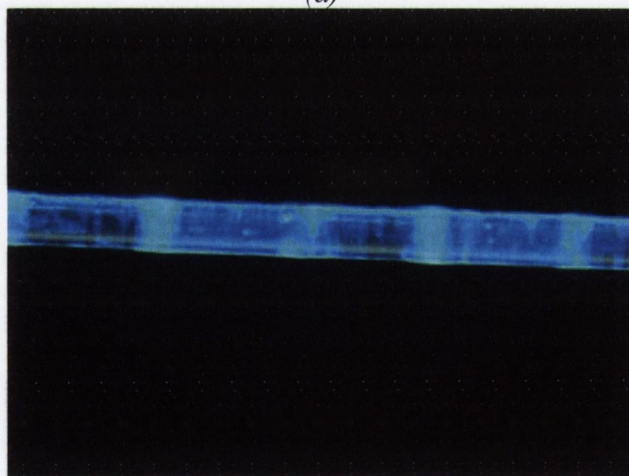
Figure 6-20 is an image of the microrings formed on the surface of the fiber and its corresponding fluorescence image at a factor of 10 X magnification. While there is



some level of coating all along the fiber, most of the material is confined to rings that have self-assembled on the fiber due to inadequate wetting of the fiber surface by the solution. Using the line length tool, the thickness of the fiber was measured to be  $82\ \mu\text{m}$  while the outer ring diameter was measured to be  $85\ \mu\text{m}$  with a resulting coating thickness of  $\sim 2\ \mu\text{m}$ .



(a)

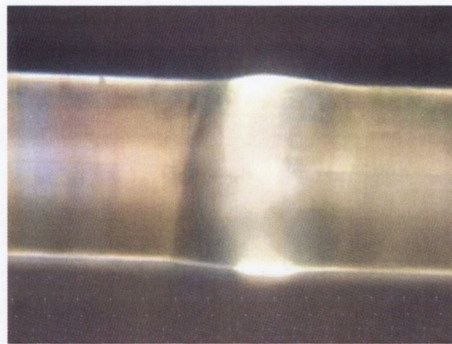


(b)

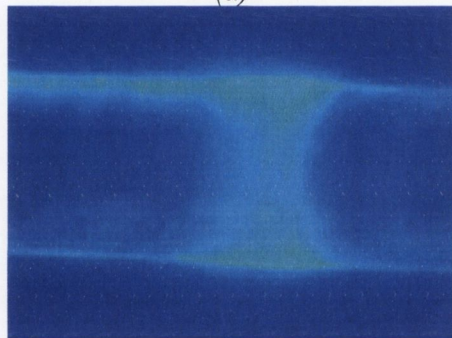
*Figure 6-20 Microrings formed on  $80\ \mu\text{m}$  diameter fiber. (a) image taken under normal lamp illumination. (b) Fluorescence image taken with long exposure under excitation with a UV light emitting diode. Ring marked with ellipse is selected as an area of interest for higher magnification measurements.*

The area marked with the ellipse in Figure 6-20 (a) was imaged at higher resolution. Figure 6-21 shows this microring at a magnification of 50X and its corresponding fluorescence image. The microring and fiber thickness was measured under this

magnification. The average fiber diameter was  $80\ \mu\text{m}$  and the ring diameter  $84.0\ \mu\text{m}$  giving a coating thickness of  $2\ \mu\text{m}$  which is in agreement with the measurement at 10 X magnification.



(a)



(b)

*Figure 6-21 Image of microring on  $80\ \mu\text{m}$  diameter fiber at magnification of 50. (a) Image taken under normal illumination. (b) image taken under excitation with UV light emitting diode at long exposure.*

Under 100 X magnification, the surface of this ring can be imaged further. This is shown in Figure 6-22. There is a high degree of inhomogeneity evident at this level of magnification and the material appears to form phases on the fiber surface. This may be due to the presence of the surface contaminants shown in Figure 6-19 which become centres of altered surface energy which then alter the morphology of the film as it forms.

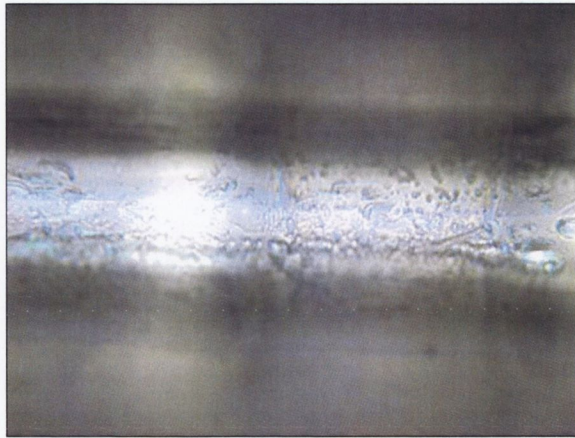


*Figure 6-22 High magnification (100 X) image of microring surface showing microstructure on coating surface.*

### **Lasing Characteristics**

Despite these inhomogeneities, the microrings shown in these images reliably and reproducibly provide low-threshold lasing. This could certainly be improved substantially with improvements in the method of production. There are many ways that this could be achieved and these will be outlined in section 6.8.1 .

It was observed in lasing experiments on these devices that lasing occurred from the thick ring region as opposed to the very thinly coated region between the rings. Typical emission spectra at different pump fluences is shown in Figure 6-23.

The spectrum can be seen to be somewhat more complex than that shown in Figure 6-16. The regularly spaced peaks that are expected from a microring with strong confinement of the modes are strongly modulated with many of the modes not appearing at all.

If the assumption is made that the peaks appearing in the spectrum are WG modes in the polymer layer, and those that are missing have been quenched by an interaction with other modes supported by the structure such as whispering gallery modes propagating close to the polymer-air interface, it is possible to make predictions about where the missing modes should appear by using the analysis in section 6.4.

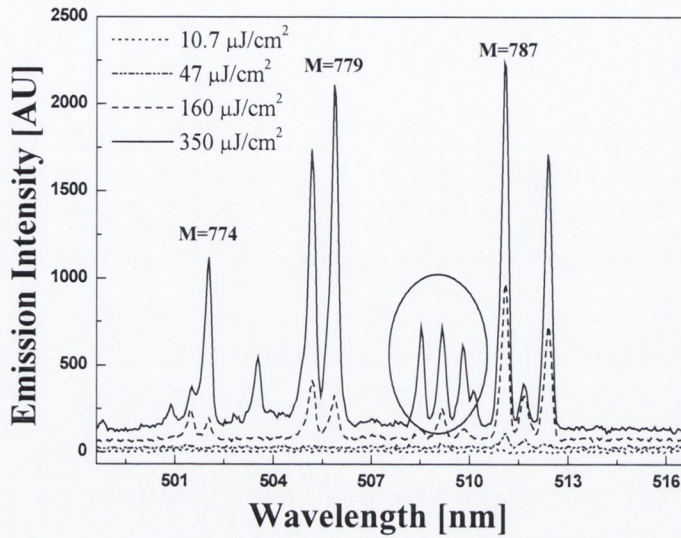


Figure 6-23 Typical emission spectrum from 80  $\mu\text{m}$  microrings shown in Figure 6-20.

Starting with the three peaks from 508.531 nm to 509.802 nm highlighted with a ring in Figure 6-23. The mode spacing between these three peaks is 0.635 nm.  $Rn_{eff}$  can be calculated to be 65.1  $\mu\text{m}$ . Assuming the effective index can be approximated by the refractive index of the polymer (although it can be expected to be somewhat lower than this due to the presence of the lower refractive index silica), this gives a value of 82  $\mu\text{m}$  for the diameter of the cavity. This is in reasonable agreement with the measurements made on the microscope images. If the effective index of the mode is say 2 % lower than that of the polymer, this gives exact agreement between the results which would indicate that the mode is reasonably confined within the polymer layer.

Using Eq. 6.15,  $\omega_{m,1} = \frac{X_m^1 c}{n_{eff} R}$ ,  $X_m$  for this spectral region can be calculated to be of the order of 800. Using a mathematical table, it is possible to find values of  $m$  that correspond to values of  $X_m$  in this region. Such a table is shown in Table 6.1. In addition, taking  $\Delta\lambda$  to be 0.635 nm it is possible to predict the position of the peaks in the spectrum. This is also shown in Table 6.1.

Figure 6-24 shows the predicted peaks (triangles) versus the spectrum plotted on a semi-logarithmic scale for clarity. It can be seen that there is good correlation between predicted peak position and the actual peaks that are present especially in the middle of the spectrum. On this scale it is also evident that the some of the “missing” peaks are present at a low level in the spectrum.

*Table 6-1 Values of  $m$ ,  $X_m$  and predicted wavelength position for the spectral region shown in Figure 6-23.*

<b><math>m</math></b>	<b><math>X_m</math></b>	<b>Predicted <math>\lambda</math></b>
774	791.151	502.381
775	792.158	503.020
776	793.166	503.660
777	794.173	504.230
778	795.18	504.939
779	796.188	505.579
780	797.195	506.219
781	798.202	506.858
782	799.209	507.498
783	800.217	508.138
784	801.224	508.777
785	802.231	509.417
786	803.238	510.056
787	804.245	510.696
788	805.253	511.336

In Figure 6-25, the measured wavelength peaks versus the predicted peaks have been plotted. Gaps have been left where it is evident that there are peaks missing from the spectrum. There is excellent correlation between the two, the slope being very close to 1. The slight discrepancy from slope of 1 is probably due to a small calibration error in the detection system. Indeed this slope is identical to that obtained using the same analysis on the capillary device. This analysis indicates that the modes appearing in the spectrum are well described by waveguide modes in the polymer layer.

Using this analysis, some of the modes in the emission spectrum in Figure 6-23 have been labelled.

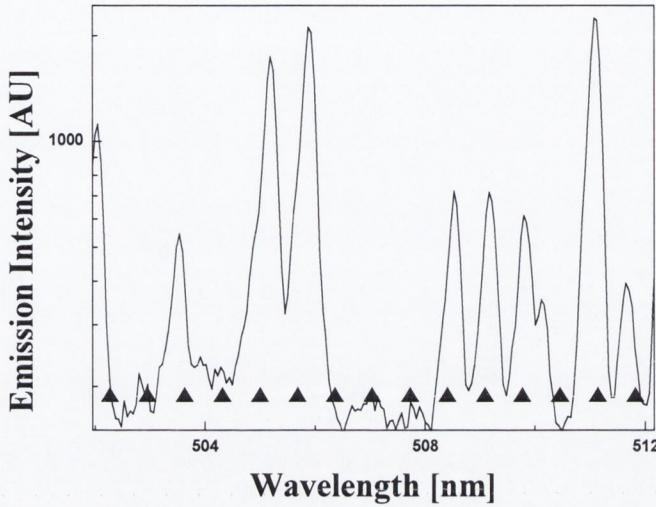


Figure 6-24 Emission spectrum plotted on a semi-logarithmic scale. Triangles represent predicted position of peaks.

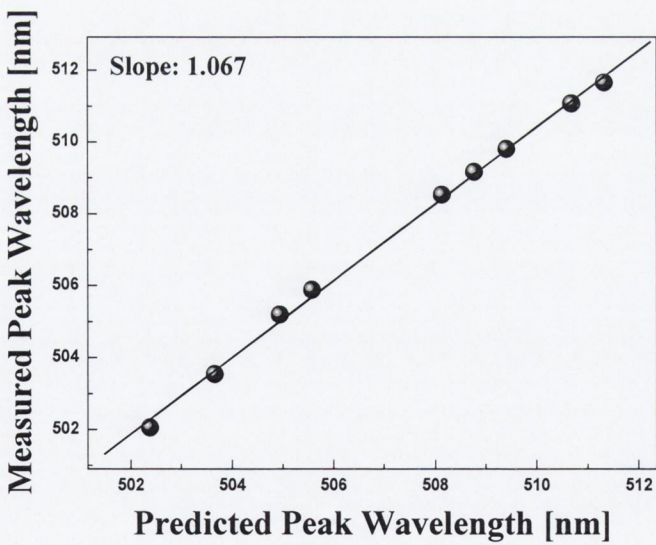
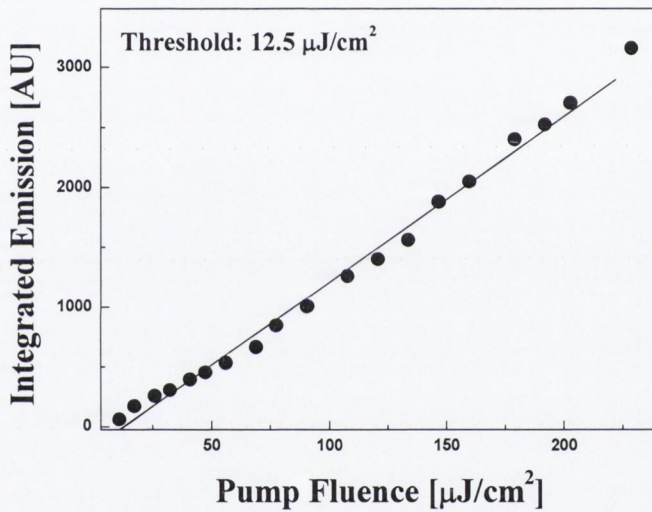


Figure 6-25 Measured wavelength peaks versus predicted peak position. Gaps have been left where it is evident that some of the peaks are missing from the spectrum.

Taking these results in combination with the emission spectra in Figs. 6-14 and 6-15, it may be argued that the strength of interaction between the different sub-

cavities within each device is governed by the thickness of the ring deposited on the glass fiber and hence the depth to which the modes in the layer penetrate into the fiber or air above. In thicker films such as those shown in region B of Fig. 6-13, the modes are strongly confined to the polymer layer. In addition, it is possible that since the layer is thick, the other modes of the structure are highly lossy and cannot couple well to the WG modes. As the layer thickness is reduced, the interaction between the different types of modes increases as does the number of different types of modes causing the number of emission peaks to reduce dramatically.



*Figure 6-26 Integrated emission intensity as a function of pump fluence. Straight line method has been used to give a lasing threshold of  $12.5 \mu\text{J}/\text{cm}^2$ .*

The input-output characteristics of this device have also been measured by monitoring the emission intensity from the ring as a function of pump fluence. The results of this measurement are shown in Figure 6-26. At low pump fluences the emission from the ring is extremely noisy. As soon as the detection system is capable of detecting clear emission from the device, there are peaks in the spectrum making the point of onset of lasing very ambiguous. For that reason, the data have been fit to a straight line from which it is possible to obtain the x-axis intercept. This value may be used to estimate the threshold for laser action. The value obtained is  $12.5 \mu\text{J}/\text{cm}^2$ . This is an order of magnitude lower than that obtained from the ring shown in Region B of Figure 6-16. This is a very low threshold value

especially considering the fact that only a fraction of the ring is being pumped so there is a considerable portion of the ring exhibits has no net gain. This situation can be improved by using longitudinal pumping as described by Dou<sup>23</sup> et al. In this case, a much lower threshold can be expected.

## 6.7 Comparison with literature

There have been very few demonstrations of microcavity lasing in the blue/green region using organic materials. The majority of studies have focussed on the 600 nm region. Table 6-2 gives a summary of results from the literature for microring devices using organic material.

*Table 6-2 Summary of results obtained in this study and other similar works from the literature.*

	$\lambda_{em}$ (nm)	Diameter ( $\mu\text{m}$ )	$F_{th}$ ( $\mu\text{J}/\text{cm}^2$ )	$E_{pulse}$ (nJ)	$P_{th}$ (W)	$\tau_{pump}$ (ns)
<b>B2080/PS*</b>	505	80	12.5	2.3	0.77	3
<b>DCM/PMMA<sup>23</sup></b>	620	63	6	4	40.8	0.1
<b>DOO PPV<sup>18</sup></b>	630	125	-	1	-	0.1
<b>PDPA-Si(iPr)<sub>3</sub><sup>18</sup></b>	530	25	No	threshold	provided	0.1
<b>BEH PPV<sup>10</sup></b>	630	100	1000			10
<b>Pyromethene/PS<sup>8</sup></b>	600	125		1.6	16	0.1

As can be seen from this table, the devices under investigation in this study operate at a considerably lower wavelength than any of the devices listed. In addition the 80  $\mu\text{m}$  device compares very well with other devices in its threshold characteristics.

\* Results obtained in this study



## 6.8 Future work

The following sections will describe directions for future work in the production of low threshold, high-Q laser devices using polymeric materials.

### 6.8.1 Microrings

Despite many reports of microring lasing using silica fibers coated with organic material, there has as yet been no reports of a systematic study of the formation of these rings or a study of the relationship between coating properties and device performance. To be of any practical significance, controlled formation of the microrings and the corresponding characterization of the output properties is essential.

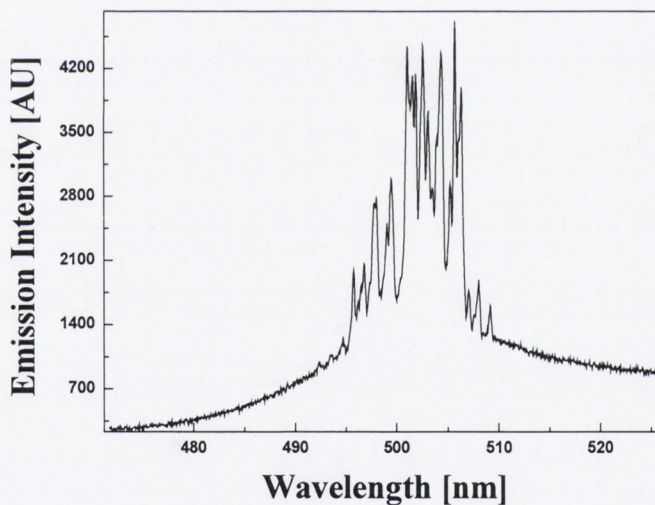


*Figure 6-27 Emission spectrum from 80  $\mu\text{m}$  microrings under longitudinal pumping.*

The image analysis in this chapter has shown that even in rings with rather poor surface quality and in the presence of surface contaminants, low threshold lasing has been achievable. This implies that improvements in the design and production of the devices could lead to very significant improvement in performance characteristics. One such improvement that has already been demonstrated by Dou *et al.*<sup>23</sup> is the use of longitudinal pumping where the rings are pumped by launching

the pump light through the fiber resulting in the rings being pumped uniformly from inside the fiber. An initial test on the 80  $\mu\text{m}$  microrings described above demonstrated that this was achievable. The emission spectrum from such a test is shown in Figure 6-27.

While lasing was easily achievable, it can be seen from the spectrum that there is a very significant spontaneous emission background. In addition the spectrum is very complex. This is easily explained when considering the experimental setup used to measure the emission spectrum. The liquid light guide placed over the fiber to capture the light has a large numerical aperture and as such captures emission from all parts of the fiber with various degrees of coating, some areas of which are lasing and some of which are not. If longitudinal pumping is to be useful, control of the position of ring formation is necessary. By changing the surface properties of the silica fiber it is possible to change and control the formation of the micro-rings.

This was achieved by using a silane treatment of the surface which makes it more hydrophobic (note, that the use of the word hydrophobic in this sense refers to the coating solution used as opposed to the normal application of this term to water). An area on the fiber was then defined by etching a ring shape on the fiber surface. Upon dip-coating of the fiber, the solution should preferentially stick to the etched ring which allows site selective formation of the rings.

The recipe used to achieve this was as follows. Firstly the silica fibers were soaked in potassium hydroxide solution for 24 hours. This removed surface grease and exposes the OH dangling bonds on the silica surface. After this treatment the fibers were washed in water, acetone and IPA and dried at 65 °C.

The silane used was chlorotrimethylsilane. The chlorine group reacts with the OH group on the surface to create a bond. The methyl groups then stick up from the surface and form a network completely coating the fiber. This treatment resulted in an increase in contact angle at the silica surface of 10 degrees (measured on flat silica substrates) which indicates that the solution adheres less well to the silanized surface than to the bare silica.

After this, thin rings were etched out of the silane surface by rotating the fibers over a sharp blade coated in potassium hydroxide. This removed the silane and exposed the OH bond on the silica again. The polymer solution adhered preferentially to these exposed regions when the fibers are dip-coated. Figure 6-28 shows a microscope image of such a ring formed on a treated surface.



*Figure 6-28 Microscope image of 80  $\mu\text{m}$  ring formed on surfacesilane- treated fiber.*

While this demonstrates that site selective positioning of the microrings is possible, there are problems associated with this method. The “contrast” in surface energy between the silanized area and the etched ring is not sufficiently large that the rings only forms on the etched area. This means that it is necessary to wash the fiber in solvent after dip-coating to remove the material from the silanized area. This also removes some of the material from the ring which means that the coating becomes extremely thin. The ring shown in Figure 6-28 was too thin to support microring lasing.

Further improvements in this method could be achieved by suitable choice of a different silane as well as a more controlled method of etching the ring. In addition, a controlled draw rate is essential for any coating formation. All of the fibers in this study have been drawn by hand which is obviously a highly uncertain method. This probably accounts for a considerable amount of the surface inhomogeneity observed in the rings. Also, the initial fiber preparation needs to be improved to eliminate the contaminants seen prior to dip-coating. However with these improvements it could be envisaged that microrings could be formed quite easily in defined areas of a fiber with well defined surface profiles and lasing characteristics. In addition, if the

coating quality could be improved, these microring lasers could be expected to lase at a considerably lower threshold.

### 6.8.2 Polymer optical fiber production.

One area that has not been dealt with thus far is that of the production of a doped polymer fiber. The manufacture of a dye-doped polymer optical fiber necessitates the solving of many physical and chemical problems.

For example, the dye must be incorporated into a host matrix that is both chemically stable, and has thermomechanical properties that make it suitable for drawing into a polymer optical fiber. Furthermore, the material must be made into a shape that can be drawn into a fiber. In addition to this, a method for incorporating cladding onto the fiber must be found.

The following sections will give a summary of a method of production for achieving these aims and while it is not yet perfect, it is a considerable step in the right direction.

In light of the spectroscopic measurements carried out in previous chapters, the material chosen as the host matrix for the fiber perform was polystyrene. The dye was added to the styrene monomer at a maximum concentration of 0.9 wt % dissolving immediately in the viscous material. The polymerisation was carried out via bulk polymerisation at 60 °C in a test tube which results in a preform of suitable shape for drawing. AIBN was used as the initiator, attacking the double bond in the monomer allowing it to react. Thiol was used as the chain transfer agent to terminate the polymerisation at a suitable molecular weight for drawing. There are some problems that can be encountered at this stage of production. As the polymerisation proceeds, the solution becomes more viscous, which can result in residual monomer being trapped unreacted in the bulk. At the drawing stage this can bubble under the elevated temperatures necessary for the initial drop, which then results in breakage and microstructure in the core. For this reason, the temperature is increased during polymerisation to allow more motion of the chains providing the opportunity for further reactions. In addition, some of the thiol can

remain unreacted in the bulk after polymerisation. Thiol has a boiling point of 96-98 °C and this can also cause catastrophic failure at the drawing stage.

### Fiber preform

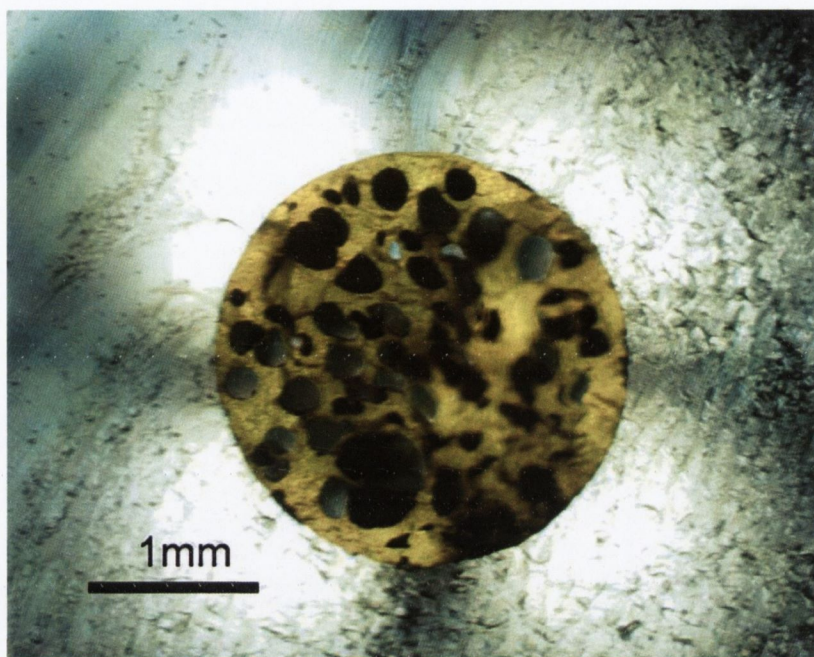


*Figure 6-6-29 Image of fiber preform after stretching stage. Black spots are bubbles in the core of the fiber.*

Gel permeation chromatography can be used to identify the presence of these species in the bulk and to optimise the temperature profile and chain-transfer agent concentration to produce a suitable material. Figure 7-1 is a photograph of a fiber after stage one of the drawing process from an unoptimized bulk. The severe bubbling has been caused by one of the two processes described above. This fiber broke during the second stage of drawing.

### Cladding and drawing procedure

A two-stage draw process was necessary since the preforms were too short to draw in one step. The first stage is a stretching step to produce a fiber preform long enough for the second continuous draw stage.

PMMA was chosen as the cladding for the fiber since it has a lower refractive index than polystyrene and also a similar glass transition temperature meaning that the

two materials have similar thermomechanical properties and can be drawn together. The cladding was incorporated by drilling a hole in a 7 cm diameter Perspex rod (without drilling right through the bottom) and inserting the polystyrene preform. The sample was clamped at both ends so that it could be stretched and gradually heated up in progressive steps with the following temperature profile: 150 °C (1 hr), 190 °C (20 mins), 210 °C (15 mins). At the same time, suction was applied to the top end of the sample to seal the interface between the polystyrene and PMMA sleeve. The actual full draw is carried out at the lower temperature of 180 °C. This resulted in a good join between the core and cladding however the bubbling described above has been prohibitive so far and improvements in the preform are currently underway.

### **Future outlook**

With regard to making polymer optical fiber lasers, a “recipe” has been devised which is a significant step towards the realisation of this device. It remains to optimise the chemical composition of the doped preform prior to cladding so as to remove the possibility of bubbling. This device could be useful for one and two-photon pumped lasing, and also as an optical amplifier for use in the blue-green spectral region. It remains to be seen if the dye will fully survive the fiber manufacturing process and if it shows the excellent photostability that was observed in dye-doped polystyrene waveguides.

## **6.9 Summary**

The aim of this chapter was to investigate a simple method for producing high quality laser cavities from the doped polymeric materials investigated in previous chapters. This has been achieved and low threshold lasing has been demonstrated in microrings where the coatings are of sufficiently good quality. This has also led to the demonstration of interesting behaviour involving lasing with an unusually low number of modes.

In addition, a method has been proposed for the controlled formation and improvement of these microrings which could lead to lowering of the lasing threshold and more controlled output characteristics.

Furthermore, a method for producing doped polymer fibers has been proposed and initial characterizations on this method have revealed several issues which should be improved to achieve a blue-green emitting polymer fiber laser.

## References

- <sup>1</sup> G. Björk, A. Karlsson, Y. Yamamoto, Phys. Rev. A **50**, 1675 (1994).
- <sup>2</sup> Y. Yamamoto, S. Machida, G. Björk, Phys. Rev. A **44**, 657 (1991).
- <sup>3</sup> G. Björk, H. Heitmann, Y. Yamamoto, Phys. Rev. A **47**, 4451 (1993).
- <sup>4</sup> R.E. Slusher, A.F.J. Levi, U. Modieen, S.L. McCall, S.J. Pearton, R.A. Logan, Appl. Phys. Lett. **63**, 1310 (1993).
- <sup>5</sup> N.C. Frateschi, A.F.J. Levi, Appl. Phys. Lett. **66**, 2932 (1995).
- <sup>6</sup> N.B. Rex, R.K. Chang, L.J. Guido, IEEE Photon. Tech. Lett. **13**, 1 (2001).
- <sup>7</sup> J.J. Campillo, J.D. Eversole, H.-B. Lin, Phys. Rev. Lett. **67**, 437 (1991).
- <sup>8</sup> M. Kuwata-Gonokami, R.H. Jordan, A. Dodabalapur, H.E. Katz, M.L. Schilling, R.E. Slusher, Opt. Lett. **20**, 2093 (1995).
- <sup>9</sup> S.E. Burns, G. Denton, N. Tessler, M.A. Stevens, F. Cacialli, R.H. Friend, Opt. Mater. **9**, 18 (1998).
- <sup>10</sup> Y. Kawabe, C. Spiegelberg, A. Schülzgen, M.F. Nabor, B. Kippelen, E.A. Mash, P.M. Allemand, M. Kuwata-Gonokami, K. Takeda, N. Peyghambarian, Appl. Phys. Lett. **72**, 141 (1998).
- <sup>11</sup> H.P. Weber, R. Ulrich, Appl. Phys. Lett. **19**, 38 (1971).
- <sup>12</sup> <http://www.firsttenangstroms.com>: Application Note.
- <sup>13</sup> A.W. Adamson in *Physical Chemistry of Surfaces*, 3<sup>rd</sup> ed. (John Wiley and Sons New York)
- <sup>14</sup> G. McHale, N.A. Kaeb, M.I. Newton, S.M. Rowan, Journal of Colloid and Interface Science **186**, 453 (1997).
- <sup>15</sup> G. McHale, M.I. Newton., Colloids and Surfaces A **206**, 79, 2002.
- <sup>16</sup> R.D. Deegan, O. Bakajin, T.F. Dupont, G. Huber, S.R. Nagel, T.A. Witten, Nature **389**, 827 (1997).
- <sup>17</sup> M.K. Chin, D.Y. Chu, S.-T. Ho, J. Appl. Phys **75**, 3302 (1994).
- <sup>18</sup> S.V. Frovlov, M. Shkunov, Z.V. Vardeny, K. Yoshino, Phys. Rev. B **56**, R4363 (1997).



- 
- <sup>19</sup> S.V. Frovlov, M. Shkunov, A. Fujii, K. Yoshino, Z.V. Vardeny, *IEEE J. Quant. Elect.* **36**, 2 (2000).
- <sup>20</sup> A. E. Siegman, *Lasers*, (Oxford University Press, Oxford, 1986).
- <sup>21</sup> M.L. Gorodetsky, A.A. Savchenkov, V.S. Ilchenko, *Opt. Lett.* **21**, 453 (1996).
- <sup>22</sup> G. Ramos-Ortiz, Ch. Spiegelberg, N. Peyghambarian, B. Kippelen, *Appl. Phys. Lett.* **77**, 2783 (2000).
- <sup>23</sup> S.X. Dou, E. Toussaere, T. Ben-Messaoud, A. Potter, D. Josse, G. Kranzelbinder, J. Zyss, *Appl. Phys. Lett.* **80**, 165 (2002).
- <sup>24</sup> B. Corbett, C. Percival., P. Lambkin, *IEEE J. Quant. Elect.*, **41**, 490 (2005).

# Chapter 7 Conclusions and Future Work

## 7.1 Introduction

In chapter 1 of this thesis, the aim of the project was outlined as being the development and characterisation of a luminescent polymer gain medium with large induced emission cross-section and corresponding large optical gain for the development of a compact optical amplifier or laser operating in the blue-green spectral region, compatible with the lowest loss communication window of acrylate polymer based waveguides and fibers. By a judicious choice of host polymer, very large optical gain (one of the largest gain coefficients reported to date in the nanosecond regime) has been established in a planar waveguide structure. The lasing characteristics of microresonators have also been investigated. Two-photon absorption cross-section spectra of the molecules have been measured with a view to the development of a blue polymer laser that can be pumped with 800 nm sources. Two different and independent methods, one based on nonlinear transmission, the other based on two-photon-induced fluorescence, have been employed to identify a large two-photon absorption cross-section and its host-dependence.

## 7.2 Summary

In chapter 3 the materials used in this study are introduced and basic spectroscopic measurements carried out, for example UV-VIS absorption and photoluminescence emission spectra.

In Chapter 4 the properties of B2080 as an amplifying medium in solid polymer hosts were investigated. It was shown that the photodegradation behaviour of the stilbene dyes investigated in solid polymer matrices depends strongly on the host into which they are doped with the most stable performance being provided by polystyrene. This may be due to torsional motion of the molecular backbone and subsequent trans-cis isomerization sensitising the molecule to chemical attack. The inhibition of this torsional motion in the polystyrene seems to result in an effective blocking of the path of photodegradation. The doped polystyrene was spin-cast onto pyrex substrates to form asymmetric slab waveguides and the gain measured using the variable stripe length method pumping at 355 nm in the ns regime. The dye-doped polystyrene waveguides showed excellent performance and the measured gain was one of the highest reported modal gains reported to date in organic materials in this wavelength region. The gain was measured at a range of fluences and by plotting the modal gain versus the excited state population density at each fluence, the stimulated emission cross-section was extracted. Furthermore, the loss spectrum in the waveguides was measured and lasing was shown in a rudimentary slab waveguide laser cavity.

The subject of Chapter 5 was the two-photon absorption properties of SP35 and SP48 in solid polymer hosts and in solution. Two methods were employed namely fs z-scan for the solution measurements and the two-photon induced photoluminescence method for the solid-state measurements. A larger TPA cross-section was measured in SP35 in agreement with theory and good agreement between the measurement in solution and the polystyrene host was observed. However, a poorer performance was observed in both the PMMA and PVP hosts again illustrating the importance of suitable choice of host to obtain the best performance from the dye.

In Chapter 6, microring cavities were investigated with a view to using the favourable spectroscopic properties of stilbene-doped polystyrene in a high quality cavity. Microring cavities were formed on the inner surface of glass capillaries and also on the outer surface of silica fibers. Optical microscopy and contact angle analysis were used to gain insight into the formation of the rings in order to control their formation. A large degree of inhomogeneity was observed on the surface of the microrings, however in spite of this, low threshold lasing was observed in 80  $\mu\text{m}$  diameter devices which compares very well to similar works in the literature. With improvements in the design and production of the rings it was estimated that the performance could be significantly improved and a method of forming the rings in a more controlled manner was proposed.

Investigating the possibility of two-photon pumped lasing in a solid state device was another aim of the project. At this point having measured both the optical gain and the TPA cross-section it is possible to make some predictions as to the threshold intensity for two-photon pumped optical gain and lasing.

Assuming a two-photon absorption cross-section of  $\sim 1 \times 10^{-47} \text{ cm}^4 \text{ s}$  which is the cross-section of SP35 measured at 760 nm, it is possible to estimate the threshold pump intensity for the onset of gain. For example, for the asymmetric slab waveguide, the transparency population is about 1 % in the ns regime. The corresponding threshold for the onset of gain in a device with similar modal gain and loss characteristics would be of the order of  $1 \text{ GW/cm}^2$ . This kind of intensity should be easily achievable in the core of a polymer optical fiber. One problem that may be envisaged, however, is finding a suitable way with which to launch the light into the fiber without burning the cleave. Since the microrings in presented in Chapter 6 also show low threshold lasing, they should also be amenable to two-photon pumping. Unfortunately, at the time of writing no suitable laser was available with which to pump them. While they were observed to fluoresce very strongly when pumped with the output from a titanium sapphire oscillator, the energy per pulse (max  $\sim 10 \text{ nJ}$ ) was too low to observe lasing.

### 7.3 Conclusions

In Chapter 1, a review was given of the advantages that organic materials possess from a processing point of view due to their molecular nature. In order to fully take advantage of this flexibility, it is necessary to understand and control the processes used to make devices. In the case of microring cavities, this has not been well covered in the literature and considerable scope exists for improving their performance. It was suggested in 2002 by Vardeny<sup>1</sup> that microrings of sufficiently good performance could provide the key to electrical pumped amplification using an organic material. If there is to be any progress made in this regard, a great deal of improvement in the performance of the devices is necessary as well as the development of a highly controlled method of production. Surface chemistry with surface characterization and the use of optical microscopy and contact angle analysis is one approach to this.

From a spectroscopic point of view, it has been shown that stilbene dyes have excellent properties for gain and two-photon absorption. Their weakness lies in the flexible double bonds in the backbone which allow torsional motion, however suitable choice of host in the solid state inhibits this motion making them extremely stable.

## References

---

<sup>1</sup> Z.V. Vardeny, *Nature* **416**, 489 (2002).

# Appendix I - Calculation of Pump Fluences

In both Chapter 4 and Chapter 6, a pump beam was used that had been expanded into a stripe geometry the intensity profile of which is shown schematically in Figure AI-1. The fluence quoted due to such a beam was calculated in the following way.

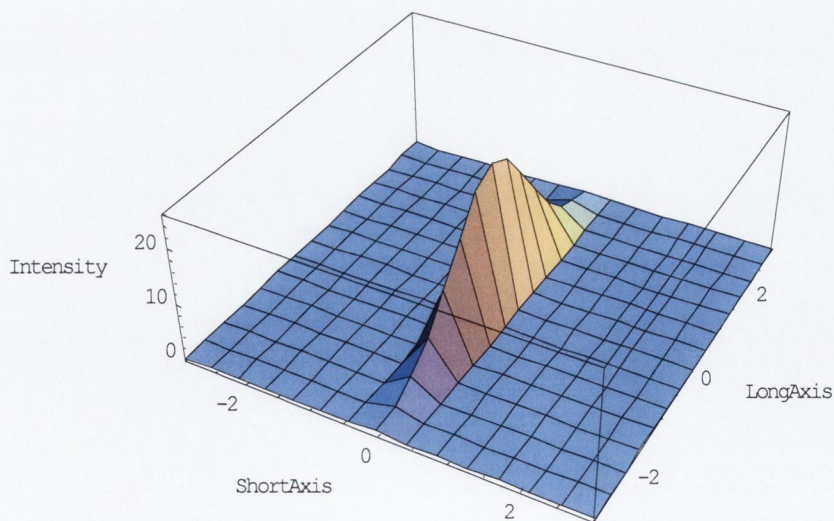


*Figure AI-1 Intensity profile of stripe beam used for pumping laser devices.*

The first cylindrical lens expands the beam into an ellipse and the second lens is then used to focus the beam into a horizontal or vertical stripe depending on the application. The beam profile at the position of the sample is calculated taking into account the  $1/e^2$  full width of the initial beam and the focal length of the two lenses using geometrical arguments. Care is taken that the sample is not placed directly at the focus of the second lens so that a geometrical optics approach is valid.

The lateral position of the sample is adjusted so that the centre of the stripe is incident on it. Having calculated the  $1/e^2$  widths of the short and long axis of the beam, a normalized 2-dimensional gaussian beam profile is assumed in order to calculate the percentage of the full beam energy that is actually incident on the sample. Once the incident energy is known, the fluence is calculated by dividing by the cross-sectional area of the area of intersection between the beam and the sample.



## Appendix II - Estimation of Excited State Population Density

In the case of nanosecond pumping of an organic material where the pulse width is many times longer than the photoluminescence lifetime, steady-state pumping can be assumed making the calculation of excited state population density from pump fluence a trivial calculation.

However, in the case of the measurements carried out for this thesis, the pulse width of the pump beam was just over twice that of the photoluminescence lifetime. To calculate the excited state population density under these conditions, the rate equation for the excited state population must be solved which is:

$$\frac{dN_2}{dt} = -\frac{N_2}{\tau_f} + \frac{\sigma_p I}{\hbar\omega} N \quad (AII-1)$$

Where  $N_2$  is the excited state population,  $\tau_f$  is the fluorescence lifetime,  $\sigma_p$  is the absorption cross-section at the pump wavelength,  $I$  is the beam intensity and  $N$  is the total population, assumed constant. In addition, the simplification will be made that the pump pulse has a square temporal shape:

$$I(t) = I_0 U(t - \tau_p) \quad (AII-2)$$

where  $U$  denotes the normalized temporal profile,  $\tau_p$  is the pulse temporal width and  $I_0$  is the peak intensity. The decay due to spontaneous emission has the form:

$$N_2(t) = N_{20} e^{-t/\tau_f} \quad (\text{AII-3})$$

Where  $N_{20}$  is the initial excited state population at the pump leading edge. Substituting this into Eq. AII-1:

$$\frac{dN_{20}}{dt} = \frac{\sigma_p I(t) N}{\hbar \omega} e^{t/\tau_f} \quad (\text{AII-4})$$

$$N_{20} = \frac{\sigma_p N}{\hbar \omega} \int_0^{\tau_p} I(t) e^{t/\tau_f} dt \quad (\text{AII-5})$$

Carrying out the integration over these limits gives:

$$N_{20} = \frac{\sigma_p N I_0 \tau_f}{\hbar \omega} \left( e^{\tau_p/\tau_f} - 1 \right) \quad (\text{AII-6})$$

Applying Eq. AII-3 to Eq. AII-6 gives the excited state population as:

$$N_2(t) = \frac{\sigma_p N I_0 \tau_f}{\hbar \omega} \left( 1 - e^{-t/\tau_f} \right) \quad (\text{AII-7})$$

For a pulse width of 3 ns and a fluorescent lifetime of 1.3 ns, the excited state population is about 90 % that of steady state population at the same intensity.

## Appendix III- Publication List

- G. Jordan, T. Kobayashi, W.J. Blau, H. Tillman, H.-H. Hörhold  
Frequency upconversion of 800-nm ultrashort pulses by two-photon absorption in a stilbenoid compound-doped polymer optical fiber  
*Adv. Funct. Mater* **13**, 751 (2003)
- T. Kobayashi, J.-B. Savatier, G. Jordan, W.J. Blau, Y. Suzuki, T. Kaino  
Near-infrared laser emission from luminescent plastic waveguides  
*Appl. Phys. Lett.* **85**, 185 (2004)
- G. Jordan, T. Kobayashi, W.J. Blau, H. Tillman, S. Pfeiffer, H.-H. Hörhold, M. Samoc, B. Luther-Davies  
Two-photon absorption and up-converted emission in blue-emitting stilbene dye  
*Nonlinear Optics, Quantum Optics* **34** (In print)
- T. Kobayashi, G. Jordan, W.J. Blau, Y. Suzuki, T. Kaino  
Gain spectroscopy and lasing in doped polymer waveguides and microstructures  
*Nonlinear Optics, Quantum Optics* **34** (In print)
- M. Djiango, T. Kobayashi, G. Jordan, W.J. Blau, Y. Suzuki, T. Kaino  
Near infra-red optical gain and lasing in luminescent polymeric microrings  
*Nonlinear Optics, Quantum Optics* **34** (In print)
- T. Kobayashi, M. Djiango, G. Jordan, M. Rütter, W.J. Blau, Y. Suzuki, T. Kaino  
Near infra-red laser emission from high-Q polymer cavities  
*Proceedings of the Society of Photo-Instrumentation Engineers* **5956** (2005) (In print)
- M. Djiango, G. Jordan, M. Rütter, T. Kobayashi, W.J. Blau, Y. Suzuki, T. Kaino  
Near infra-red lasing in dye-doped polymeric microrings  
*Proceedings of the Society of Photo-Instrumentation Engineers* **5958** (2005) (In print)

G. Jordan , M. Flämmich, M. Rüther, T. Kobayashi, W.J. Blau, Y. Suzuki, T. Kaino  
Optical characterization of a luminescent small molecule in solid-state polymer  
matrices: large gain and low-threshold microcavity lasing in the blue-green region  
Proceedings of SPIE Optics and Photonics **5934** (2005) (In print)

G. Jordan, M. Flämmich, M. Rüther, T. Kobayashi, W.J. Blau, Y. Suzuki, T. Kaino  
501-nm light amplification and large nanosecond optical gain in organic dye-doped  
polymeric waveguides  
(Submitted for publication Appl. Phys. Lett.)

T. Kobayashi, M Djiango, G. Jordan, M. Rüther, W. Blau  
0.8- $\mu\text{m}$  laser emission from photopumped luminescent polymer microresonators  
(Accepted for publication Appl. Phys. Lett.)